Università degli Studi di Firenze
Dipartimento di Ingegneria dell'Informazione (DINFO)
Corso di Dottorato in Ingegneria dell’Informazione

Curriculum: Electronics, Electromagnetics and Electrical Systems

---

# Development and Real-time Implementation of Novel 2-D and 3-D Imaging Techniques on a Research Scanner

Academic Discipline (SSD) ING-INF/01

*Candidate*
Claudio Giangrossi

*Supervisor*
Prof. Piero Tortoli
Ing. Enrico Boni

*PhD Coordinator*
Prof. Fabio Schoen

---

ciclo XXXIV, 2018/2021

Università degli Studi di Firenze,
Dipartimento di Ingegneria dell’Informazione (DINFO).

Thesis submitted in partial fulfillment of the requirements for the degree of Doctor of Philosophy in Information Engineering.

October 2021

# Acknowledgments

I would like to sincerely thank my supervisors, Prof. Piero Tortoli and Dr. Enrico Boni for their unvaluable time, and knowledgeable advices. I would also like to extend my gratitude to Dr. Alessandro Ramalli, my "unofficial" supervisor, who always supported me in my research activities, and to all my lab mates, for their great help, and for all the good times we shared together.

Last but not least, a special thanks goes to my family and my beloved ones for always supporting me during these years.

# Contents

# Chapter 1. Introduction

## 1.1 Objective

In the last decades, ultrasound imaging systems have become more and more popular thanks to their capability to investigate tissues in safe, cost-effective, and non-invasive way. Their role in diagnostic imaging has become fundamental in several medical specialties, thanks also to the introduction of advanced echographic systems fostered by the efforts of several research laboratories around the world. Such efforts are more frequently based on the use of special research scanners, characterized by flexible hardware and programmable software and firmware. These features have been demonstrated ideal for the implementation and test of new methods, such as high frame-rate (HFR) imaging, color flow imaging (CFI), vector Doppler imaging, and 3-D imaging. Especially HFR and 3-D imaging have recently attracted great interest, but they are technically demanding since they involve either the formation of thousands of images per second, or the use of 2-D probes having a large number of elements. Therefore, great challenges must be faced for effective real-time implementation of 3-D and HFR imaging methods.

My PhD activity aimed to implement and test advanced 2-D and 3-D ultrasound imaging modalities on an open research scanner called ULA-OP 256.

In the first part of my work, a new ultrasound imaging modality called Virtual real-time (VRT) was introduced through the modification of the firmware and software of the research scanner ULA-OP 256. With this modality, during a real-time (RT) investigation, the scanner initially acquires and stores in its memory up to 20 s of raw echo data. On user demand, the scanner can be switched to VRT mode: the stored data are re-processed by the same resources used in RT but at different (typically lower) rates and, possibly, with different processing algorithms and parameters. In this way, contingent difficulties of image interpretation (especially in presence of rapidly moving phenomena), or possible computational limitations imposed by hardware during continuous RT processing can be overcome. The VRT modality has been demonstrated useful in different applications, for example, to implement a high-PRF version of the Multiline vector Doppler (MLVD) method, and a

High--rame-rate CFI method, characterized by enhanced temporal and spatial resolution.

The second part of my work included the software upgrade of ULA-OP 256; it enabled the use of 2-D probes and the implementation of 3-D scanning methods. The ULA-OP 256 can now be coupled to 2-D probes with arbitrary geometries, including matrix and sparse arrays. Furthermore, the scanner is now capable of simultaneously imaging multiple planes with programmable rotational angles. Novel approaches based on a sparse spiral array probe have been implemented and tested for different applications. For example, bi-plane imaging was evaluated for robust flow mediated dilation exams. Real-time 3-D spectral Doppler analysis was also performed. Here, two planes with programmable rotational angles were scanned to produce corresponding B-Mode images, over which multiple Doppler lines could be arbitrarily set to obtain the relative Multigate spectral Doppler (MSD) profiles.

Finally, the last part of my work was specifically dedicated to the technical problems involved by HFR 3-D imaging. The management of (several) hundreds of transducer elements of a 2-D probe yields a huge amount of echo data: this makes complex and computationally expensive the processing of data volumes including thousands of lines, especially if performed at HFR. As a case report, the requirements of the main processing stages involved in ULA-OP 256 receiver have been thoroughly investigated to detect and, possibly, solve the main bottlenecks. The study has evidenced that the star architecture that digitally interconnects the eight front-end boards of ULA-OP 256 may frequently encounter data transfer bandwidth saturation that limits the overall performance in terms of frame/volume rate. A new architecture for data transfer has been proposed and shown effective to reduce the bandwidth requirements and thus, increase the performance of the scanner.

The Thesis is organized as follows:

- **Chapter 2** illustrates the basics of ultrasonic wave propagation, with focus on the architecture of ultrasound systems and on the main imaging methods.
- **Chapter 3** briefly describes the scanner ULA-OP 256.

- **Chapter 4** introduces a new ultrasound modality called Virtual real-time and shows two applications that exploit this modality.
- **Chapter 5** presents the steps necessary for the implementation of multi-plane 3-D imaging in ULA-OP 256 and shows two applications that exploit such a feature.
- **Chapter 6** presents a study on the acquisition requirements for HFR 3-D imaging. As a case study, ULA-OP 256, has been used to identify bottlenecks, limitations, and possible solutions. A new architecture for data transfer is proposed and experimentally tested.
- **Chapter 7** concludes the thesis and gives future perspectives.

## 1.2 Contributions

### *Conference Proceedings*

- **Claudio Giangrossi**, Alessandro Ramalli, Carlo Palombo, and Piero Tortoli, " Bi-plane imaging for a robust assessment of Flow Mediated Dilation," 2021 IEEE International Ultrasonics Symposium (IUS), 2021, pp. 1-4, doi: 10.1109/IUS52206.2021.9593360.
- Francesco Guidi, **Claudio Giangrossi**, Alessandro Dallai, Alessandro Ramalli, Piero Tortoli, " High-frame-rate color flow imaging with enhanced spatial resolution in virtual real-time," 2021 IEEE International Ultrasonics Symposium (IUS), 2021, pp. 1-4, doi: 10.1109/IUS52206.2021.9593479.
- **Claudio Giangrossi**, Valentino Meacci, Enrico Boni, Alessandro Dallai, Francesco Guidi, Stefano Ricci, Alfred C. H. Yu, Piero Tortoli, "Virtual real-time: a new US operating modality," 2019 IEEE International Ultrasonics Symposium (IUS), 2019, pp. 1493-1496, doi: 10.1109/ULTSYM.2019.8926259
- Valentino Meacci, Stefano Ricci, **Claudio Giangrossi**, Riccardo Matera, Alessandro Dallai, Enrico Boni, Piero Tortoli, "High velocity investigation with Multi Line Vector Doppler," 2019 IEEE International Ultrasonics Symposium (IUS), 2019, pp. 360-363, doi: 10.1109/ULTSYM.2019.8925613

### *Journal papers*

- **Claudio Giangrossi** et al., Virtual Real-Time for High PRF Multiline Vector Doppler on ULA-OP 256," in IEEE Transactions on Ultrasonics, Ferroelectrics, and Frequency Control, vol. 68, no. 3, pp. 624-631, March 2021, doi: 10.1109/TUFFC.2020.3017940
- Alessandro Ramalli, Enrico Boni, **Claudio Giangrossi**, Paolo Mattesini, Alessandro Dallai, Herve Liebgott, Piero Tortoli, "Real-Time 3-D Spectral Doppler Analysis with a Sparse Spiral Array," in IEEE Transactions on Ultrasonics, Ferroelectrics, and

Frequency Control, vol. 68, no. 5, pp. 1742-1751, May 2021, doi: 10.1109/TUFFC.2021.3051628

# Chapter 2. Ultrasound Basics

*This chapter briefly describes the fundamentals of ultrasound physics and transducers. Moreover, it gives an overview of the main architecture of an ultrasound system and the main techniques for morphological and Doppler imaging.*

## 2.1 Ultrasound propagation

The term “ultrasound” describes acoustic waves characterized by a frequency out of the auditory band (Fig. 2-1), which propagate in a medium. The energy of ultrasound is mechanical and is generated by a source that produces a pressure change in the medium. This energy is transferred from one point to another through the molecules of the medium that locally vibrate and, interfering with each other, propagate the pressure field (Fig. 2-2).

The behavior of this physical phenomenon is analytically described by the one-dimensional, wave equation:

$$\frac{\partial^2 U}{\partial z^2} = \frac{1}{c^2} \cdot \frac{\partial^2 U}{\partial t^2} \qquad 2.1$$

where $U$ [N/m$^2$] represents the stress, $z$ represents the direction of propagation of the wave, and $c$ [m/s] represents the propagation speed of sound through a medium.

The propagation speed of a medium $c$ is strictly dependent on its volumetric density $\rho$ [kg/m$^3$] and the elastic constant $\beta$ [kg/(m s$^2$)] as follow:

$$c = \sqrt{\frac{\beta}{\rho}} \qquad 2.2$$

It means that this parameter is highly variable for different media, even considering only the range of human tissues.

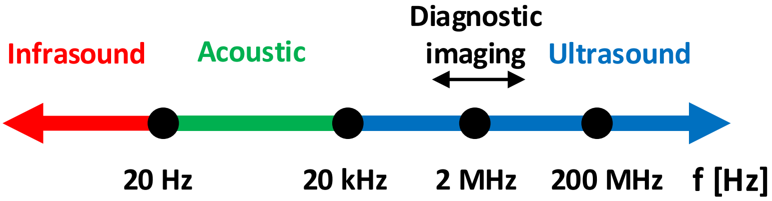

*Fig. 2-1 Ultrasound frequency range*

The generic solution of the wave equation 2.1 is:

$$U(z,t) = U_0 \,.\, e^{j(2\pi f t \pm kz)} \qquad 2.3$$

with $U_0$ [N/m$^2$] as the peak of the pressure module, $f$ [Hz] the oscillation frequency of the wave, and $k$ [1/m] the wave number. $k$ is related to the wavelength of the wave $\lambda$ [m], the frequency, and the propagation speed as follow:

$$k = \frac{2\pi}{\lambda} = \frac{2\pi f}{c} \qquad 2.4$$

Another parameter that is important to describe the propagation of sound waves is the acoustic impedance:

$$Z = \rho \cdot c \qquad 2.5$$

The acoustic impedance $Z$ [Rayl = kg/(m$^2$·s)] is a physical property of the medium that describes, in analogy to the Ohm's law, the resistance that the medium opposes to an ultrasound wave that passes through it. When a medium has a homogeneous acoustic impedance, the wave can propagate

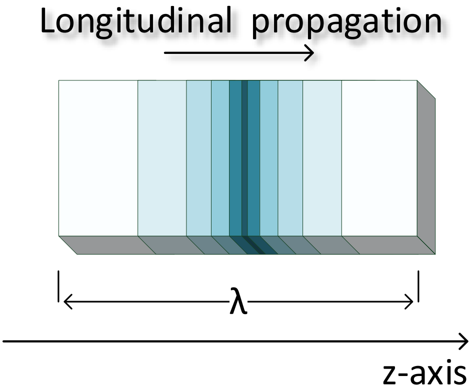

*Fig. 2-2 Propagation of a longitudinal wave of wavelength λ in a homogeneous medium.*

with a constant velocity. Otherwise, when a medium is heterogeneous - i.e., when the medium has some acoustic impedance discontinuity, caused by an interface or an obstacle - different wave phenomena may happen, such as scattering, reflection, transmission, and attenuation.

The scattering phenomenon, also known as Rayleigh scattering, occurs when the ultrasound wave meets an acoustic obstacle of size smaller or comparable to its wavelength. Here, part of the wave incident energy is transmitted to the particle and part is isotropically spread in all directions. The phenomenon can be described by the scattering cross section ($\sigma$) defined as the ratio of the spread power ($S$) and the intensity of the incident wave ($I$):

$$\sigma = \frac{S}{I} \tag{2.6}$$

The scattering cross section parameter is particularly important because relates to the power of the echoes that can be received by ultrasound system.

Reflection phenomenon occurs instead when two media, with different acoustic properties, interface to each other and a wave that propagates in the first medium encounters the second medium. Here, the wave encounters a discontinuity at the interface, and part of the energy is reflected, while the remaining part is transmitted to the second medium Fig. 2-3.

The behavior of a wave at an interface is explained by the Snell's law, which determines the relationships between the incidence ($\vartheta_i$) and transmission ($\vartheta_t$) angles, which strictly depend on the propagation speeds of the two media ($c_1$ and $c_2$, respectively) as follows:

$$\frac{c_1}{sin\,(\vartheta_i)} = \frac{c_2}{sin\,(\vartheta_t)} \tag{2.7}$$

For the Snell's law rearrangement (considering $c_2 = c_1$) and for observed experiments, the angle of the reflected wave ($\vartheta_r$), is equal to $\vartheta_i$:

$$\vartheta_i = \vartheta_r \tag{2.8}$$

The reflection $R$ and transmission $T$ coefficients indicate how the incident pressure is split in transmitted and reflected pressure. Considering the impedances of the two media ($Z_1$ and $Z_2$, respectively), and the incidence and transmission angles, they are defined as follows:

$$R = \left(\frac{Z_2 \cos\vartheta_i - Z_1 \cos\vartheta_t}{Z_2 \cos\vartheta_i + Z_1 \cos\vartheta_t}\right)^2 \tag{2.9}$$

$$T = 1 - R = \frac{4\, Z_1\, Z_2 \cos\vartheta_i \cos\vartheta_t}{(Z_2 \cos\vartheta_i + Z_1 \cos\vartheta_t)^2} \tag{2.10}$$

So far, an ideal medium has been considered, however a non-ideal, heterogenous medium produces multiple scattering effects, implies dissipation of energy, and generates heat that attenuate the propagating

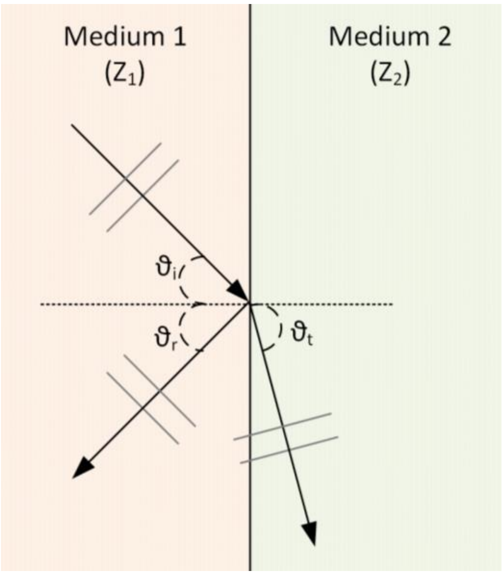

*Fig. 2-3 Incident, reflected and transmitted wave at the interface between two different media, following the Snell's law.*

wave. In particular, the acoustic intensity $I$, during propagation, decreases as an exponential function:

$$I = I_0 e^{-2\alpha z} \tag{2.11}$$

Where $\alpha$ [W/m$^2$] is the attenuation coefficient, a constant that changes with the medium characteristics, while $I_0$ is a reference intensity. Generally, $\alpha$ is expressed in [dB/cm/MHz] for practical uses.

## 2.2 Piezoelectric transducers

The piezoelectric effect, typical of materials arranged in a crystal structure is exploited in most commercial ultrasound transducers.

The direct effect consists in the mechanical deformation due to the application of an electrical excitation signal to the faces of the piezoelectric material (Fig. 2-4). If the frequency of the excitation signal is properly matched to the thickness of the material, the deformation can be sufficient to produce an acoustic wave that propagates through the surrounding medium.

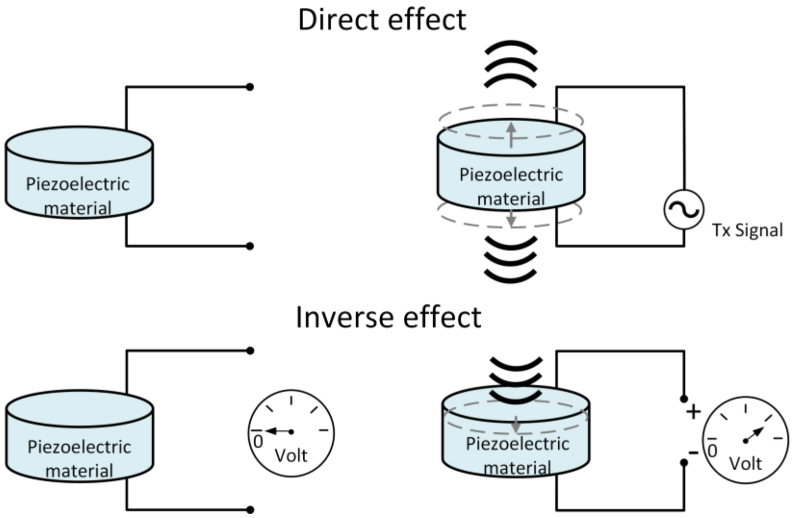

*Fig. 2-4 Basic illustration of the direct effect and inverse effect on a piezoelectric material relatively excited by a signal, and receiving a pressure on its surface*

The inverse effect is obtained when a mechanical deformation is imposed to the piezoelectric material. If the wavelength of the mechanical wave is properly matched to the material thickness, a difference of potential between the two faces is obtained. This effect is the basic principle of an ultrasound reception.

The transducers are the components that are used to generate acoustic waves through an appropriate excitation, and to receive the echoes produced from scattering or reflecting sources. The most commons transducers are based on piezoelectric materials, such as lead zirconate titanate (PZT), cut into various geometries and sizes, adapted to the application of interest, and suitable to be assembled in arrays. The piezoelectric material is generally bonded with two layers addressed to increase the transducer efficiency. When a driving signal is applied, the acoustic wave tends to propagate on both sides of the piezoelectric material, i.e., toward the medium/tissue of interest and toward the inside of the probe. The acoustic impedance of the transducer is often much higher than that of tissues that are usually investigated, and so the transmission would be very inefficient. The piezoelectric material is thus bonded with an impedance matching layer. Furthermore, to avoid that the wave propagates into the opposite direction producing undesired reflections, a second – backing - layer, operating as an acoustic absorber, is typically applied onto the second transducer side (Fig. 2-5).

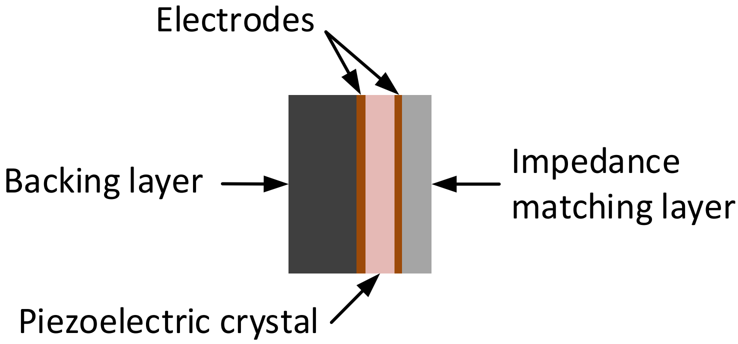

*Fig. 2-5 Typical composition of a transducer, composed by an absorber backing layer, a piezoelectric crystal with electrodes, and an impedance matching layer*

Transducers are characterized by many parameters that may strongly vary to the application necessities. Each piezoelectric crystal has a resonance frequency $f_{res}$ which is dependent on the physical properties of the crystal and on its geometry, in particular, to $c_{piezo}$ which is the sound propagation speed of the piezoelectric material, and $A$ the stiffness of the crystal:

$$f_{res} = \frac{c_{piezo}}{2A} \tag{2.12}$$

The Q-factor, which is a parameter that characterizes the quality of a transducer, is defined as:

$$Q = \frac{f_{res}}{B_W} \tag{2.13}$$

where $B_W$ is the transducer bandwidth. Transducers with a high Q factor, have a strong resonance with a narrow bandwidth, while transducers with low Q factor have a weak resonance at $f_{res}$, that dump easily. Usually, the chosen Q factor represents a trade-off, that combines an efficient resonance at $f_{res}$ to obtain a high signal to noise ratio at cost of a pulse distortion.

Medical probes [1], [2] are typically composed by an array, of hundreds of transducers, also called elements, that can be produced with different technologies (e.g. the mentioned PZT, but also CMUT, etc.). The main advantage of arrays is their flexibility, which allow the electronic focusing of the acoustic beam at different position and with different steering directions, enabled by the independent control of each element. Usually, this is done, driving the elements with appropriate transmission delays and amplitudes (also called apodization). Furthermore, in reception, dynamic beamforming is possible, which coherently combines the echoes received by the elements, with appropriate delays and apodization weightings, at each depth, thus, enabling a good focus along the entire line of interest. The most common types of medical probes are those based on convex, phased, and linear arrays [3]. In linear probes, the elements are positioned

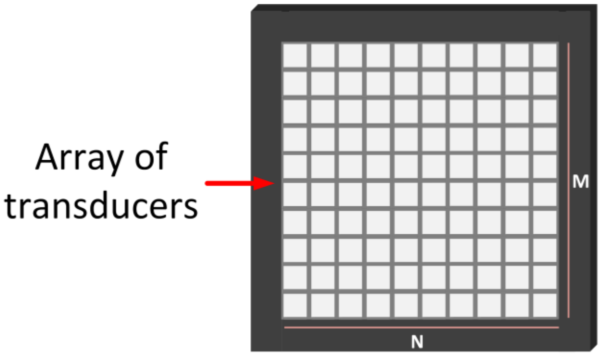

*Fig. 2-6 illustration of a 10x10 elements matrix array 2-D probe*

in line, linearly spaced at a distance called pitch, bounded with a backing layer, and, usually, with an acoustic lens for the elevation focusing.

The recent interest for systems capable of performing volumetric (3-D) imaging, and the recent technological improvement led to the development of 2-D probes. They are composed of hundreds (even thousands) of elements and can be based on matrix or sparse arrays, depending on how their elements are distributed. Matrices are composed by N×M transducers distributed as shown in Fig. 2-6, while sparse arrays follow an element distribution based on optimized geometry layout. Sparse arrays, in fact, aim at ensuring a good trade-off among sensitivity, secondary lobe levels, resolution[4]–[8], and number of elements.

## 2.3 Pulsed wave transmission

Modern ultrasound systems mainly use pulsed wave transmission modes. A transducer is used to transmit a short signal, called burst, and to receive the backscattered echoes. Transmissions are repeated at regular intervals, called pulse repetition interval (PRI). Nevertheless, typically, the system specifies the inverse of the PRI, i.e., the pulse repetition frequency (PRF).

Pulsed wave systems allow estimating the distance $d$ from the transducer to a scatterer, by measuring the time of flight $\Delta t$, i.e., the time gap passing from the transmission of the burst and the reception of the echo. Indeed, knowing the propagation speed $c$:

$$d = \frac{\Delta t \cdot c}{2} \qquad 2.14$$

However, since transmissions are regularly repeated, the maximum detectable time of flight, without ambiguity, is equal to the PRI, which correspondingly limits the maximum non-ambiguous distance or range $d_{max}$:

$$d_{max} = \frac{c}{2 \cdot PRF} \qquad 2.15$$

Moreover, during the transmission, the system cannot detect the weak backscattered echoes, therefore the minimum investigable distance $d_{min}$ is limited by the duration of the transmission burst *D*:

$$d_{min} = c \cdot D \qquad 2.16$$

In the range $[d_{min}, d_{max}]$, the system can process the echoes from either a single fixed window (or gate) or from multiple ones but placed at different depths; those systems are referred to as single-gate and multi-gate systems, as shown in Fig. 2-7.

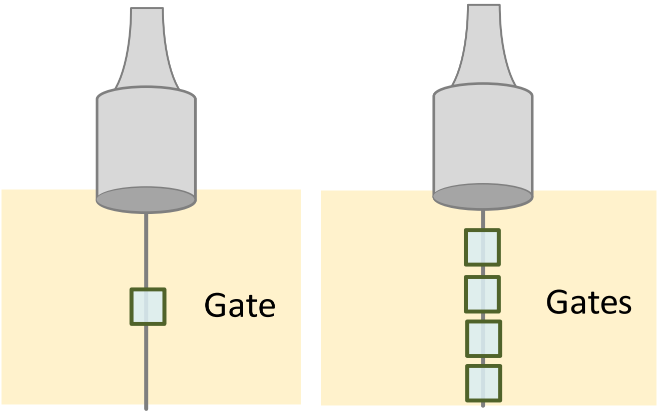

*Fig. 2-7 Single gate (left)and multigate (right) investigations*

The axial resolution is the smallest detectable distance between two targets placed on planes that are parallel to the transducer plane. It is proportional to transducer bandwidth. The lateral resolution is the smallest detectable distance between two targets placed on planes that are orthogonal to the transducer plane. It depends on the focalization, on the transducer geometry and on the transmission frequency.

## 2.4 Ultrasound systems for imaging

As sketched in Fig. 2-8 a system for ultrasound imaging is mainly composed of an ultrasound probe, used to transmit bursts and receive echoes, two analog sections for signal transmission and received echoes conditioning, a digital section for signal processing, and finally a back-end to display the results. The operations of all stages/sections are timely and suitably managed by a control unit.

It is worth highlighting that the analog sections, including the transmit/receive (TX/RX) switches and the analog-to-digital conversion stage, are replicated as many times as the number of channels of the system, which in turn defines the number of array elements that can be simultaneously and independently driven.

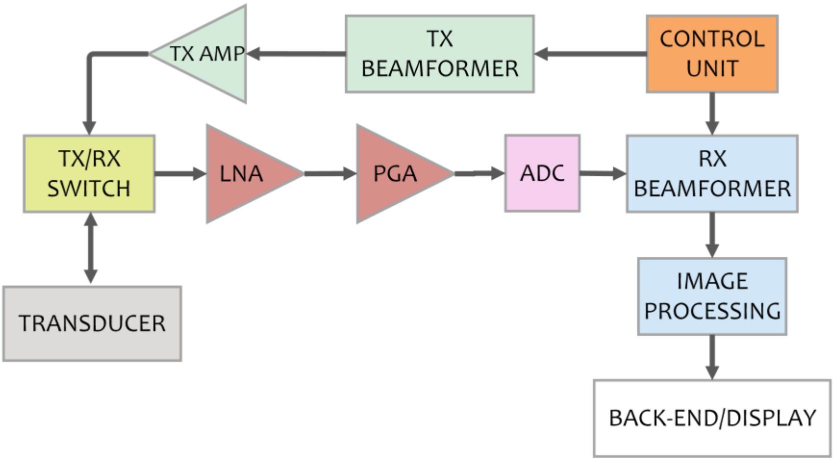

*Fig. 2-8 General architecture of an ultrasound system highlighting the transmission stage (green), the reception stage (red), the digital section (light blue) that are all managed by the control unit (orange).*

The transmission stage is typically composed by: a digital to analog converter (DAC) for each channel, which provide the waveforms programmed by the control unit and necessary for the excitation of the probe, a power amplifier for each channel, needed to achieve the necessary amplitude of the excitation signal, which is typically in the ±100V range. A TX/RX Switch, is necessary to send the transmission signals only to the probe, and avoid damaging the reception stage, and redirect the received echoes to the RX stage.

Since the received echo signals are very small (±10 mV), they must be amplified with Low Noise Amplifiers (LNAs). They are critical elements as they determine the overall noise introduced by the analog reception chain. Subsequently, the signal is amplified by a Programmable Gain Amplifiers (PGA), whose gain is increased during the reception phase to compensate the depth-dependent attenuation. This function is referred-to as Time Gain compensation (TGC). The signals appropriately conditioned are then converted by the analog-to-digital converter (ADC). Finally, the digitized data (also called Raw echo data) are processed by digital devices such as Field Programmable Gate Arrays (FPGAs), Digital Signal Processors (DSPs), Graphic Processing Units (GPUs ), and Personal Computers (PCs) that allow performing heavy processing operations, such as beamforming, demodulation and all the image processing in an efficient and quick way.

## 2.5 Scanning techniques

Array transducers allow imaging using various scan techniques that can vary depending on the application, the used probe, and the geometry of the imaging region.

The most commonly used scan sequences are linear and phased scan. In linear scan, several parallel view lines are reconstructed, to permit examining a rectangular region. Typically, it is used with linear arrays, where the active aperture, both in transmission and reception, is electronically moved to cover the entire array aperture. This method is particularly used for small region of interest, and when a high lines density is required.

In the phased scan, several lines are reconstructed with different steering angles to investigate a wide sectoral region. Typically, all elements are used both in transmission and reception to progressively steer the view line. Phased scan is used with small linear arrays, called phase arrays.

Recently, new high frame rate techniques became widely used to investigate rapidly moving phenomena with advanced imaging methods. HFR imaging methods minimize the number of transmission events required to reconstruct an image, thus maximizing the frame rate. With a single transmission a whole image or volume can be reconstructed. Typically, in HFR imaging, defocused wide beams are transmitted. Plane waves are typically used with linear arrays, while diverging waves with phased and convex arrays. Multiple plane or diverging waves are often transmitted with different steering angles and for each angle a low quality image is beamformed. Coherently compounding the low-quality images allows increasing the final image quality in terms of contrast, resolution, and signal-to-noise ratio, but reduces the achievable frame rate. Similarly, plane and diverging waves are used with 2-D probes to achieve high volume rates.

## 2.6 Imaging modes

The received ultrasound signals can be processed to extract information content, which is displayed according to different imaging modes. The most commonly used for diagnosis is B-Mode in combination with different Doppler modes.

The B-Mode (Brightness Mode) is used to show the morphological structure of the tissues over a bidimensional image. The beamformed signals are shown in grayscale, that relatively shows in black the absence of backscattered signal, and progressively in white, the tissues with stronger backscattered signals. An example is shown in Fig. 2-9.

Doppler imaging covers a key role in flow investigations. In pulsed wave systems, the system can evaluate the Doppler signal at a specific or at different depths by evaluating the phase differences between echo signals received after consecutive transmission events. Most of the

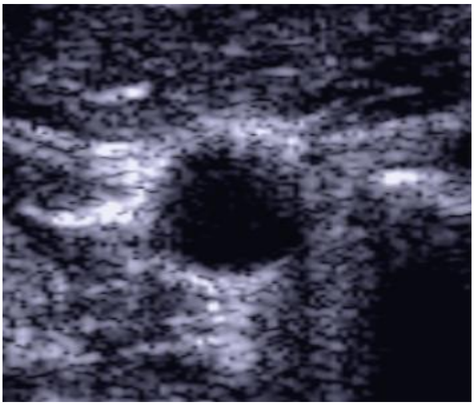

*Fig. 2-9 Example of B-Mode image showing a common carotid artery*

commercial ultrasound scanners performing Doppler analysis shows the so-called Sonogram, which displays the Doppler spectrum received for a single depth over time and, thus, provides the time-trend of blood velocity components as shown in Fig. 2-10.

Anyway, in recent years multiple advanced modalities to interpret flow information have been developed. Some of the most interesting, that have been also used in the next chapters are the Multigate Spectral Doppler, the Color Flow Imaging, and the Vector Doppler imaging.

The Multigate Spectral Doppler (MSD) technique is useful to show the flow temporal evolution at different depths (Fig. 2-11) along a Doppler line of interest. Color flow mapping (CFM) is an imaging technique that overlays to the anatomical image the blood flow velocity information. This method shows qualitative velocity information that are shown for a 2-D region of interest with a color map, typically with red and blue colors,

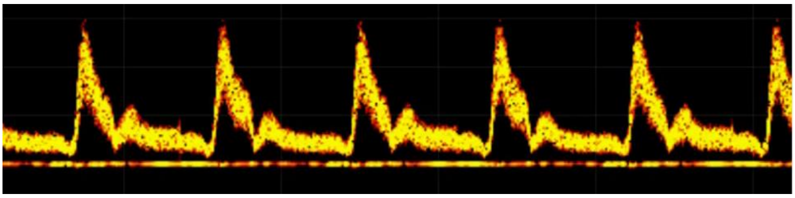

*Fig. 2-10 Doppler analysis provided through a spectrogram, which indicates the trend of the shift Doppler over time.*

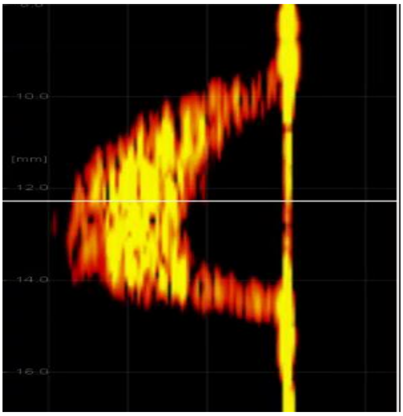

*Fig. 2-11 Example of parabolic flow profile produced by Multigate Spectral Doppler.*

which correspond to targets moving towards or away from the transducer, as showed in Fig. 2-12.

Finally, the vector Doppler imaging is a method that permits displaying flows with complex patterns, such as the flows produced by stenosis, bifurcation etc. over a 2-D region. This method shows both direction and module of the velocity, using a bidimensional map of vectors as shown in Fig. 2-13.

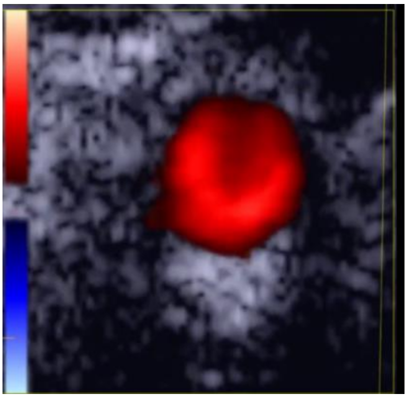

*Fig. 2-12 Example of color flow imaging investigating a carotid artery.*

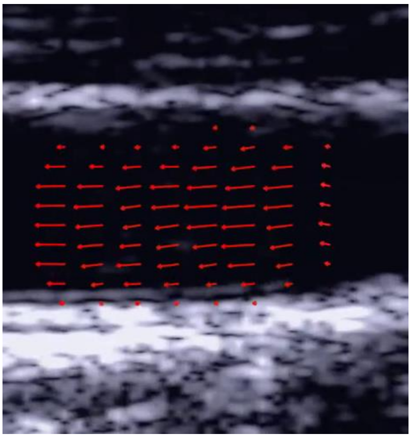

*Fig. 2-13 Example of vector Doppler image obtained investigating a carotid artery.*

# Chapter 3. Research scanner ULA-OP 256

*This chapter provides an overview of the research scanner ULA-OP 256 used for experiments and developments. The chapter shows the digital architecture and the main technical specifications of the scanner. This chapter is based on: ULA-OP 256: A 256-Channel Open Scanner for Development and Real-Time Implementation of New Ultrasound Methods* (10.1109/TUFFC.2016.2566920)

## 3.1 Introduction

There is an increasing need for ultrasound systems with high computational power and number of channels. For example, probes with hundreds or even thousands of transducers are required to electronically scan a volume, and they should ideally connect to systems with a correspondingly high number of input channels.

To implement and experiment novel ultrasound methods, the researchers use the open scanners, i.e., systems providing high performance and flexibility in terms of hardware (size, number of channels, probe supported etc..) and software/firmware/scripts programmability, as needed to efficiently implement custom methods.

In this PhD project a 256-channel research scanner, called ULA-OP 256 (ULtrasound Advanced Open Platform), was used (Fig. 3-1). The modular architecture of this system, based on multiple electronic boards, is briefly reviewed in the next sections.

*Fig. 3-1. ULtrasound Advanced Open Platform 256 (ULA-OP 256).*

## 3.2 Architecture

ULA-OP 256 is composed of 8 Front-end (FE) boards, each capable of managing 32 elements of the associated probe, a master control board that performs signal and image processing and communicates with a host PC, where a dedicated software runs. The clock of the system is generated on the backplane by a low-jitter phase-locked-loop (PLL) (AD9522-4, Analog Devices, Norwood, MA, USA), which is distributed to all the boards.

The number of FE boards installed on the system can be changed according to the needs: it is possible to use any number between 2 and 8 FE boards, thus enabling from 64 to 256 channels. The FE boards are physically interconnected through a backplane board, and digitally with a high-speed communication SerialRapidIO (SRIO) with a ring architecture, using 4 lanes at 5 Gbit/s, granting a bandwidth of 80Gbit/s full-duplex.

All the FE boards are connected to the Master Control (MC) board, and to a probe connector through the backplane as shown in Fig. 3-2. For a research system, the possibility of connecting a large variety of probes is very important but, unfortunately, the probes can have several types of connectors depending by the manufacturer. For that reason, the probe connector was placed on a dedicated board, so that the system can be

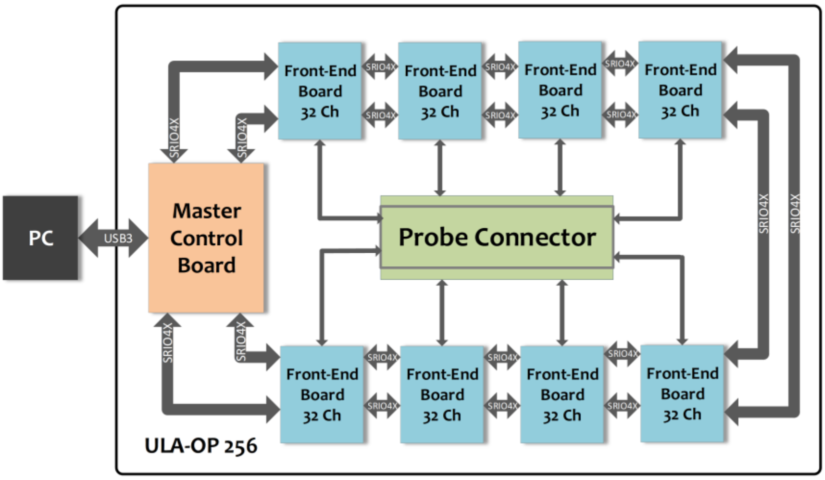

*Fig. 3-2 General architecture of the ULA-OP 256*

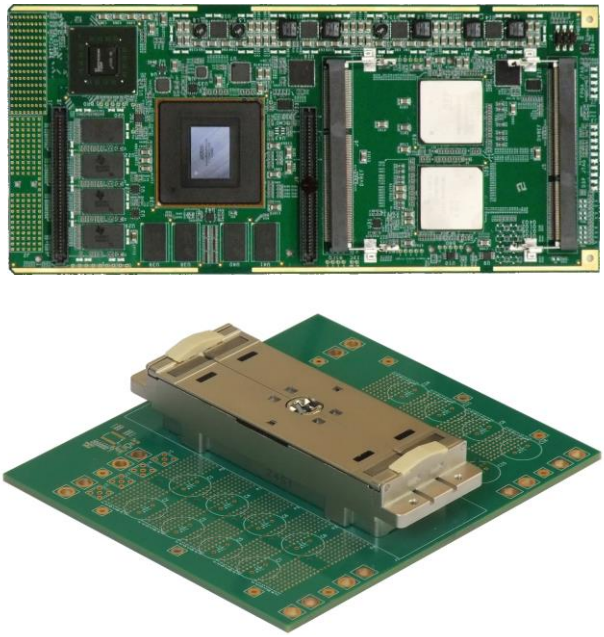

*Fig. 3-3 Two modular boards of the ULA-OP 256: a front-end board (top) and a probe board with the connectors for 256-element probes (bottom).*

adapted to any probe, even if its connector has a new pin-out, by re-designing only a specific probe board.

The MC board hosts an FPGA (Cyclone V SoC, Altera, San Jose, CA, USA) and a DSP (320C6678 family, Texas Instruments, Austin, TX, USA) running at 1.2 GHz, and 8GB of DD3 memory. The MC board also interfaces the scanner with the PC. The data coming from the FEs board are collected, possibly elaborated, and sent to the host PC with a USB 3.0 SuperSpeed connection that can sustain a transfer speed of 200 MB/s

## 3.3 Front-End board

Each Front-end board hosts the electronics to perform the transmission (TX), reception (RX), and real-time processing for 32 system channels. An FPGA (ARRIA V GX Family, Altera, San Jose, CA, USA) generates 32 bit-streams, that are sent to a board specifically used for TX, which converts each stream to an analog waveform signal that excites the elements of the probe. This board contains the transmission power

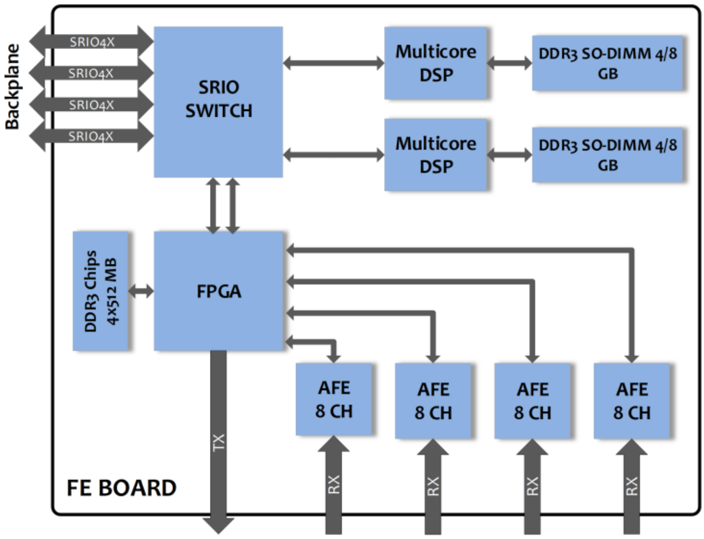

*Fig. 3-4 Block-diagram of the main devices of the FE board*

amplifiers and the T/R switches used to disconnect such amplifiers during the RX phase. The received echo-signals are amplified and converted at 78.125 MSPS with 12-bit resolution by 4 ultrasound analog front end integrated circuits of 8 channels each (AFE5807, Texas Instruments, Austin, TX, USA).

The digital data are elaborated by the FPGA, which performs the (partial) delay and sum (DAS) beamforming of the 32 acquired channels.

The two DSPs on the FE board (320C6678 family, Texas Instruments, Austin, TX, USA) perform coherent demodulation and filtering, and possible other custom elaborations that are implemented through its firmware.

The FEs have onboard two 4GB DDR3 Memory Modules, one per DSP, dedicated to store demodulated and post-beamforming data, while another 2GB Module is reserved to the FPGA, and dedicated to raw data storage (Fig. 3-4). Large memories are very important to transmit custom sequences, and to store and transfer to the PC the different types of data produced by the system: (raw unprocessed data, demodulated signals, and post beamformed data). For example, in the case of raw data, depending on the mode and the pulse repetition interval, it is possible to store 1-30 s of data. Table 3.I, summarizes the main characteristics of the scanner.

TABLE 3.I

ULA-OP 256 MAIN FEATURES

| | |
|---|---|
| **General features** | Open platform<br>8 FE boards, 32 to 256 total independent channels<br>Portable size: 34 × 30 × 26 cm |
| **Transmitter** | 32 to 256 arbitrary waveform generators based on a 468 Mbit/s sigma-delta bitstream<br>Max output voltages: 200 Vpp<br>Frequency: 1 to 20 MHz |
| **Receiver** | Bandwidth: 1 to 30 MHz<br>Analog Gain:<br>2 – 54 dB with 0 to 40dB programmable TGC<br>ADCs with 12-bit resolution @ 78.125 MSPS |
| **Beamformer** | Programmable apodization and delays (dynamic focusing delay and sum beamformer, with resolution of 1/16 of the sampling period) |
| **Processing modules** | Coherent demodulation, band-pass filtering, downsampling, B-mode, Multigate spectral Doppler, Color flow mapping, vector Doppler, etc<br>Possibility to create new custom modules |
| **Storage capabilities** | Up to 80 GB for RF (pre- or post- beamformed) and baseband data |

## 3.4 Software and firmware of the scanner

### *Software*

A dedicated and configurable software written in C++ is used to control and program the ULA-OP 256 from the PC (Fig. 3-5). In detail, the software schedules the startup of the hardware, interfaces the user with a graphic user interface (GUI), and shows in real-time output images. The imaging modalities can be set with text configuration files that can be customized by the user. Multiple display frames from different processing modules can be simultaneously shown on the screen. Also, the real-time

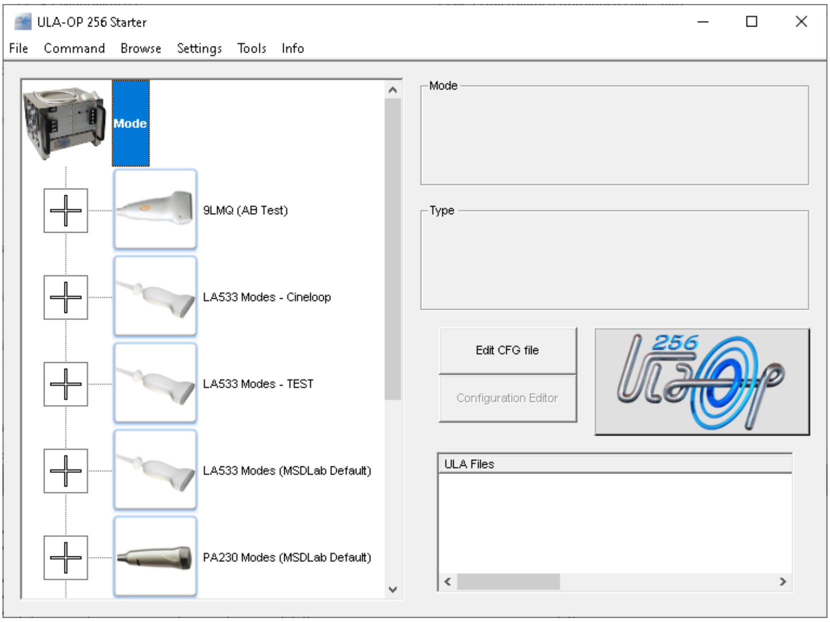

*Fig. 3-5 Start screen of the dedicated software of ULA-OP 256*

interface allows changing the pulse repetition frequency (PRF), saving the acquired signals, and setting on the fly various imaging parameters. At every PRI and through the USB link, the software communicates to the ULA-OP 256 the updated parameters, which are interpreted to correspondingly adjusts the parameters of the elaboration modules running on the FPGAs, DSPs, and the other devices.

### *Firmware*

The FE FPGAs are programmed with a firmware written in VHDL. It coordinates the operations of TX/RX devices and performs the partial beamforming of 32 channels. The raw data acquired from the echoes are stored in a buffer inside the FPGA, then read-out at 234MHz and used both for beamforming operation both for RAM saving, useful to save data for postprocessing and for the new virtual real-time modality shown in the next chapter. The beamforming implements a delay and sum (DAS) beamforming algorithm. Six DAS units can work in parallel to beamform multiple lines at the same time, moreover, each unit can be reprogrammed, within the same PRI, to reprocess the same raw data with different delay and apodization curves. Therefore, the system can beamform up to 1020 lines for each transmission event. Parallel beamforming is strictly necessary to perform High Frame Rate Imaging, producing thousands of frames per seconds.

DSPs on the FE boards are programmed with a dedicated firmware programmed in C. The FE DSPs receive beamformed data from the FE FPGA and perform in-phase quadrature demodulation, filtering, and downsampling. This samples are, finally, sent to the DSP of the MC board, where the final summation and the imaging modalities algorithm such as B-Mode, Doppler imaging, are performed.

# Chapter 4. Virtual real-time: a new ultrasound modality

*A new ultrasound modality so called Virtual Real-Time, useful to reprocess raw data has been introduced on the research scanner ULA-OP 256. In this chapter the proposed approach and two main application that exploited this modality are illustrated*

---

*The activity reported in this chapter resulted in the following publications:*

***Claudio Giangrossi** et al., "Virtual Real-Time for high PRF Multi Line Vector Doppler on ULA-OP 256," in IEEE Transactions on Ultrasonics, Ferroelectrics, and Frequency Control, vol. 68, no. 3, pp. 624-631, March 2021, doi: 10.1109/TUFFC.2020.3017940.*

*Francesco Guidi, **Claudio Giangrossi**, Alessandro Dallai, Alessandro Ramalli, Piero Tortoli, " High-frame-rate color flow imaging with enhanced spatial resolution in virtual real-time," 2021 IEEE International Ultrasonics Symposium (IUS), 2021, pp. 1-4, doi: 10.1109/IUS52206.2021.9593479.*

***Claudio Giangrossi**, Valentino Meacci, Enrico Boni, Alessandro Dallai, Francesco Guidi, Stefano Ricci, Alfred C. H. Yu, Piero Tortoli, "Virtual real-time: a new US operating modality," 2019 IEEE International Ultrasonics Symposium (IUS), Glasgow, United Kingdom, 2019, pp. 1493-1496, doi: 10.1109/ULTSYM.2019.8926259*

*Valentino Meacci, Stefano Ricci, **Claudio Giangrossi**, Riccardo Matera, Alessandro Dallai, Enrico Boni, Piero Tortoli, "High velocity investigation with Multi Line Vector Doppler," 2019 IEEE International Ultrasonics Symposium (IUS), Glasgow, United Kingdom, 2019, pp. 360-363, doi: 10.1109/ULTSYM.2019.8925613*

## 4.1 Introduction

Applications of High Frame Rate (HFR) imaging methods are increasingly popular due to their capability of acquiring phenomena in rapid evolution. The design and development of new high-performance systems capable of implementing HFR methods in real-time is a crucial challenge. Modern systems acquire frames at very high rates; however, the real-time elaboration of the corresponding massive amount of data, and the presentation on the display, present several challenges.

A large amount of raw data is generated after each transmission (TX) event. The exact amount depends on the number of active channels, the field of view and the analog-to-digital converter (ADC) sampling rate and resolution. Even when the number of active channels is limited to 128, the raw-data size may easily overtake 1 MB per TX event, which directly translates to a data rate of 10 GB/s for applications running at 10 kHz pulse repetition frequency (PRF) [9].

In case of HFR B-mode imaging it is possible to acquire (and process) frames at rates of hundreds or thousands of frame/s, but such rates are not reproducible on monitors and, in any case, the human eyes are not sensitive to such high frequencies. In addition, in demanding methods such as multigate spectral Doppler [10], 2-D Vector flow imaging [11], HFR color flow mapping [12], etc. the calculation power required to maintain kHz frame rates might not be sustained in real-time.

Also for basic real-time (RT) HFR B-Mode and Doppler imaging, [13], [14] enormous amount of data must be processed at very high speed. One of the most computationally intensive tasks that are involved, is represented by beamforming, which must produce multiple (N) lines in parallel for each TX event. This means that, e.g., the delay and sum procedure must be applied N times, with N different delay patterns, to the same radiofrequency (RF) echo-data received during each pulse repetition interval, i.e. at PRF rate.

Software-based open scanners [15], [16] which implement the signal processing chain through high-level programming [9], typically approach this problem by transmitting plane or diverging waves and acquiring raw echo-data in local random access memories (RAMs). The data are then sent, usually through PCI-express connection, to a PC containing powerful graphic processing units (GPUs) [17], [18]. In this approach, the results are typically viewed with some delay after the acquisition.

Hardware-based open scanners [9], [19], include computing devices such as field-programmable gate arrays (FPGAs) that, to some extent, allow RT processing the raw RF data. However, each machine and each application determine a trade-off between the parameters (e.g. field of view, image quality, temporal resolution, etc) that affect the final image

In this chapter the new Virtual real-time (VRT) approach is presented together with its implementation obtained programming the FPGA FE firmware and the software of the ultrasound research scanner ULA-OP 256 [20]. Raw data is here continuously stored on RAM during the RT investigation and processed according to the available on-board calculation power. With a simple command on the ULA-OP 256 graphic user interface, the system starts to re-process the saved raw data at the rate most suitable for full data processing and/or for the desired reproduction rate on the display. Moreover, the user can change any processing parameter compatible with the adopted TX strategy during acquisition. This on-demand approach to the processing of raw data is complementary to the slow-motion replay mode that is usually realized on software-oriented open platforms for HFR flow imaging [21].

### *Real-Time operations*

During an acquisition, in each FE board, the AFEs amplify, filter and digitize with 12-bit resolution and 78.125 MHz sampling rate, the echoes received by 32 probe elements, as previously mentioned in paragraph 3.3 . The digitized raw data are stored in a dual-port memory buffer implemented in the FPGA. The data are then sent from this buffer to the FPGA beamformer and, at the same time, to the on-board DDR RAM, which acts as a circular buffer memory (Fig. 4-1, top).

The dimension of the circular buffer RAM in the system is 16 GB, and for each of the 256 channels it is thus possible to store 62.5 MB of echo data. For example, if each image is derived from 256-channel raw echo-data of 2048 samples/channel/PRI, and 12-bit per sample, it is possible to store over 20000 frames.

In RT, the beamformer applies appropriate delays and apodization coefficients before operating the summation of 32 channel data. Thanks to a special serial-parallel architecture [22], the ULA-OP 256 beamformer can efficiently process the same data multiple times, as requested in HFR applications. Accordingly, the longer is the pulse repetition interval, the higher is the number of lines that can be beamformed in real-time by re-processing the same data.

The beamformed data can be demodulated and further processed by the back-end DSPs according to the running application. The data produced by the different FE boards are finally combined on the MC board before being transferred to the host PC for real-time display. At the same time, the raw data continue to be stored into the DDR RAM buffer, so that the operator can anytime download them to the host PC, where they become available for possible off-line processing.

## 4.2 Virtual Real-Time operations

The firmware architecture of the FE FPGA, and the PC software of the scanner have been modified to introduce the possibility of running the “virtual” real-time modality in addition to the real-time modality.

At any time, the user can press a button on the PC graphical interface (GUI) to switch the scanner to VRT mode. When VRT is started, the data flow from the AFEs is interrupted, and the raw channel data previously stored in the DDR circular buffer are transferred to the internal FPGA dual-port buffer (Fig. 4-1, bottom). The data are then elaborated by the same scanner computing devices (FPGAs and DSPs) used in real-time (i.e., the scanner resources ignore the data origin).

The same (application-dependent) group of parameters that are available on the GUI during RT operations can be configured in VRT as well. Any setting compatible with the implemented TX-RX strategy can be changed with respect to that used in RT. In particular, all data stored in the DDR memory at PRF rate, can be read-out at a different rate, which will be hereinafter called Virtual PRF (VPRF). This rate change can be

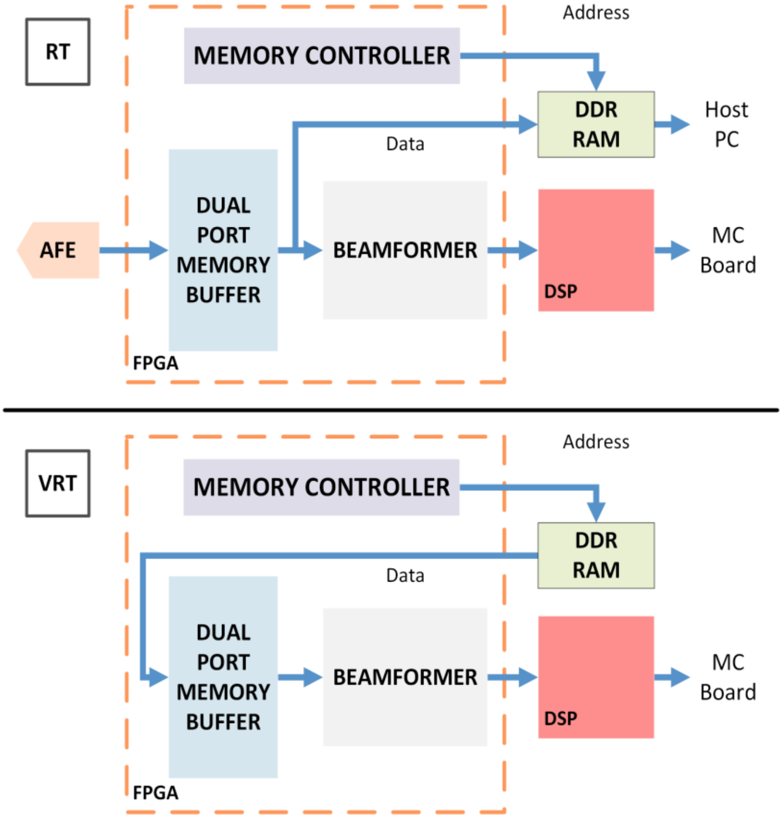

*Fig. 4-1: Data flow in the FE boards of ULA-OP 256. In real-time (top), the data acquired by analog front-end (AFE) integrated circuits are fed into the dual-port memory buffer and then simultaneously distributed to the beamformer and to the external DDR RAM. In VRT (bottom), channel data are loaded from the RAM into the dual-port memory buffer.*

useful, for example, when the frame rate of the monitor is not high enough to show all available frames (e.g., during HFR acquisitions). Echo data producing, e.g., 1000 frames/s, can be read out at a rate 20-fold lower (50 Hz), so that all frames (obtained with the same processing steps adopted in real-time) turn out to be visible. An example of such capability is shown in the second example of paragraph 4.2.1 .

The possibility of configuring ULA-OP 256 with different parameters during RT and VRT operations, respectively, can be fruitfully exploited in applications that in real-time would require a processing power beyond the hardware capabilities. In this case, the RT operating parameters must be set so that the required calculation power results compatible with the available hardware resources. For example, a computationally intensive technique can be applied, in RT, only for one part of the points available in the DDR RAM. After switching to VRT mode, the data management is programmed to slow-down the extraction of channel data from the DDR memory so that the hardware has sufficient time to complete the calculations all over the desired region of interest (ROI).

### 4.2.1 Preliminary results

In this section, two examples illustrate how the new VRT modality works. Two applications are then reported in detail in the following two sections 4.3 and 4.4

#### *Multigate spectral Doppler*

Multigate spectral Doppler (MSD) [10], [23] is a method that allows displaying in real time the distribution of Doppler frequencies generated by scatterers at different depths from the probe. In RT, with ULA-OP 256 [9] it is possible to show such distribution together with the B-Mode images, as well as the spectrogram originated from a selected depth. For example, Fig. 4-2 shows, on the top panel, a RT screenshot in which the frequency baseline of the MSD distribution was wrongly set (so that aliasing effects are produced) and the sonogram was extracted from a depth corresponding to tissue. In VRT (bottom panel), it was possible to correct the baseline visualization and to select a suitable depth for the sonogram to be displayed (data reprocessing). Furthermore, it would be possible to change parameters like the dynamics and the threshold of the profile, change the type of FFT windows, apply a video filter, change the B-Mode dynamics and threshold.

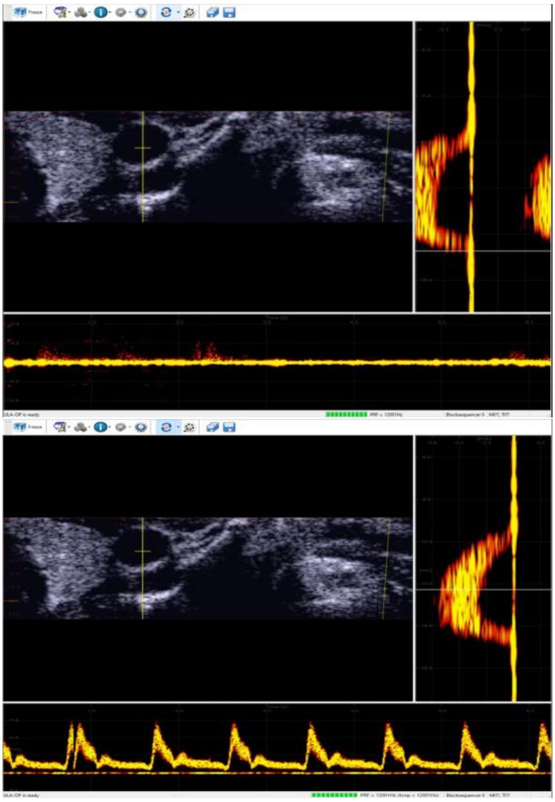

*Fig. 4-2 Screenshots from the ULA-OP 256 display investigating a carotid with Multigate spectral Doppler. Each panel shows the Doppler scan line superimposed to the B-Mode image (left), the MSD profile (right) with the white line indicating the depth form which the sonogram (bottom of each panel) was extracted. The MSD baseline and the sonogram depth were wrongly set in RT mode (top) and correctly set in VRT (bottom)*

### *HFR plane wave imaging*

ULA-OP 256 can produce in real-time HFR images based on plane wave transmission [22]. The frame undersampling caused by the monitor is usually so high that the advantage of having frames at high rates is lost, and possible high-speed tissue movements, such as those present in the cardiac walls, cannot be appreciated. However, with VRT all frames can be displayed and seen by the operator.

In this test, a linear probe, LA533, was immersed in a tank full of water. A metal tip was rapidly moved in front of the probe while imaged by the

*Fig. 4-3 Superimposed monitor frames describing the trajectory of a metal tip in RT (top) and in VRT (bottom) HFR modes*

scanner over a duration of 200 ms. Plane waves were transmitted, and the echoes processed in RT to produce 500 frames per second. Each frame included 96 lines each of 2700 RF samples. The top of Fig. 4-3 was obtained by superimposing all the frames displayed on the monitor during the 200 ms tip movement. The bottom of Fig. 4-3 shows, superimposed, all the frames displayed on the monitor when the same raw data were reprocessed in VRT, at a 12-times lower VPRF. While in RT it is impossible to appreciate the movements of the tip, in VRT the trajectory is neatly reproduced.

## 4.3 Application to high PRF multiline vector Doppler

In Doppler modes such as spectral Doppler [24], color flow mapping [24], vector [11], [25]–[28] or speckle [29], [30] imaging, a lot of computationally intensive tasks must be performed, in addition, a further constraint is represented by the PRF, which is directly correlated to the maximum detectable velocity.

ULA-OP 256 [20], was recently programmed to estimate, through the TX of plane waves, eight vector Doppler lines [28] (multi-line vector Doppler, MLVD). However, the calculation effort for generating vector velocities over a 2 cm deep region, has limited the maximum PRF to 7 kHz. As a consequence, when high velocities have to be investigated (e.g. the velocities originated by stenotic plaques in carotid bifurcations [31]), the vector Doppler exploration likely involves aliasing [24], [32], [33].

The purpose of this application is to use the virtual real-time modality (VRT) [34], with multiline vector Doppler mode. In this paragraph will be shown that the VRT is the ideal approach to implement a high-PRF version of the MLVD technique [35].

Now it will be reported the basics of MLVD method, which is described in more detail in reference [28]. Velocity vectors are calculated along 8 Doppler lines perpendicular to the probe surface. The lines are spaced by 1.225 mm, so that they cover a ROI of about 1 cm of lateral extension.

A linear array probe insonifies the ROI by transmitting plane waves at PRF rate. In reception, the probe is divided into 8 pairs of sub-apertures (16 sub-apertures), each couple of sub-apertures, $A_R(k)$ and $A_L(k)$ ($1 \le k \le 8$), being symmetrically located on the two sides of the corresponding vector Doppler line (see Fig. 4-4). Note that while the sub-apertures $A_R(k)$ and $A_L(k)$ are not overlapped to each other, they are partially overlapped to the sub-apertures $A_R(k+1)$ and $A_L(k+1)$ used for the adjacent line.

A scatterer moving with velocity $V$ at depth $d$, produces echoes that are received by the aperture's pairs and dynamically beamformed along each Doppler line in the FE FPGA. Then, data from the left and right apertures are processed in the back-end through coherent demodulation, wall filtering and spectral analysis. The mean Doppler shifts, $f_{dl}$ and $f_{dr}$, are computed by calculating the centroid of each Doppler spectrum. The lateral ($V_x$) and axial ($V_z$) components of the velocity vector are calculated by the trigonometric triangulation [36]:

$$V_x = \frac{c}{2f_{tx}} \frac{f_{dr} - f_{dl}}{\sin\theta_{rx}}, V_z = \frac{c}{2f_{tx}} \frac{f_{dr} + f_{dl}}{1 + \cos\theta_{rx}} \qquad 4.1$$

where $c$ and $f_{tx}$ are the sound velocity and transmission frequency, respectively, and $\theta_{rx}$ is the receiving angle, which depends on the depth $d$ [37]. The velocity vector is finally obtained as:

$$V = \sqrt{{V_x}^2 + {V_z}^2} \quad ; \quad \alpha = \angle(V_x, V_z), \qquad 4.2$$

where $V$ is the vector amplitude and $\alpha$ is the angle. An example of MLVD real-time display, reporting the analysis of the common carotid artery in a volunteer, is reported in Fig. 4-5.

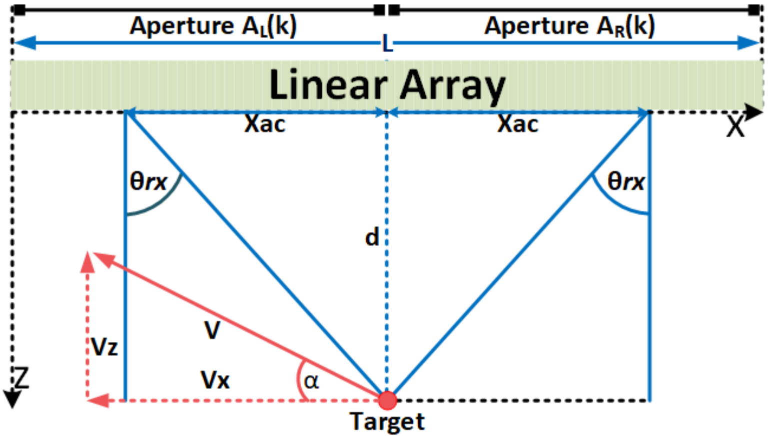

*Fig. 4-4 Ultrasound probe apertures and geometry used for Multi Line Vector Doppler.*

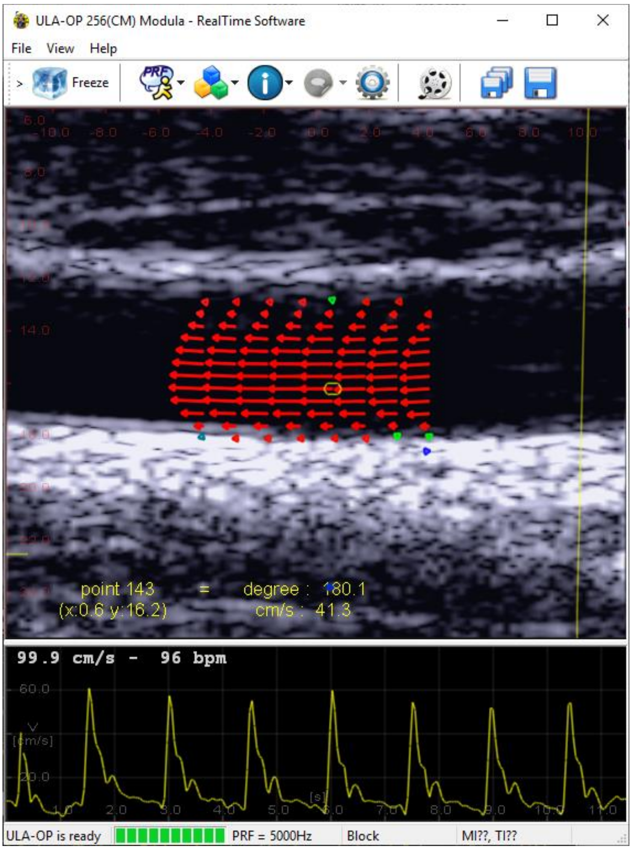

point 143 = degree : 180.1
(x:0.6 y:16.2) cm/s : 41.3

99.9 cm/s - 96 bpm

ULA-OP is ready

PRF = 5000Hz

MI??, TI??

*Fig. 4-5 : Sample screenshot of ULA-OP 256 real-time display with MLVD while investigating the carotid artery of a volunteer at PRF = 5.0 kHz. The top panel shows the velocity vectors distributed in the 8 lines, while the bottom panel shows the angle corrected velocity at the cursor (yellow circle) position.*

MLVD was implemented by repeating a transmission sequence composed by 64 plane waves followed by 96 focused lines. The focused lines were used for presenting live B-mode images on the background of the MLVD (see Fig. 4-5). A vector map frame was calculated from the plane waves (packet size: 64). Thus, PRF/(64+96) MLVD+B-mode frames were produced every second. The Doppler vectors were estimated at 256 depths. The data were filtered along both fast and slow time before being 4-fold decimated in the final display. Thus, the system calculated a number of vectors-per-second equal to:

$$Vec/s = \frac{PRF}{64+96} \cdot 256 \cdot 8 = 12.8 \cdot PRF \qquad 4.3$$

The calculation effort here neglected the B-mode processing in addition to (Eq. 4.3), since its contribution is much lower.

The VRT architecture has been used to extend the PRF range usable during MLVD acquisitions. During real-time, the ULA-OP 256 computing devices calculated only one vector line (1LVD) [37], while the scanner

TABLE 4.I
TX / RX MLVD PARAMETERS USED IN EXPERIMENT

| **Parameter** | **Symbol** | **Value** |
|---|---|---|
| PROBE | | |
| Type | | Linear |
| Elements | | 192 |
| Element Pitch | | 0.245 mm |
| 6 dB Band | | 3.25 – 12.75 MHz |
| MLVD TX | | |
| Frequency | $f_{Tx}$ | 8 MHz |
| Transmission cycles | N | 5 |
| Apodization window | | Tukey |
| Pulse Repetition Freq. | PRF | 16 kHz (exp. 4.3.1A)<br>15 kHz (exp. 4.3.1B) |
| TX Aperture | | 31.36 mm (128 el.) |
| Mode | | Plane Wave |
| MLVD RX | | |
| Lines | k | 1-8 |
| IL pitch | | 1.225 mm |
| RX Aperture | $A_{RX}$ | 18.8 mm |
| RX Sub-Apertures | $A_L(k)$, | 7.8 mm (32 el.) |
| Relative Aperture | Xac | 5.48 mm |
| Steering angle | $\theta_{rx}$ | 14° @ 22mm (exp. 4.3.1A)<br>14° @ 30mm (exp. 4.3.1B) |
| Focalization | | Dynamic |
| Aperture ratio | F# | 5 |
| Sampling Freq. | $F_S$ | 78.125 MHz |
| Packet size | | 64 |

continued to save in the DDR RAM all channel data. Such reduction of the calculation effort allowed the scanner to work at higher PRF.

The real-time 1LVD display allowed the user to select a significant ROI. Then, the scanner was switched to VRT mode. By reloading the raw data from the RAM at a slower rate, VPRF, the scanner had enough time to process in-line all the 8 Doppler lines.

### 4.3.1 Experiments and results

#### *A) Syringe flow jet*

MLVD with VRT was first tested through the investigation of the high velocity flow jet produced by a syringe. The experiment was aimed at measuring the maximum detectable velocity.

ULA-OP 256 was connected to the LA533 linear array probe (Esaote spa, Florence, Italy) and worked with the parameter set summarized in Table 4.I. A tank was filled with water and a syringe was installed at the border, 15 mm below the water surface. (see Fig. 4-6). The probe was located over the syringe tip so to longitudinally intercept the flow jet. The

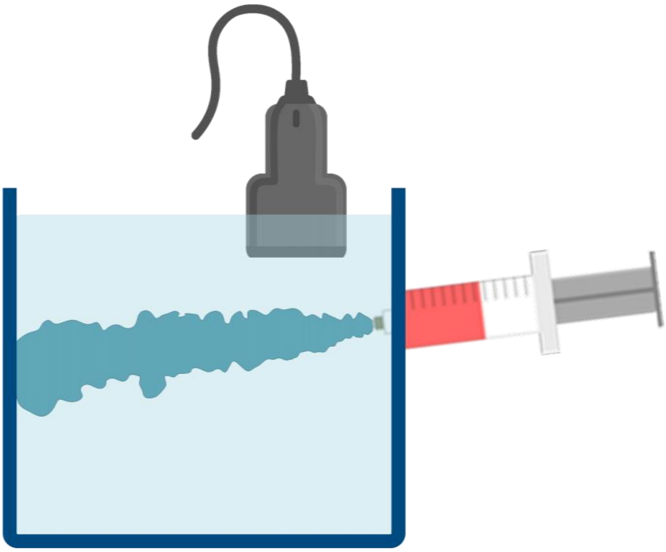

*Fig. 4-6 Experimental setup: The ultrasound probe was immersed in a water tank to intercept the high velocity jet of blood mimicking fluid ejected from an external syringe.*

syringe had a tip diameter of 4 mm and was filled with 150 ml of water mixed with corn starch. The syringe piston was manually pressed to eject the mixture in the tank. A sequence of tests was carried out in which the jet velocities were increased until the aliasing limit was achieved.

During the acquisition, ULA-OP 256 processed in real-time the data to display a single vector Doppler line superimposed to a B-mode image. In this phase, the PRF was set at 16 kHz.

A sample screenshot taken from the real-time 1LVD display is shown in Fig. 4-7A. The syringe’s tip is clearly discernable on the right of the figure. The jet crosses the vector Doppler line at about 1 cm from the tip, where a roughly parabolic profile is detected.

ULA-OP 256 was then switched to VRT mode to reprocess the saved raw data. The reproduction rate was here slowed-down 5-fold (VPRF=3.2 kHz). In this condition ULA-OP was able to calculate 8 vector Doppler lines. Fig. 4-7B shows a screenshot taken during VRT reproduction. Here the flow spatial distribution was detected by 8 vector Doppler lines

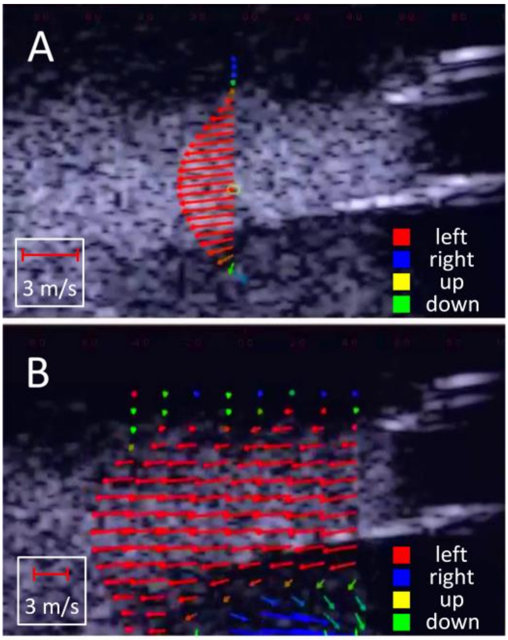

*Fig. 4-7 Screenshots from the ULA-OP 256 scanner while investigating with MLVD a 3 m/s jet produced by a syringe. A: Real-time 1LVD is superimposed to B-mode at PRF=16 kHz; B: VRT MLVD at 8 vector Doppler lines is superimposed to the B-mode.*

covering 1 cm of lateral extension. A vortex is clearly visible in the region below the jet. The velocity scale between real-time and VRT was changed by the user to improve the display readability. In both modalities the peak velocity of about 3m/s was detected without aliasing.

### *B) Anthropomorphic phantom*

To evaluate the method performance in a more realistic condition, a wall-less phantom of a stenotic carotid bifurcation was used. The second experiment was based on a wall-less anthropomorphic phantom reproducing the carotid artery bifurcation. The phantom was casted with polyvinyl alcohol cryogel and featured 120 kPa elastic modulus, 1518 m/s sound speed and 0.24 dB/(cm·MHz) attenuation [38]. A 50% eccentric stenosis was present at the entrance of the internal branch (see Fig. 4-9). The stenosis is co-planar to the bifurcation geometry and the diameters of the common, internal, and external carotid artery branches are 6 mm, 3 mm, and 4 mm, respectively. The LA533 probe was positioned over the phantom in correspondence of the bifurcation plane (see Fig. 4-8)

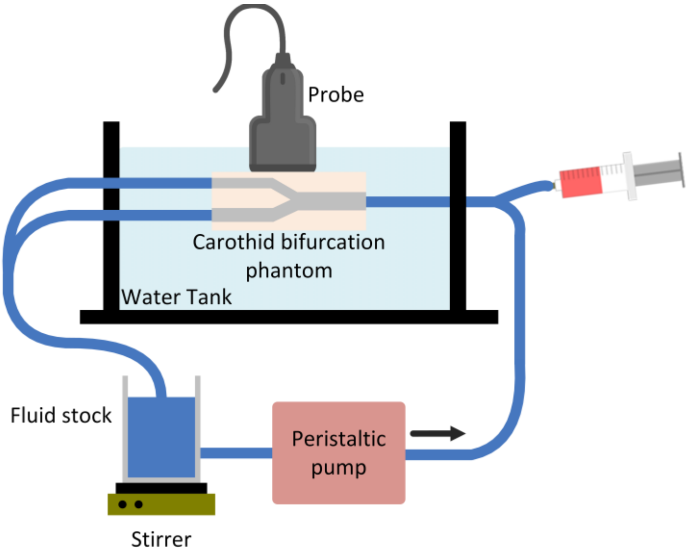

*Fig. 4-8 Experimental setup: the probe is positioned over the phantom in correspondence of the bifurcation plane A blood mimicking fluid (BMF) was forced by a peristaltic pump to circulate at steady velocity. The syringe, loaded with the BMF, was manually pressed to create transient high-velocity jets in the stenosis*

A blood mimicking fluid (BMF) was forced by a peristaltic pump (Watson-Marlow Pumps Group, Falmouth, UK) to circulate in the phantom at steady velocity. The BMF was obtained by dissolving 3 g of Orgasol® particles in 2 l of demineralized water [39]. Since the pump was not able to produce high velocity jets, a piston syringe was added to the hydraulic circuit. In this way, while the pump produced a steady flow, the syringe, loaded with the BMF, was manually pressed to create transient high-velocity jets in the stenosis.

The ULA-OP 256 was programmed to generate the same TX/RX sequences described in 4.3.1 A. During the experiment, the ULA-OP 256 display was captured and saved (a screenshot is reported in Fig. 4-9). The PRF was here set to 15 kHz.

The investigation of the bifurcation started using 1LVD (RT) mode. In this phase, as visible on the left panel of Fig. 4-9, a single Doppler line was superimposed to the B-mode image of the phantom.

Then the operator switched the ULA-OP 256 to VRT mode, and set the VPRF to 2.5 kHz, which corresponds to a data rate slowed down 6-fold with respect to the acquisition PRF. The right panel of Fig. 4-9 correspondingly shows 8 vector Doppler lines superimposed to the B-mode. This display covers an extended region and allows to better

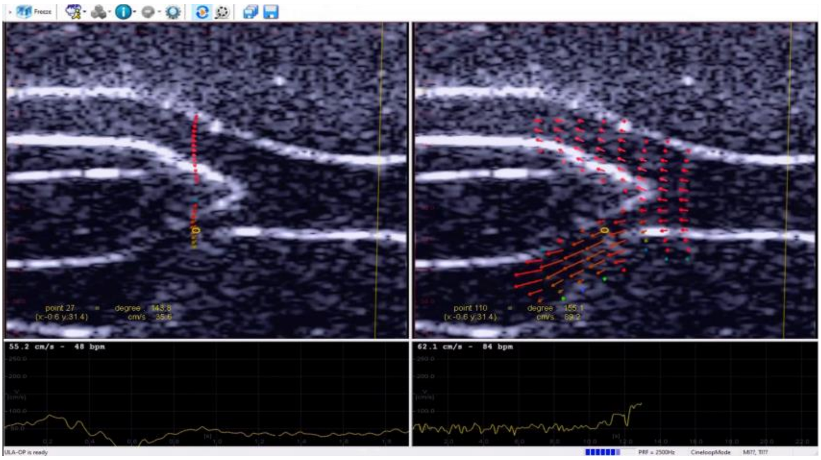

*Fig. 4-9 Screenshots from the ULA-OP 256 scanner while investigating with MLVD the anthropomorphic phantom. On the left side, the real-time 1LVD is superimposed to B-mode at PRF=15kHz; On the right side: in VRT, 8 vector Doppler lines are superimposed to B-mode.*

appreciate the flow spatial distribution and temporal evolution, especially during the jet transient.

In Fig. 4-9, the bottom panels show the angle corrected velocity detected in the stenosis, at the position highlighted by the yellow circle. The measuring point can be changed by the user during RT operation as well as during VRT reproduction. In this test, the background steady velocity detected in the measuring point was 50 cm/s. During the jet, the local velocity increased up to 125 cm/s. After the jet, a significant velocity reduction was measured. This was probably due to backpressure generated by the phantom elastic tissue after the jet pressure stress.

The accuracy and precision of the MLVD method have been already reported in [28]. The VRT modality is not expected to affect these parameters in any way. In fact, the TX/RX strategy and data processing are the same described in [28], the only difference being that for VRT data are acquired and processed at different times.

The parameter configurations (see Table 4.I) were verified in the proposed experiments. The first test highlighted that limiting the real-time calculation to 1LVD, raw data can be acquired at PRF as high as 16 kHz and, in VRT, can be MLVD-processed at a suitable VPRF value and finally displayed. With the jet slightly angled with respect to the transducer (see Fig. 4-6) a velocity of 3m/s was detected without aliasing. However, the maximum detectable velocity in practical situation strongly depends on the Doppler angle. The staggered PRF techniques [33], already tested with MLVD [40], could contribute to further extend the maximum detectable velocity.

The second experiment of this application verified the method behavior in a real-like condition. The VRT modality is accessed with a simple command and VRT is immediately available without the need of further operations as data download or off-line processing. This experiment also suggests the use in the clinical scenario. In RT the operator can position the probe on the patient and perform a first evaluation of flow conditions, while in VRT high quality flow visualization and accurate estimate of the velocities can be immediately performed.

## 4.4 Application to high frame rate color Doppler imaging

The color flow mapping (CFM) technique is widely used to quickly localize blood vessels and possible flow abnormalities [12], [41]. It is well known that its main limitations consist in the low attainable accuracy and frame-rate. These limitations arise from the need to transmit multiple pulses, typically 6-20, for each scan line of the region of interest (ROI). A low number of received pulses per line limits the ability to accurately estimate the speed, involves a poor signal-to-noise ratio and dramatically reduces the effectiveness of high-pass filters (HPFs) for clutter removal. Moreover, the transmission sequence may reduce so much the final frame-rate that possible rapid changes in blood flow velocity (e.g. transient reverse flow components) cannot be properly detected. Besides, since different lines in the ROI are scanned at different times, the color box might simultaneously show different colors (i.e., velocities) that correspond to different phases of the heart cycle.

HFR methods [42]–[44] enable CFM to operate on continuous sampled data. In this way, clutter can be reduced by more effective HPFs [42], [45] longer ensemble lengths (*EL*) can be used to increase the estimation accuracy.

Since these techniques require the availability of a high computing power, most research systems implement the so called "retrospective modality", which off-line post-processes acquired data but prevents immediate feedback about the effectiveness of a novel approach. Few systems are also capable of real-time processing [21], [46] but typically with limited frame-rate.

In this application a method is presented to perform high-speed continuous data acquisition and CFM processing in real-time (RT) at Doppler PRFs up to 4.3 kHz [47]. The same raw data are also processed in “virtual real-time” (VRT) over an extended ROI, i.e., with a bigger size and a finer spatial resolution. Three sample applications showing the possibility of increasing either the frame rate, the ROI size or the spatial resolution will be shown in this paragraph.

### *CFM processing*

In both RT and VRT modalities, beamformed data are in-phase quadrature (I/Q) demodulated, low-pass filtered, and down-sampled by two digital signal processors present in each FE board. The same DSPs can also perform coherent Plane Wave compounding to produce high-resolution B-Mode images by the combination of echo-data obtained at multiple transmission angles.

The I/Q data are sent to the MC board where an 8-core DSP performs all subsequent operations. The first core completes the beamforming by adding the samples produced by all active FE boards. The resulting I/Q data streams are then stored in a new circular buffer allocated in an external memory. The second DSP core acts as a master and distributes the beamformed data to the remaining 6 cores, each dedicated to process one line, until all the $N_L$ lines within the ROI are processed. For each of the $N_G$ depths in the ROI, such data are organized in groups of $EL$ complex samples, within the ROI.

The samples are high-pass filtered by a continuous time 4-th order infinite impulse response (IIR) filter [47], whose cutoff frequency can be selected by the user in the range [0.012; 0.4]×PRF. For each group of $EL$ samples, the average power is calculated before and after the high-pass filter. The autocorrelation of the filtered samples, within the group, is computed together with the relative standard deviation $RSD = \frac{\sigma}{|\mu|}$, where $\sigma$ and $\mu$ are the autocorrelation standard deviation and mean, respectively. The complex autocorrelation output is then low-pass filtered, in both space and time. The first one was implemented as a 3×3 Gaussian filter. Each sample produced by the spatial filter is then sent to a 1-st order IIR filter working across slow-time. Finally, the phase and the power of the filtered autocorrelation are calculated for any point within the ROI. The autocorrelation power is non-linearly combined with the input signal power, the autocorrelation RSD, and the estimated phase, to generate a pixel transparency map.

Both phase and transparency maps are sent back to the master core, which operates a final 3×3 median filtering before sending the phase and the pixel transparency maps to the PC. Here, the CFM frames are color-coded in blue-red scale, combined with the B-Mode layer, and finally displayed at a rate of PRF/*EL* frames/s.

The implemented software is fully parametric and allows setting the number of lines ($N_L \leq 128$) and the number of depths ($N_G \leq 256$) within the color ROI, the wall filter corner frequency, the ensemble length ($EL = [3; 64]$) and the transparency thresholds, according to the application [47].

The ULA-OP 256 was set to transmit PWs or steered PWs and to continuously acquire the pre-beamforming samples over a ROI as large as possible considering the available memory. At the same time, the system was configured to produce in RT both B-mode and CFM frames over the same ROI.

During RT operations, when an interesting flow behavior is observed, the system can be frozen and immediately switched to the VRT mode. In this case, the raw data are reprocessed at a reduced processing rate to allow tuning the VRT extended ROI (size, resolution, position) and the processing parameters (including *EL*, wall filters, thresholds) thus maximizing the output display information. For example, fast or turbulent flows can be better observed in slow motion, and by reducing the *EL* size to improve the CFM temporal resolution. At the same time, the image quality can be recovered by tuning the persistence filter cut-off frequency.

### 4.4.1 Experiments and results

Fig. 4-10 shows a screenshot of the system user-interface, in which the RT and the VRT CFM frames are on the left and right window, respectively. The system was here configured to transmit 6 MHz 6-cycle PW pulses from 128 elements of a LA533 (Esaote, Florence, Italy) linear array probe, with a PRF of 3.6 kHz. The RT CFM processing was performed over a ROI with $N_L = 64$, $N_G = 128$, and at $EL = 32$. This configuration resulted in a RT frame-rate of 112 CFM frames/s. In VRT mode, the same ROI was reconstructed, but an equivalent rate of 900 frames/s by setting $EL = 4$ which allowed to obtain one frame every 1.1 ms. This mode is ideal to reprocess an investigations of rapidly changing

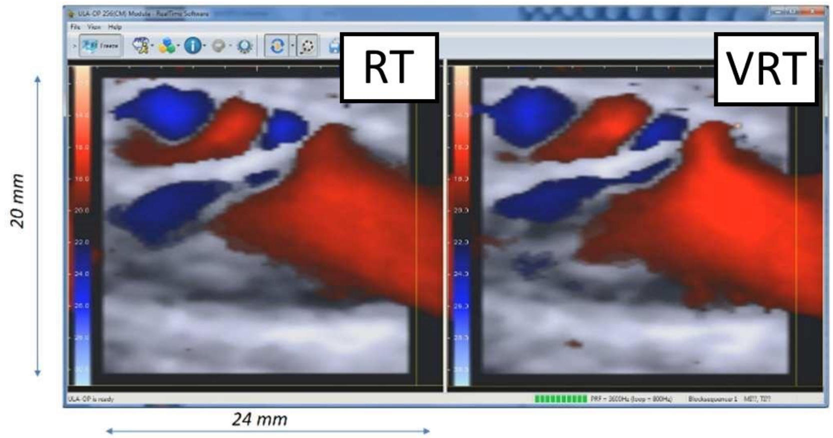

*Fig. 4-10 ULA-OP 256 software screenshot showing RT (left) and VRT (right) CFM images over the same 20x24 mm ROI extention.*

flow with different settings and at a lower reproduction rate, enabled by reducing the virtual PRF from 3.6 kHz (used in RT mode) to 200 Hz.

Fig. 4-11 shows a screenshot obtained when the system was programmed to transmit 6 MHz PW pulses from 128 elements at 4 kHz PRF. Here, the beamformer computing power allowed processing a ROI of $N_L = 64$ and $N_G = 128$ scanning and area of 13×16 mm$^2$. In this case, $EL$ was 16 for a RT frame-rate of 250 frames/s.

In VRT different reception parameters were set to process a matrix of 128×256 points to cover, with the same spatial resolution, a 4-time larger area, i.e., 26×32 mm$^2$. Of course, in this case, the system should be previously configured to acquire also the pre-beamforming samples needed for the larger ROI. In Fig. 4-11, the yellow dashed box on the right panel highlights the position of RT ROI. This mode is ideal for the slow-motion investigation of rapidly changing flows on extended ROIs.

Fig. 4-12 shows the result obtained by transmitting, with a PRF of 4.3 kHz, sequences of three 9 MHz PWs tilted with 5°, 0° +5°, respectively. The Doppler PRF was 1.4 kHz. The echo-data were beamformed and coherently compounded in RT for $N_L = 64$, $N_G = 128$, and $EL = 16$, covering an area of 15×32 mm$^2$. The same ROI area was reprocessed in VRT using

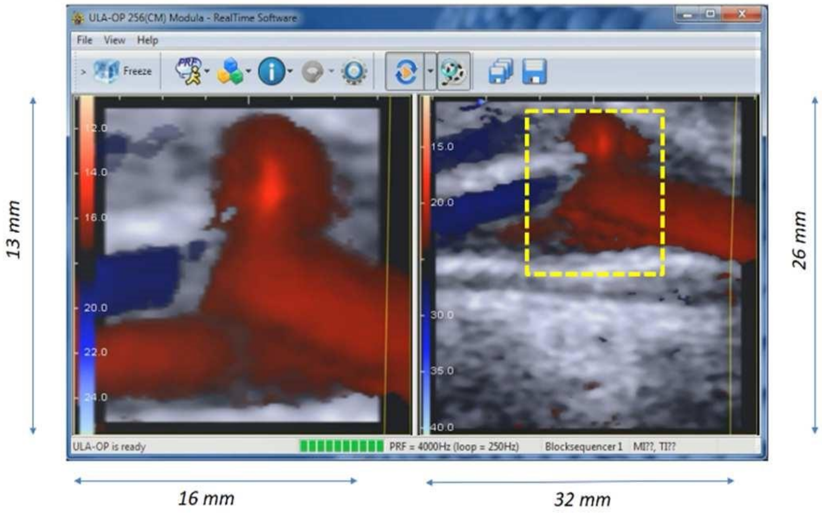

*Fig. 4-11 ULA-OP 256 software screenshot, showing the RT (left) and VRT (right) CFM frames. The dashed yellow box highlighted the of the RT ROI dimension and position*

an identical processing setup but doubling the horizontal and vertical sampling steps on a matrix of 128×256 points. In this way, the same region was explored with improved resolution, while maintaining an appropriate PRF for the application.

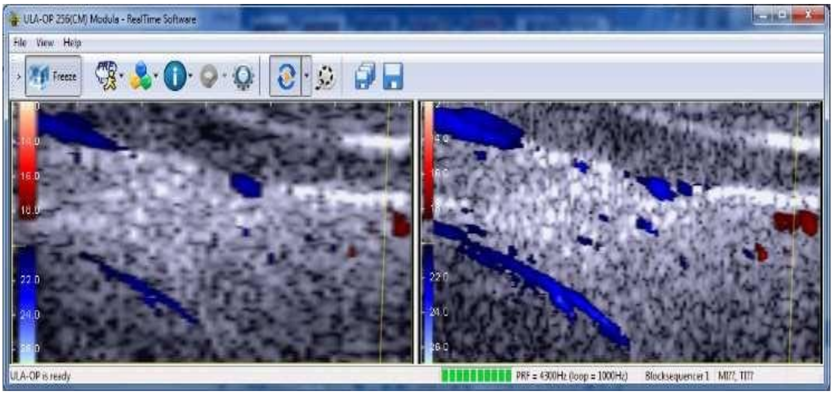

*Fig. 4-12 Investigation of small vessels in the thyroid region, performed at PRF=4.3 kHz. Screenshot of RT (left) and VRT (right) display. The ROI was the same but with a 4-fold number of points in the latter case (128×256 instead of 64×128).*

## 4.5 Discussion and conclusion

The recent development of HFR methods based on plane or diverging wave TX, has opened new exciting scenarios but has, at the same time, proposed new challenges in echographic data management and display.

Different approaches have been proposed to extract as much information as possible from the massive data amount produced by the front-end electronics. In most cases, all processing tasks are demanded to high-level programming of GPUs. In the Aixplorer scanner (Supersonic Imagine, Aix-en-Provence, France) [48], an acquisition clip covering an interval of some seconds may be launched from a conventional ultrasound mode. The user can then review the clip after applying beamforming and extended processing capabilities to the acquired data. In [21], an elegant approach based on C++ and Cuda programming allowed to equip a software-based platform with a live color-encoded speckle imaging (CESI) modality [29]. The same channel data acquired during real-time were retransmitted to the GPU to visualize, off-line, turbulent flow with CESI running at high-frame-rate.

Although the goals that boosted the development of VRT modality on the hardware-based ULA-OP 256 are similar to those that guided the previous approaches, the implementation is totally different. The architecture of the FE FPGAs was here modified to make possible reloading the raw data present in the DDR RAM. The data are then processed by the same ULA-OP 256 hardware chain for both RT and VRT modalities. This allows uniformity in the user interface and no delay between the two phases.

In the proposed architecture, HFR acquisitions can be immediately reproduced in slow motion replay mode. When processing is limited to the production of B-Mode images, as in the HFR plane wave imaging example, it would be possible to further increase the acquisition PRF by reducing the RT frame rate (e,g, by producing only the frames that can be seen on the screen).

In general, the RX parameters can be tuned to maximize the display quality, and it is also possible using different sets of elaboration parameters, e.g. a “light” set in RT and a “full” set in VRT, capable of optimizing the algorithm performance.

Such capability was used in two applications: for high PRF multiline vector Doppler and high frame rate color Doppler imaging.

In MLVD, VRT modality was used to extend the range of PRF values that can be set in MLVD mode, making possible the investigation of the high flow-jets typical in stenotic vessels. In this application a “light” parameter set was optimized to reduce the calculation effort in real-time, so that a PRF of about 16 kHz was achieved. On the other hand, the “full” set, used in VRT, was designed to achieve a high-quality visualization of the flow details.

In color Doppler imaging, VRT modality was used to overcome the limitations in terms of spatial resolution size of the region of interest that real-time processing imposes because of the processing effort of CFM images at high frame-rate based on plane wave transmission with coherent compounding.

The fast switching from RT to VRT and vice versa lets finding the most favorable combination of all processing parameters and enables slow motion investigation of rapidly evolving flow events that might be skipped in RT.

It is worth highlighting that lowering the VPRF does not lead any reduction in aliasing limit, since the aliasing limit is uniquely related to the acquisition rate, PRF**.** VRT data are processed with the same hardware used in the original methods, i.e., the same mathematical noise due to, e.g. fixed point arithmetic, operation sequence, etc., so, VRT modality can be applied to any ultrasound method implemented and previously validated on the same research platform. No new software needs to be developed nor a new validation is required when a method is run in VRT mode.

# Chapter 5. Multi-plane advanced modes

*This chapter reports on advanced ultrasound modalities based on multi-plane imaging. The mode was enabled on the ULA-OP 256 by developing and upgrading the system with 3-D imaging capabilities by 2-D probes.*

*The activity reported in this chapter resulted in the following publications:*

***Claudio Giangrossi**, Alessandro Ramalli, Carlo Palombo, and Piero Tortoli, " Bi-plane imaging for a robust assessment of Flow Mediated Dilation," 2021 IEEE International Ultrasonics Symposium (IUS), 2021, pp. 1-4, doi: 10.1109/IUS52206.2021.9593360.*

*Alessandro Ramalli, Enrico Boni, **Claudio Giangrossi**, Paolo Mattesini, Alessandro Dallai, Herve Liebgott, Piero Tortoli, "Real-Time 3-D Spectral Doppler Analysis with a Sparse Spiral Array," in IEEE Transactions on Ultrasonics, Ferroelectrics, and Frequency Control, vol. 68, no. 5, pp. 1742-1751, May 2021, doi: 10.1109/TUFFC.2021.3051628*

## 5.1 Introduction

3-D imaging on ultrasound scanners is a big challenge due to the high complexity of the system, the management of huge data rates, and the high processing load. Formerly, 3-D imaging was performed by tilting or translating linear array probes by means of a step motor to mechanically scan the volume of interest. However, 3-D imaging was correspondingly limited in terms of volume rate, incompatible with several applications. The great technology progress has enabled the production of 2-D array probes, which are composed by a bidimensional matrix of transducers which permits the electronic scan of volumes [49]. The main downside is that the management of hundreds (in some cases even thousands) of transducers of a 2-D probe involves the management of huge amount of data [50]. The objective of this research was to contribute to the development of an advanced and programmable 3-D imaging system, based on the ULA OP 256 scanner, capable of introducing novel 3-D imaging modalities.

In particular, the software of the ULA-OP 256 was upgraded to allow the scanner to be coupled with 2-D probes of arbitrary geometries, including matrix and sparse arrays[5]–[7]. Furthermore, the scanning methods were upgraded to allow the selection of scan planes with programmable rotational angles in a volume.

These new functionalities, in combination with a sparse spiral array probe, were exploited in two novel applications: real-time 3-D spectral Doppler analysis and robust assessment of flow-mediated dilation.

## 5.2 Upgrade of the ULA-OP 256 software for 3-D imaging

The original software of the ULA-OP 256 allowed managing only 1-D array probes. Through a configuration text file, the element-to-channel mapping of the probe was described together with other specific parameters such as the pitch and the center frequency. Moreover, the scan sequence was defined through another configuration text file, which only considered a 2-D coordinate system.

The available parameters in the two configuration files were sufficient to the software to compute the position of fully populated linear, convex, and phased arrays and to calculate the TX/RX apodization and delays for 2-D scan sequences. Nevertheless, this type of notation was not effective to enable the use of 2-D probes and 3-D imaging. First, the position of the elements and the scan directions need to be defined in a 3-D coordinate system; moreover, the probe configuration file should consider the possibility of using sparse arrays. Therefore, the probe configuration file was modified to let the user define the position of each element of the 2-D probe in a 3-D coordinate system, thus enabling the definition of not fully populated matrixes and, more in general, any arbitrary array geometry including non-gridded sparse arrays (i.e., sparse arrays whose elements are not forced to be positioned on a grid).

Moreover, the configuration file defining the scan sequences was also modified to include: 1) the third spatial coordinate of the Cartesian system in the definition of the position of focal points and beamforming directions in a volume; 2) the rotational angle, to allow defining and scanning planes at a rotation angle different from 0°, i.e., the imaging plane used in 2-D imaging.

The most critical part of this activity was to upgrade the ULA-OP 256 software to interpret the new parameters without interfering with the existing scanning modalities and probes and ensure backward compatibility. For this reason, all software functions were carefully revised and upgraded to include the third spatial coordinate in the computation of delays, apodization factors, and scan sequence directions.

Specifically, all functions dealing with the TX/RX beamforming had to be updated to consider the coordinate system shown in Fig. 5-1, in which $P = (x_p, y_p, z_p)$, $O = (x_o, y_o, z_o)$, $E = (x_e, y_e, z_e)$ are the focal point of the volume of interest, the origin of the emission (also called virtual source, or apex), and the position of an element of the probe. For example, the propagation time $t_p$, used for RX beamforming, considers the time needed by the ultrasound pressure to reach $P$ from $O$ and the time needed by an element in $E$ to receive back the echo scattered from $P$. It can be computed as follows:

$$t_p(O, P, E\ ) = \frac{\left|\overrightarrow{OP}\right| + \left|\overrightarrow{PE}\right|}{c} \qquad 5.1$$

where the distances $\left|\overrightarrow{OP}\right|$ and $\left|\overrightarrow{PE}\right|$ are:

$$\left|\overrightarrow{OP}\right| = \sqrt{(x_o - x_p)^2 + (y_o - y_p)^2 + (z_0 - z_p)^2} \qquad 5.2$$

$$\left|\overrightarrow{PE}\right| = \sqrt{(x_p - x_e)^2 + (y_p - y_e)^2 + (z_p - z_e)^2} \qquad 5.3$$

The modalities implemented for 3-D imaging are all based on focused transmissions and line-by-line scan sequences, which means that for every transmission event only one line is beamformed. Moreover, since the

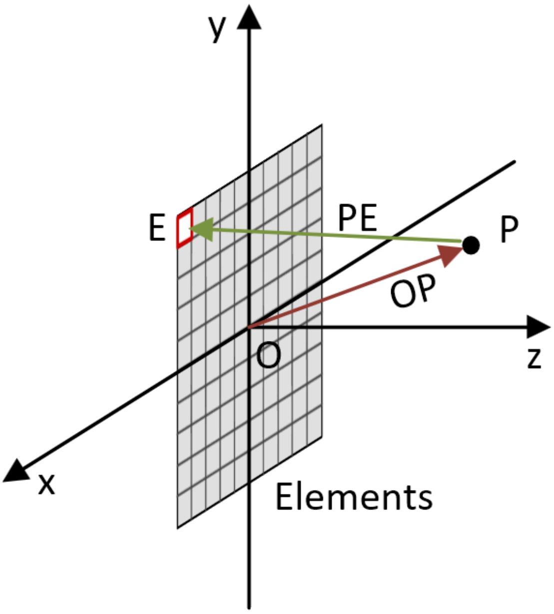

*Fig. 5-1 Illustration of TX (red) RX (green) path that must be considered to calculate the delays for each element E and for each point P of the image.*

aperture size of most available 2-D arrays is relatively small (roughly 1 cm), only phased imaging modes were implemented to scan regions of interest wide enough for general purpose tissue imaging. To further increase the region of interest, 3-D scan sequences were implemented with virtual apex on negative z values, i.e., behind the transducers plane.

As shown in Fig. 5-2, a sector scan is defined by the rotational angle ($\varphi$**)** the direction of the first line ($\theta_1$*)*, the line angular-step ($\theta$) and the number (*N*) of scan lines. The scan sequence starts from the outermost line, as defined by $\theta_1$, which belongs to the plane having the set rotational angle. The scan sequence continues with the subsequent lines, which still belong to the same rotational plane, but are oriented along directions having gradually increasing angles.

The ULA-OP 256 software upgrade now allows the implementation of the so-called multi-plane imaging, i.e., the possibility of simultaneously reconstructing multiple images over arbitrarily oriented planes and

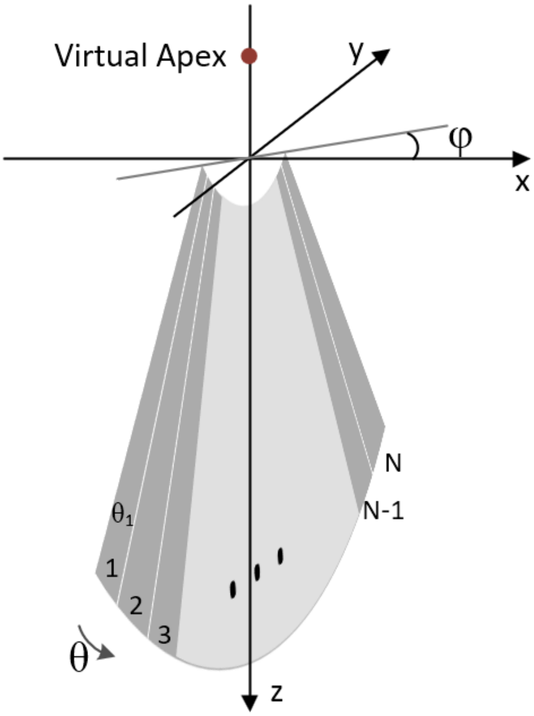

*Fig. 5-2 Illustration of TX RX sequence of a sector scan of N lines. The image is reconstructed line-by-line in N TX/RX events.*

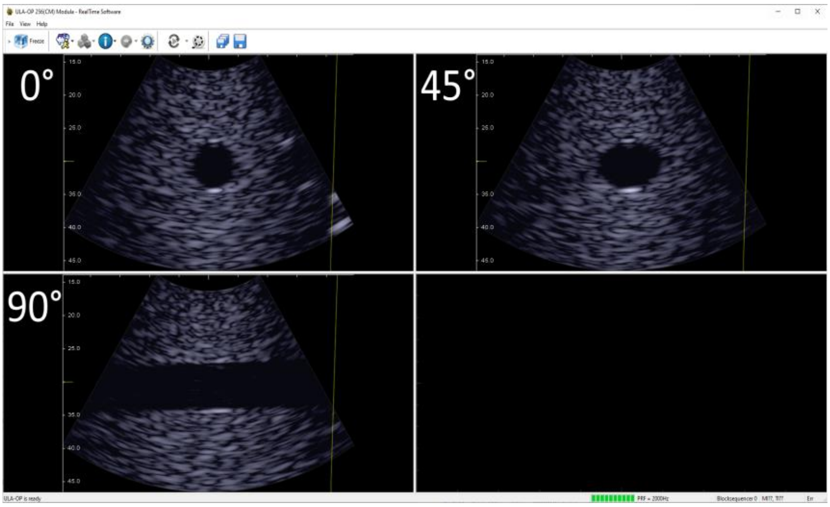

*Fig. 5-3 Screenshots from the ULA-OP 256 display obtained investigating a phantom with B-Mode phasing scan at 0°(top-left), 45° (top-right) and 90° (bottom-left) azimuth angles planes*

showing the related images in a single window. As an example, Fig. 5-3 presents the ULA-OP 256 real-time interface while showing B-Mode phantom images reconstructed at 0°, 90° and 45° rotational angles.

It is worth highlighting that the upgraded configuration files also allow defining Doppler investigation lines, which can now be steered over the entire volume of interest. Therefore, advanced imaging modalities can now be developed by interleaving B-mode imaging, over multiple planes, and Doppler imaging over different programmable lines. Examples of advanced applications will be detailed in paragraph 5.4  and 5.5 .

## 5.3 The sparse array probe

In the multi-plane applications presented in this chapter, the ULA-OP 256 research system [22] was coupled to a special version (Fig. 5-4) of the Vermon matrix array probe (Vermon S.A., Tours, France). As shown in Fig. 5-4, such a 2-D probe was obtained by sparsely selecting 256 elements out of the original array. It The latter one consists of 32 (x-axis) by 32 (y-axis) elements (3.7 MHz, 300 μm pitch, 70% bandwidth), divided into

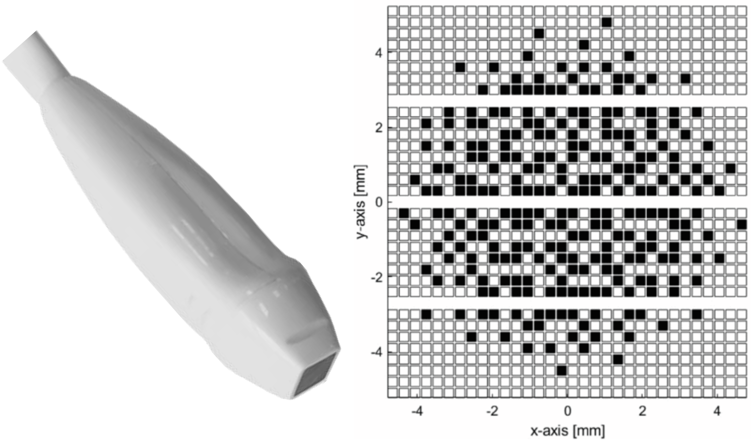

*Fig. 5-4 Picture of the special version of the Vermon sparse array probe (left), and its Layout (right). Each selected element (black) was paired to one channel of the ULA-OP 256 scanner.*

4 groups of 32x8 elements separated by an unconnected row along the y-direction. The total number of addressable elements is thus 1024.

Although not easily recognizable, the 256 selection selected element have a geometry that matches, as much as possible, the layout of a 2-D spiral whose density is tapered with a Tukey window [51], [52]. Each element could thus be paired to one channel of the ULA-OP 256 scanner so that it could be individually controlled both in TX and in RX.

The sparse array was first characterized by acquiring the one-way fields obtained in focused transmission mode. The ULA-OP 256 was programmed to transmit 3-cycle sinusoidal bursts at 3.7 MHz weighted by a Hamming’s window. Pressure signals were detected by the HGL008 hydrophone (Onda Corporation, Sunnyvale, CA, USA), which was moved in a water tank by a 6-axis positioning system to scan 2-D planes with programmable rotational angles, including that parallel to the probe surface placed at the focal distance. One-way fields were acquired for multiple configurations steering angles (0°,8°,16°), and focal depths (25 mm, 40mm) to characterize the behavior of the probe in some of the most used transmission configurations. The transmitted beam resulted correctly steered and focused. Always, the main -6dB beam width was narrower than 2.2 and 4 mm, while the peak pressures varied in the range

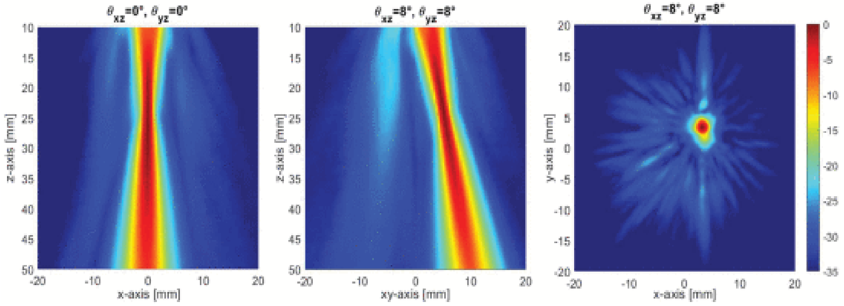

*Fig. 5-5 Examples of experimental one-way fields produced by the 256-element sparse array. In the left panel, the beam was not steered and was acquired on the plane with rotational angle equal to 0°, i.e., the xz-plane. In the middle and right panels, the beam was steered by 8° on both lateral directions and was acquired on the plane with 45° rotational angle (center) and on a plane parallel to the probe surface at a depth of 25 mm (right).*

[140, 260] kPa and [90-200] kPa for beams focused at 20 and 40 mm, respectively. Moreover, secondary lobes were at least 20 dB lower than the main lob peak in all steering conditions. Fig. 5-5 shows three beamplot examples.

The relatively good transmission performance of the sparse array pushed the development of two advanced modalities based on bi-plane imaging for a robust assessment of flow mediated dilation and for 3-D spectral Doppler analysis.

## 5.4 Application to bi-plane imaging for a robust assessment of Flow Mediated Dilation

The Flow Mediated Dilation (FMD) is a biomarker of endothelial function that can permit an early diagnosis of atherosclerosis, predict cardiovascular diseases, and perform follow-up on therapy effectiveness [53]–[58]. The FMD response is reduced in the case of endothelial diseases and is restored when the therapy works. The exam consists in monitoring the response of the brachial artery to reactive hyperemia induced by a temporary arterial occlusion [59]. The vessel response is comprehensively assessed by continuously monitoring both the Wall shear rate (WSR) and the arterial diameter [60]. Typically, both parameters are evaluated through the long-axis view of the artery [61]–[64]. The WSR is often estimated by the centerline Doppler velocity measurement assuming an ideal parabolic flow velocity profile, and the wall distension is assessed by measuring the diameter changes produced by the release of the occlusion cuff. The exam is relatively long (10-15 minutes), and unavoidable probe-to-arm movements often impair the success of the exam even if special supports are used to hold still the probe and the patient's arm. In particular, the diameter measurement on the longitudinal view is reliable only when the imaging plane exactly intercepts the full vessel diameter. In case of misalignment, the estimation is non-consistent. For this reason, FMD has not spread as a routine clinical exam but is mainly used for research protocols [65], [66].

In this application, a bi-plane imaging modality has been proposed that, by exploiting both cross and longitudinal arterial views, allows robust measurements of diameter and flow profile.

### *Bi-plane imaging for FMD*

In this application, the system was programmed to perform (bi-plane) B-mode imaging of two perpendicular planes corresponding to the artery longitudinal and cross-section, respectively, as shown in Fig. 5-6. A Doppler investigation line could also be set over the longitudinal section to detect the flow profile through multigate spectral Doppler (MSD) [67] processing, and assess the wall shear rate (WSR).

In the cross-section view, the artery is shown as a black circle-like region, which remains in the field of view even when the probe is slightly misaligned.

### *Diameter and velocity profile estimation*

The estimation of the diameter is performed in real-time with a modified version of the edge-detection algorithm proposed in [61], [68]. In this algorithm, several (typically 16) points are tracked on both near and far arterial walls; then, the diameter is estimated as the average distance between the points on the walls. In the modified algorithm, the instantaneous diameter is calculated as the diameter of the regression circle that best fits the edge-detected points. The real-time processing module

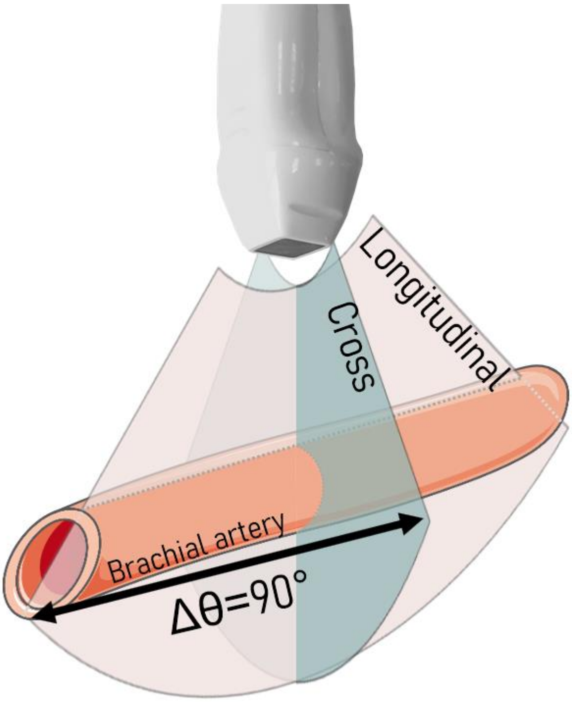

*Fig. 5-6 The spiral array probe investigating cross and longitudinal views of the brachial artery.*

elaborates 30 edge-detection points, whose initial positions lay over a circumference centered on a manually selected point. For each edge-detection point, a circular domain around the point is considered, of which the center of mass is calculated using the B-mode greyscale. The calculated centers of mass of the domains are then used to move the edge-detection points closer to the edge. The search for the edge is iteratively repeated until convergence, i.e., when in two consecutive iterations the position of the edge-detection points moves less than 30 μm. Once all points converge, the diameter is estimated as that of the best fitting circumference regressed from the edge contour. It is worth highlighting that the position of each point is angularly constrained frame by frame. On the real-time interface, the edge-detected points are positioned on the B-mode image along the wall of the artery, while the instantaneous diameter trend is plotted on an additional window.

The WSR estimation is based on both the walls' position and the velocity profile along the artery radial direction. The latter is evaluated through MSD profiles, which are produced by the DSPs by computing the complex module of a 256-point FFT for each depth. The MSD profiles are further processed by extracting the mean Doppler frequency, which is converted to flow velocity through the Doppler equation. For the latter, the Doppler angle is estimated as the angle between the Doppler investigation line and the linearized wall directions extrapolated by tracking the wall position in the longitudinal view. Finally, the shear rate is computed as the maximum velocity gradient with respect to the vessel radius in the proximity of the wall position.

### 5.4.1 Experiments and Results

Two experiments were performed with the proposed bi-plane imaging method, in which the ULA-OP 256 was programmed to sequentially interleave the transmission of one line for each of the two B-mode planes and the Doppler line. The pulse repetition frequency (PRF) was set to 8 kHz, which allows reconstructing 128-line B-mode images at 20 frames per second (FPS) and sustaining an effective PRF of approximately 2.7 kHz for the Doppler line, high enough to avoid aliasing in this application.

#### *Phantom tests for robustness estimation*

The first experiment aimed to compare the robustness of the diameter tracking algorithm, when implemented on the cross or the longitudinal view, respectively. In this test, a phantom with vessels having different diameters ($D$ = 4, 6, 8 mm) was used to assess the algorithm capability to correctly estimate the diameter in case of probe-to-vessel misalignments. The probe, held by an automatic positioning system, was initially aligned to include, in the longitudinal view, the vessel's main axis. Then, the estimation algorithms were initialized to simultaneously track the vessel diameter on both cross and longitudinal views. Finally, the probe was harmonically moved back and forth from the vessel axis up to an offset of $0.2\times D$ as shown in Fig. 5-7. The same test was repeated for each of the 3 vessels. The measurement coefficient of variation $CV = \sigma/\mu$ was

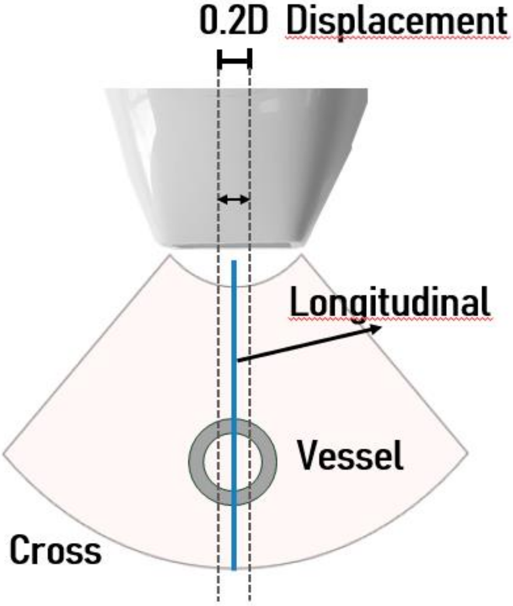

*Fig. 5-7 Cross and longitudinal planes, used for the diameter estimations, are represented in pink and blue, respectively. While estimating the diameter, the probe was harmonically moved within an offset equal to 20% of the diameter (dotted lines).*

calculated as the ratio between the standard deviation, $\sigma$, and the mean, $\mu$, of the estimated diameters during the 60 s-long acquisition.

Fig. 5-8 shows the instantaneous measurement values during each phantom test, when the diameter was estimated from both the cross (in red) and longitudinal (in blue) views. The results highlight that, besides a common underestimation, the measurements based on the cross-section view allowed better accuracies. For example, for the 4 mm vessel, whose diameter is comparable to that of the brachial artery, the underestimation was, on average, 4%, while it was 10% when the diameter was estimated from the longitudinal view.

Concerning the algorithms' robustness, the trends reported in Fig. 5-8 point out that the estimations on the cross-section are much more stable and robust to probe misalignments from the vessel axis. The resulting CVs quantitatively confirm that the variability of the estimation obtained on the cross-section view is approximately one-third of that obtained from the longitudinal view.

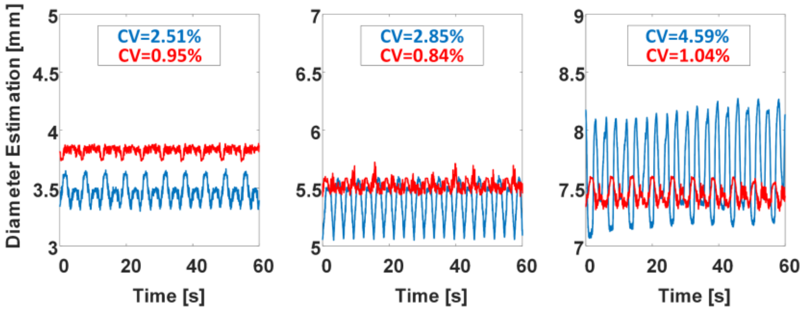

*Fig. 5-8 The graphs shows the estimations resulted by the phantom tests on the three vessels with diameters 4mm, 6mm, 8mm (left to right respectively). Estimates conducted during the 1-minute-long tests for the longitudinal and cross section views are shown in blue and red, respectively, while the related coefficients of variation are reported in the black box.*

### *In vivo experiment*

A preliminary in-vivo test was conducted on a 32-year-old healthy volunteer, i.e., with no cardiovascular pathology reported in the medical history. After few minutes resting, to stabilize the heart rate, the real-time interface of the ULA-OP 256 (Fig. 5-9) was started and the probe was placed to simultaneously scan the cross (panel A) and longitudinal (panel B) sections of the volunteer’s brachial artery.

Once the probe position was stabilized, the diameter tracking algorithm was started on both the scan sections by manually selecting a point inside the vessel (blue crosses). Once the positions of the edge-detected points (yellow dots) were superimposed to the B-mode images, the instantaneous values of the diameter, estimated in real-time, were visible in panels C and D. The panel E shows the MSD profile used for flow velocity and WSR estimations and computed along the Doppler line shown in yellow on the longitudinal section. As qualitatively showed in the trend graphs of the instantaneous diameter, the one estimated on the cross-section is less noisy than the one estimated on the longitudinal section, and its trend matches a physiological pattern during the cardiac cycle, with clear systolic vessel dilations and diastolic contractions.

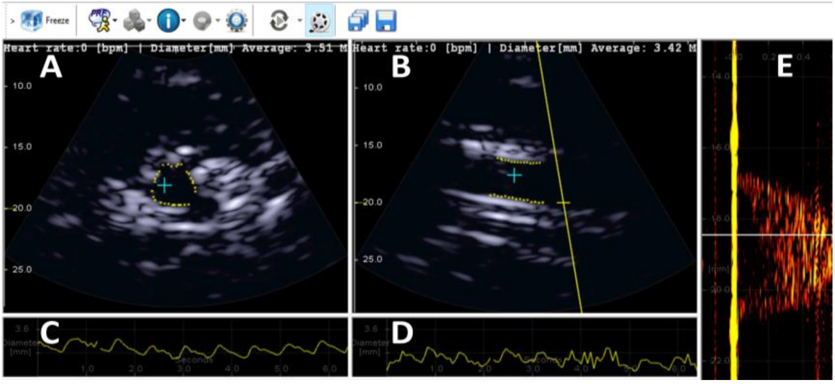

*Fig. 5-9 Screenshot of the ULA-OP 256 user interface during a bi-plane FMD investigation of the brachial artery. The blue crosses in A, B show the initial point set by the operator inside the vessel to start the estimation, Dotted lines in A, B indicate the tracked positions of the vessel walls used for calculation of diameters as shown in panels C and D, respectively. Panel E shows an instantaneous spectral profile detected along the yellow line in B and used for wall shear stress estimates.*

The two experiments proposed showed that both in phantom and in-vivo tests the proposed by-plane imaging technique resulted robust to probe misalignments. Phantom tests, performed on vessels having different diameters, demonstrated that the cross-section is more suitable to track the diameter on long acquisitions and allowed reducing both the underestimation and the CV with respect to the estimation on the longitudinal. The in-vivo test qualitatively confirmed the same findings and confirmed that the proposed approach is a robust solution for feasible FMD exams and encourages next clinical tests.

## 5.5 Application to real-time 3-D Spectral Doppler Analysis with a Sparse Spiral Array

Over the last four decades, ultrasound spectral Doppler has been the method preferred by medical doctors to quantitatively assess blood flow velocities [24], [31], [69]–[72]. Although traditionally limited to the detection of velocities within a single sample volume, spectral analysis has also been successfully extended to multiple sample volumes aligned along a scan line (Multigate spectral Doppler – MSD), for either peripheral vascular or aortic investigations [23].

In recent years, massive research efforts and technological developments have brought two major breakthroughs: volumetric (3-D) imaging [14], [73]–[75] and vector Doppler [11], [28], [76], [77], [77]–[84]. Although full acceptance of new display modalities always takes some time, both methodologies look mature for implementation in ultrasound machines. Furthermore, medical doctors working on peripheral vascular have frequently complained that the morphology of plaques is 3-D and, hence, unfair assumptions must be done when working with pulsed-wave (PW) Doppler by using 2-D scanners. The possible extension of spectral-analysis-based velocity investigation to all points within an entire volume is, thus, of undoubtful clinical interest. The support of a 3-D morphological view may facilitate the optimal probe positioning and the rapid identification of regions in which spectral analysis may provide valuable flow information.

In this application, ULA-OP 256 combined with the 256-element, 2-D spiral array can provide, in real time, multigate spectral Doppler profiles along lines that can be arbitrarily located in a volume. The implementation of coded transmission (TX) together with matched filtering in reception (RX), is also described, and shown capable of partially overcoming the SNR limitation of sparse arrays.

The scanner was programmed to permit the navigation in the volume of interest. B-mode images, on planes defined by a programmable rotational angle, are simultaneously displayed to locate non-isoplanar Doppler lines over the vessels of interest.

### *Transmission*

For both B-Mode and Doppler imaging, the ULA-OP 256 is configured to transmit focused beams with programmable focal depth. No apodization is applied in TX on the 256 excitation signals since the spiral layout implemented density tapering. For each Doppler line, either tone bursts or linear frequency modulated (chirp) signals are used in TX to drive each active element with the same 35 V peak amplitude (see Fig. 5-10). The chirp is 5 μs long, linearly spans a band of 3 MHz centered at 3.7 MHz, and is tapered with a 10% Tukey window. In this way, the resulting -6dB

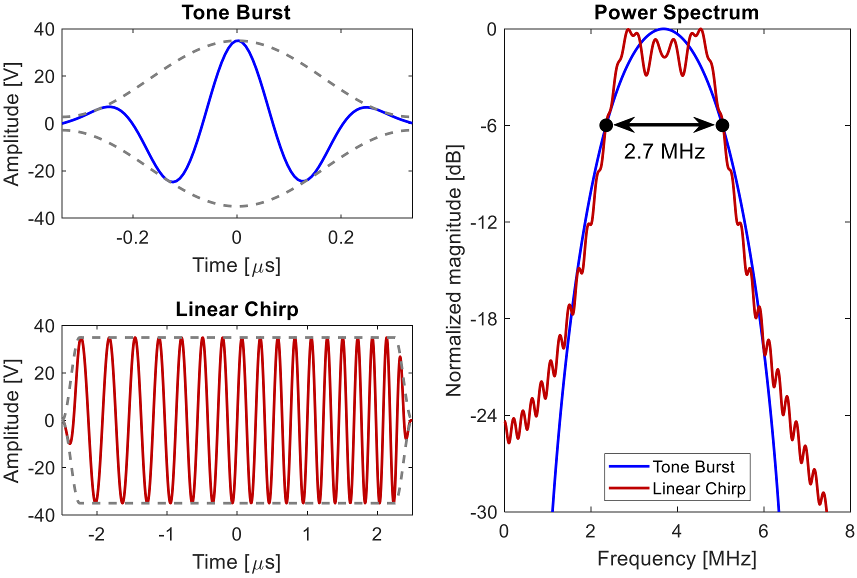

*Fig. 5-10 The excitation signals (left panels) and their power spectra (right panel). On the left panels, the dashed gray lines represent the envelope of the tapering windows.*

signal bandwidth (2.7 MHz) matches the probe bandwidth. The length of the chirp was chosen by considering a tradeoff among SNR gain, depth of the blind zone, and imaging artifacts [85]–[87]. The tone burst, which is also used for B-mode imaging, includes 2.5 cycles of a sinusoid at 3.7 MHz. The burst is weighted by a Hamming window to obtain the same (-6dB) bandwidth and maximum amplitude of the linear chirp. The B-mode images are obtained by scanning 128 consecutive lines on 64°-wide sectors.

### *Reception*

In RX, the echo signals received after each TX event are band-pass filtered (cut-off frequencies: 0.25 and 10.0 MHz), time gain compensated, and analog-to-digital converted at 78 MHz with 12-bit resolution. Then, they are dynamically beamformed with constant f-number (F# = 2) by the FPGAs onboard ULA-OP 256. Finally, the beamformed signals are quadrature demodulated and downsampled by the available DSPs to produce up to 512 output samples. The downsampling factor can be adjusted by the user to cover the range of interest.

### *Matched filtering*

The ULA-OP DSPs are also in charge of applying matched filtering to the echo-data obtained in Doppler mode. To reduce the computational load, matched filtering is performed on baseband data and in the frequency domain rather than in the time domain [88]. Baseband operation is not expected to produce any distortion since the chirp duration is limited to 5 μs and the active aperture is relatively small [89], [90]. For each TX/RX event, pulse compression is thus achieved in 3 steps:

1) Up to 512 (fast-time) beamformed, quadrature demodulated, and downsampled data are transformed, after zero-padding, to the frequency domain through a 1024-point Fast Fourier Transform (FFT).
2) The resulting complex spectra are multiplied by the coefficients of the matched filter. The frequency response of this filter reproduces the complex conjugate spectrum of the TX signal. If needed, the amplitude response can be weighted by a window that partially mismatches the filter while reducing the side-lobes [85], [86], [89].
3) Spectral data are transformed back to the time domain through a 1024-point inverse-FFT and the 512 valid output samples are made available for the next processing stages.

It is worth noting that, for a fair comparison, matched filtering was applied to the data of both the tone burst and the linear chirp.

### *B-mode and Doppler processing*

For B-mode imaging, the moduli of baseband complex data are computed and log-compressed before being transferred to the host PC. The data are finally scan-converted and displayed in grayscale by the PC real-time interface.

For MSD-mode, the slow-time, baseband (and, possibly, pulse compressed) samples corresponding to each of 512 different depths along the Doppler line, are FFT-processed by the DSP. The complex moduli of the spectra are then transferred to the host PC. Here they are displayed as color-scale images in which the horizontal axis corresponds to the Doppler frequencies and the vertical axis to the depth of the examined sample volume [23].

The user can also select one of the MSD depths to simultaneously show the corresponding spectrogram as a color-scale image in which the horizontal axis corresponds to time and the vertical axis to the Doppler frequencies.

### 5.5.1 Experimental tests

#### *Assessment of SNR gain*

In order to prove the effectiveness of real-time pulse compression in 3-D Doppler mode, experiments were conducted on a homemade flow phantom. This consisted of a straight, rigid, cylindrical tube immersed in a water tank and connected to a hydraulic circuit, through which a blood-mimicking fluid was pushed by a programmable peristaltic pump (Watson-Marlow, Falmouth, UK). Specifically:

- The 70-cm long tube, having an inner diameter of 8 mm and 1-mm thick wall, was made of Rilsan® (Arkema S.A., Colombes, France) - a polyamide and bioplastic member of the nylon family of polymers - characterized by an attenuation coefficient of 2dB/cm/MHz and sound propagation speed of 2600 m/s.
- The blood-mimicking fluid consisted of 2.5 g of 10-µm particles of Orgasol® (Arkema S.A., Colombes, France) - a polyamide powder - suspended in 2 liters of demineralized water with 1 g of surface-active agent for a uniform distribution of particles [39].
- The fluid flowed, at a steady rate of 280 ml/min, from a reservoir into an expansion tank, then through the straight tube, and finally back to the reservoir. Acquisitions were repeated for 9 different directions of the Doppler line, corresponding to the combinations of the angles 0°, 8°, and 16° in both xz- and yz-plane.

During these tests, as sketched in Fig. 5-11, manual setting of the probe position was facilitated by two real-time B-mode images: the first one, reconstructed along the plane with 90° rotational angle, was used to intercept the cross-section of the tube; the second one, whose rotational

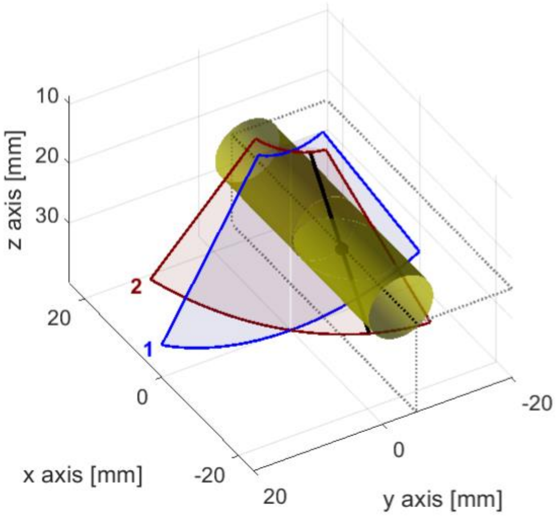

*Fig. 5-11 The reference system and the scanning planes used to facilitate the alignment of the probe with the straight tube. The probe was centered on the origin of the reference system. The first plane, with 90° rotational angle (blue), was used to intercept the cross-section of the tube (yellow). The second plane (red), was used to ensure a proper alignment between the tube axis and the focusing point (black dot) of the (solid black) Doppler line, in this example steered at $\theta_{xz}= \theta_{yz}=16°$. Gray dotted lines represent the projection lines of the tube axis along the main planes.*

angle was programmed to include the Doppler investigation line, was used to ensure a proper alignment between the tube axis and the focal depth of the Doppler line.

To allow comparing the Doppler SNRs achieved by using different TX signals, the ULA-OP 256 was programmed to interleave, at 1 kHz PRF, the following TX events:

*1)* Sinusoidal burst TX along a scan line of the B-mode image 1.
*2)* Linear chirp TX along the Doppler line.
*3)* Sinusoidal burst TX along a scan line of the B-mode image 2.
*4)* Sinusoidal burst TX along the Doppler line.

Slow-time Doppler signals were acquired for an interval of 6 s. Data were here post-processed by a Matlab® (The MathWorks, Natick, MA) script that replicates the real-time MSD processing implemented on the

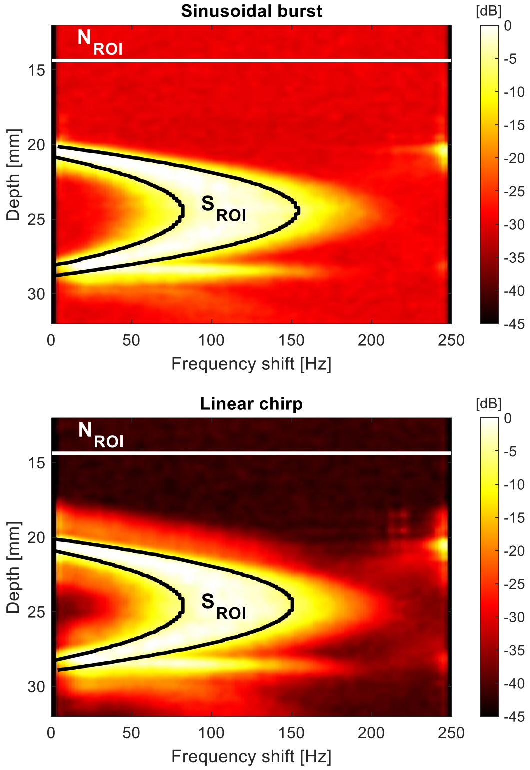

*Fig. 5-12 Examples of averaged MSD images used to determine the region of the Doppler spectrum related to the flow ($S_{ROI}$) and that containing only noise ($N_{ROI}$). The examples refer to the case with $\theta_{xz} = \theta_{yz} = 16°$. On top, the MSD image obtained with the sinusoidal burst; on bottom, the one obtained with the linear chirp.*

ULA-OP 256. The Doppler SNRs obtained with each of the two TX signals were computed as proposed in [87]. Briefly, consecutive MSD frames were averaged so that smooth images, like those in Fig. 5-12, were obtained. Here, the region of the Doppler spectrum related to the flow ($S_{ROI}$), i.e., the region within the −6dB isolines, which includes $n_S$ spectra, was semi-automatically segmented. Once the position of the walls was manually pointed, an automatic algorithm fitted the borders of the −6dB isolines with a second-degree polynomial curve. The noise region ($N_{ROI}$) was selected in the upper portion of the image, covering $n_N$ =50 depths, where the flow was absent. The SNR was thus estimated as:

$$SNR = 10\log_{10}\left(\frac{S}{N}\cdot\frac{n_N}{n_S}\right) \qquad 5.1$$

where $S$ and $N$ correspond to the total power measured in $S_{ROI}$ and $N_{ROI}$, respectively.

Finally, for each acquisition, the gain in SNR (*GSNR*) was computed as the difference between the SNR obtained with the chirp TX and the sinusoidal burst TX.

### *MSD investigation along non-isoplanar lines*

In order to prove the capability of assessing blood flow along lines located in different planes, the anthropomorphic phantom [38] of the carotid bifurcation (already described in chapter 4.4) was used. Specifically, it mimicked the bifurcation of the carotid artery with stenosis of the internal carotid artery (ICA). The phantom was substituted to the straight tube in the hydraulic circuit so that the carotid bifurcation lied parallel to the probe surface.

As sketched in Fig. 5-13, during these tests, two real-time B-mode images, crossing at the level of the common carotid artery (CCA), were

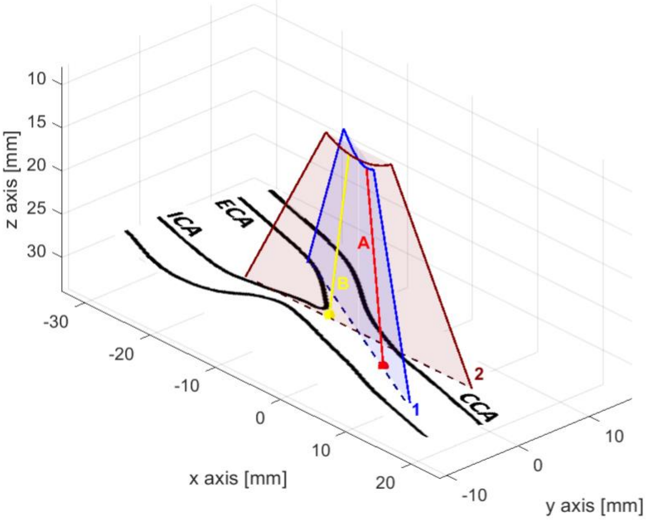

*Fig. 5-13 Schematic view of the carotid bifurcation phantom, placed parallel to the probe surface at roughly 30-mm depth. B-Mode images were obtained along planes 1 and 2. Doppler lines were steered along direction A and B.*

shown: the first, coincident with the plane at 25° rotational angle, reproduced a longitudinal section including the origin of the external carotid artery (ECA); the second one, coincident with the plane with 0° rotational angle, reproduced a section including the ICA origin.

Two Doppler lines, both focused at ~30 mm depth, were set on the two imaging planes: line A intercepted the CCA, while line B was close to the origin of the ICA. The steering angles, on the xz- and yz-plane, were ($\theta_{xz} = -14.5°$, $\theta_{yz} = -6.9°$) and ($\theta_{xz} = -8.6°$, $\theta_{yz} = 0.0°$) for lines A and B, respectively.

The ULA-OP 256 was here programmed to interleave, at 1 kHz PRF, the following TX events:

1) Sinusoidal burst TX along a scan line of the B-mode image 1.
2) Linear chirp TX along the Doppler line A.
3) Sinusoidal burst TX along a scan line of the B-mode image 2.
4) Linear chirp TX along the Doppler line B.

B-mode images and MSD spectra were directly shown in real-time on the ULA-OP 256 software interface.

### *In vivo experiments*

Two real-time B-mode images, which scan planes at different rotational angles, were made available to facilitate the probe positioning and to allow setting the position of two Doppler lines during *in vivo* tests.

The ULA-OP 256 was thus programmed to interleave, at 3 kHz PRF, 6 TX events:

1) Sinusoidal burst TX along a scan line of the B-mode image 1.
2) Linear chirp TX along the Doppler line A.
3) Linear chirp TX along the Doppler line B.
4) Sinusoidal burst TX along a scan line of the B-mode image 2.
5) Linear chirp TX along the Doppler line A.
6) Linear chirp TX along the Doppler line B.

B-mode images, MSD profiles, and spectrograms from a selected depth were shown in real-time on the ULA-OP 256 software interface.

In this interleaved mode, the mechanical index (MI), the thermal index for soft tissues at surface ($TIS_{as}$), and the temperature rise at the probe surface (ΔT) were estimated. The MI was 0.12 and 0.10 for chirp and sinusoidal burst, respectively, the $TIS_{as}$ was always lower than 0.01, while ΔT after 30-minute continuous operation in still air was 4°C. Then, preliminary acquisitions were performed on the carotid arteries of healthy volunteers.

### 5.5.2 Results

#### *Assessment of SNR gain*

Fig. 5-12 shows two MSD images obtained by transmitting the sinusoidal burst and the linear chirp, respectively. The Doppler line was set at $\theta_{xz} = \theta_{yz} = 16°$. Qualitatively, the images do not show a significant difference in the spectrum shape. Both spectra also show the same artifact due to the saturation of beamformed signals from the second wall of the plastic tube. However, an improved SNR is clearly achieved with pulse compression. Indeed, since both images were normalized to the respective overall maximum intensity, the noise level obtained with the chirp appears considerably lower than that of the sinusoidal burst. Similar results were obtained for all tested steering conditions and the estimated SNRs and GSNRs are summarized in Table 5.I. On average (see the rightmost column), the estimated SNRs were 19.6 dB for the sinusoidal burst and 31.0 dB for the linear chirp, which corresponded to an average GSNR of 11.4 dB.

TABLE 5.I

ESTIMATED SNR AND GSNR

| | **$\theta_{xz}$** | **0°** | | | **8°** | | | **16°** | | | **Avg±Std values** |
|---|---|---|---|---|---|---|---|---|---|---|---|
| | **$\theta_{yz}$** | **0°** | **8°** | **16°** | **0°** | **8°** | **16°** | **0°** | **8°** | **16°** | |
| **SNR [dB]** | **Sinusoidal burst** | 19.5 | 20.0 | 18.8 | 21.9 | 20.9 | 19.2 | 19.9 | 18.8 | 17.2 | 19.6±1.3 |
| | **Linear chirp** | 30.4 | 31.6 | 29.9 | 33.2 | 32.3 | 30.4 | 31.1 | 31.6 | 28.6 | 31.0±1.4 |
| **GSNR [dB]** | | 10.9 | 11.6 | 11.1 | 11.3 | 11.4 | 11.2 | 11.2 | 12.8 | 11.4 | 11.4±0.6 |

### MSD investigation along non-isoplanar lines

Fig. 5-14 reports a screenshot of the ULA-OP 256 interface obtained during experiments conducted on the carotid artery bifurcation phantom. The sector sketched in Fig. 5-13 is here shown as B-Mode image in Panel 1. It reproduces a region from the origin of the ECA (on the left) to the bulb in the CCA (on the right). Correspondingly, a slight increase of the vessel diameter can be observed. The (red) Doppler line here intercepted the beginning of the CCA bulb, producing MSD profiles like the one in panel A, showing a parabolic-like shape in the direction of positive Doppler shifts.

The B-mode sector shown in Panel 2 reproduces the phantom from the origin of the ICA (on the center-left) to the external wall of the CCA (on the center-right). The (yellow) Doppler line was steered on the origin of the ICA just before the stenosis. The MSD profile (panel B) is parabolic-like also here but, compared to the one in panel A, it looks “full” since the Doppler angle was close to 90° [91] and the spectral broadening was thus high. It is worth highlighting that, in this interleaved setting, a

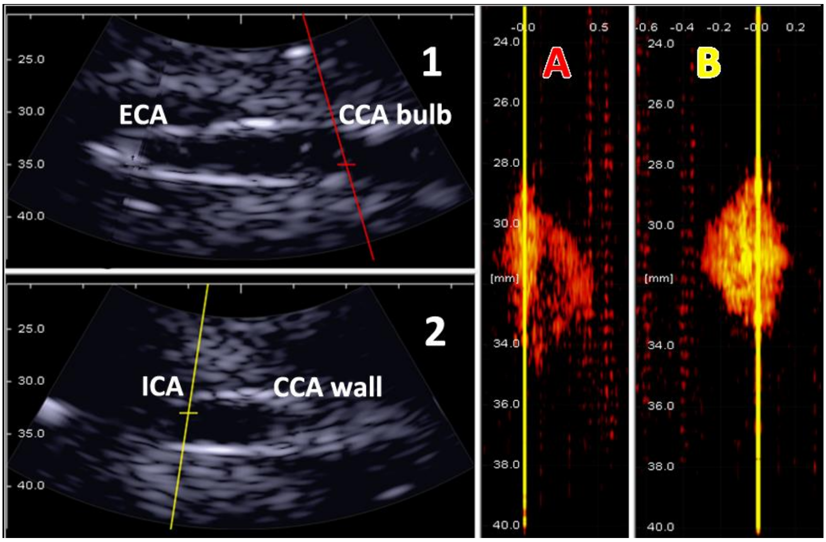

*Fig. 5-14 Screenshot of the ULA-OP 256 interface during real-time operation. B-Mode images (1, 2) and MSD profiles (A, B) were obtained as described in the schematic view of the carotid bifurcation phantom in Fig. 6. The dynamic range of B-mode images was 30dB, while that of MSD profiles was 24dB.*

PRF=1kHz corresponded to a Doppler sampling rate of 250 Hz, which was purposely adapted to get as close as possible to the aliasing limit on panel A and, hence, to exploit the whole available Doppler band.

### *In vivo experiments*

Fig. 5-15 shows two examples of the ULA-OP 256 interface frozen during real-time operation on healthy volunteers. In these examples, the bi-planar B-mode volume rate, limited by the PRF (3kHz), the number of interleaved transmission events (6), and the number of lines per frame (128), was 3.9 Hz, which is quite low but sufficient to support probe positioning. On the other hand, the update rate of MSD profiles was arbitrarily set to 40 Hz, which is high enough for real-time display, but, considering the computational power of the DSP, it could have been increased up to hundreds of Hz.

In the first example, Fig. 5-15 top, the delta between the rotational angles of the two B-mode images was set to 90°. In this way, the longitudinal and the cross-section of the CCA could be scanned. The Doppler line A was steered by 10° within plane A, while line B was set perpendicular to the probe surface.

Both MSD profiles have an M-like shape, which is typical during late systole [92]. In panel B, in particular, a strong clutter from the walls is visible and the spectra look “full”, down to 0 Hz, which is associated with the almost 90° Doppler angle. Vice versa, the profiles along the Doppler line A show a wider spectral window, as expected at a lower Doppler angle.

In the second example, Fig. 5-15 top, the delta between the rotational angles of the two B-mode images was set to 60°. To simulate a non-optimal positioning of the probe, it was slightly shifted with respect to the axis of the CCA, but both Doppler lines were roughly focused on the CCA axis. The two B-mode images show two cross-sections of the CCA, which take the form of ellipses. Both MSD profiles have a parabolic-like shape, as expected during diastole, and show a strong wall clutter. Moreover, they have opposite Doppler shifts: negative along line A and positive along line B, as expected from the schematic view sketched in Fig. 5-15 bottom. Finally, also in this case, both the MSD profiles and the sonograms are “full”, due to the almost 90° Doppler angles.

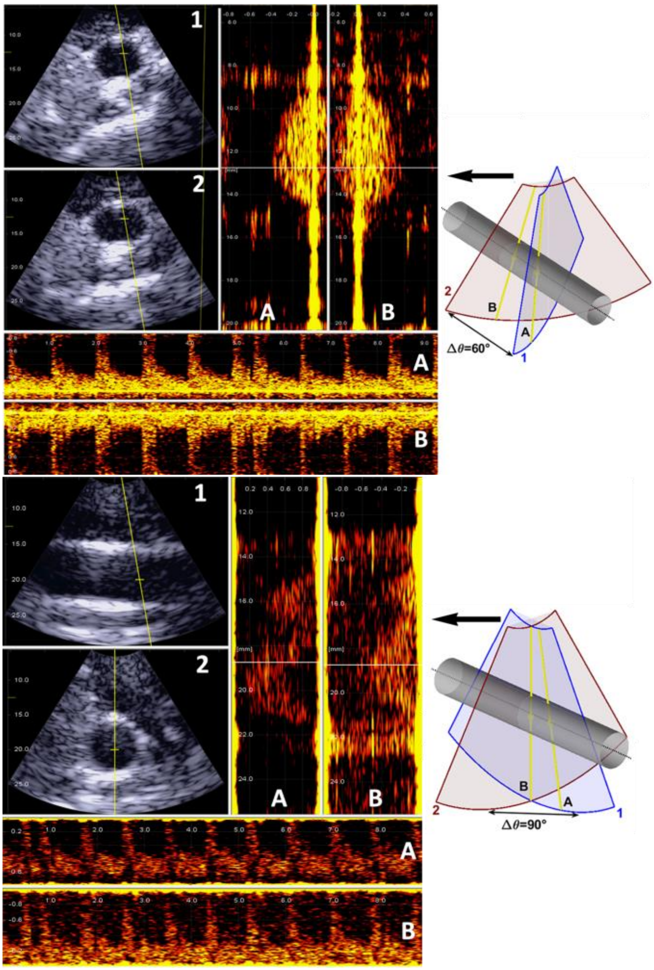

*Fig. 5-15 Two examples of the ULA-OP 256 interface during real-time in-vivo operation on the common carotid artery of healthy volunteers (left). B-Mode images (1, 2), MSD profiles and related sonograms (A, B) were obtained as described in the schematic views (right), where the common carotid artery is sketched as a gray cylinder. The dynamic range of B-mode images was 30dB, while that of MSD profiles was 24dB.*

### 5.5.3 Discussion

In this application, the first system capable of performing real-time spectral Doppler from any of the points in the volume, scanned by a 2-D spiral array has been presented. The system was based on the ULA-OP 256 research scanner and on a prototype spiral probe, designed by selecting 256 elements from a 1024–element gridded array. The MSD modality, which represents an extension of classic PW Doppler to multiple sample volumes along a line, has been implemented. The effectiveness of coded transmission and pulse compression in reception to compensate for the low achievable SNR due to the limited number of elements has been also tested.

The performance of the system was quantitatively assessed on experimental data acquired from flow phantoms based either on a straight tube and on an anthropomorphic phantom of the CCA. Finally, for a qualitative assessment of the system performance in-vivo, real-time images were also collected on a healthy volunteer.

Different interleaving sequences, depending on the application of interest, were implemented. For example, the TX sequence for B-mode imaging was interleaved with the transmission of: 1) different Doppler pulses (i.e. a sinusoidal burst and a linear chirp) along the same investigation line, for SNR assessment; 2) chirp Doppler pulses along investigation lines within different scan planes, to qualitatively assess the blood flow in the anthropomorphic phantom and in-vivo. Together with the two B-mode images, used to facilitate probe positioning, two MSD profiles with (Fig. 5-15**)** or without (Fig. 5-14) the spectrograms from selected depths were simultaneously displayed. This capability could be used to observe the flow dynamics along non-isoplanar Doppler lines, e.g. to simultaneously assess the flow before and after a stenosis, an aneurysm, or an aortic stent. This approach, compared to conventional color flow mapping, would provide quantitative evaluation of blood flow along multiple (possibly non-isoplanar) lines, with higher temporal resolution, rather than a qualitative color-map of blood flow distribution in a plane.

In [6], it was demonstrated, through off-line calculations, that the use of sparse, rather than full arrays, neither affects the shape nor the mean frequency of the Doppler spectrum, but it impairs the SNR. The results presented in this work have shown the effectiveness of pulse compression in SNR enhancement. Specifically, the use of a linear chirp [87], instead of a sinusoidal burst, has brought to an SNR increase of 11.4 dB (see Table 5.I) which was quite stable (standard deviation equal to 0.6 dB) for the tested steering conditions. Also, the average SNR increase was very close to the theoretical value ($10\log_{10}(B \cdot T)$) [89], which resulted 11.3 dB in the tested conditions (B = 2.7 MHz, T = 5µs). Such gain partially compensated for the limited SNR associated with the use of a reduced number of elements (here 256) typical of sparse arrays. Considering that any possible doubling of such number is expected to increase the SNR by 9 dB (6 in TX and 3 in RX) [6], the pulse compression gain here allowed obtaining a performance better than that achievable with 512 elements excited by standard pulses. In pulsed wave Doppler applications, the SNR could also be increased by exploiting long, narrowband pulses, with conflicting implications on transit time and velocity gradient broadening, respectively. Nevertheless, lengthening the pulses is not advisable in applications where the range resolution is important, e.g. in multi-gate spectral Doppler and color flow imaging. Pulse compression thus represents a good means to achieve high SNR while using wideband, i.e. high resolution, signals.

Even if, in general, the transmission of long linear chirp signals for extended exposure times might rise thermal effects [87], on both probe and skin surfaces, this did not happen in our tests. The relatively low excitation voltage (±35 V) and the sparse distribution of the active elements most likely facilitated heat dissipation. Therefore, the excitation voltage could be further increased, but in our case, we preferred to stay below the safety limit of ±45 V suggested by the probe manufacturer.

In this application, a sparse spiral array was associated to a 256-channel research system to detect, in real-time, the flow profiles along non-isoplanar investigation lines in phantom (Fig. 5-14) and in vivo (Fig. 5-15). The profiles, as expected, show different shapes, depending on the Doppler angle and investigated region. In vivo, in particular, although tissue attenuation further impaired the SNR, the sonograms and the profiles exhibited the expected spectral windows and the same physiological trend that can be observed with linear arrays [92]. All benefits and limitations of 2-D spectral Doppler can be extended to 3-D. For example, quantitative information on blood flow velocity could be obtained through simple angle correction or, e.g., through vector flow imaging techniques exploiting the Doppler bandwidth to estimate the flow direction [27], [93].

The results also highlight some limitations of the current system. The MSD images in panels A, B of Fig. 5-14, present secondary profiles whose depth and frequency are slightly shifted with respect to the main Doppler profile. These profiles can be attributed to the characteristics of the transmitted fields, which, in addition to the main steered beam, also show relatively high (up to -20dB) grating lobes, as visible in Fig. 5-5 at the beginning of this chapter. Furthermore:

1) The probe characteristics were not ideal for the investigation of superficial vessels: the central frequency was too low and the aperture size was too small (<1 cm) to achieve good spatial resolution.
2) The relatively wide elements and the big average pitch limit the probe steering capability, in terms of reduced sensitivity and increased grating lobe level, respectively. This, in turn, limits the effective size of the region of interest.
3) The navigation system based on two B-mode images, although capable of working at reasonably high frame rates, does not facilitate the detection of the vessels of interest, as a full 3-D rendering could do.

For clinical examinations of shallow vessels, wider apertures, linear scans, and higher frequencies would be preferable. However, the presented configuration might be suitable for the investigation of the carotid artery or the jugular vein as well as for echocardiography [51] and abdominal vascular applications. Nevertheless, to make the system suitable for clinical tests, the following features should be included:

1) Integration of in-probe pre-amplifiers to further improve the SNR and penetration depth [94].
2) A better navigation system, which could include a C-Mode display and, possibly, an automatic system to determine the rotational angles of the imaging planes, adapting them to the specific anatomy of the subject. In the latter direction several approaches based on artificial intelligence showed promising results in automated recognition [95]–[97], and should be considered.

## 5.6 Conclusion

In conclusion, by taking into considerations the proposed applications, the results are really encouraging and confirm that sparse arrays are a feasible option for the implementation of 3-D imaging/Doppler systems.

The two proposed applications showed that at a relatively cheap cost, they may give to physicians the opportunity to:

- Simultaneously assess a robust measurement of diameter and WSR for FMD exam using a bi-plane imaging
- Simultaneously assess the dynamics of blood flow within an entire volume of interest, at high temporal resolution, and on multiple non isoplanar directions simultaneously.

Moreover, the 3-D morphological view will provide more degrees of freedom and less room for errors in probe positioning.

# Chapter 6. Requirements and Limitations of HFR 3-D imaging systems

*This chapter report a study regarding the basic requirements in terms of computational, memory and data transfer rates, of 3-D imaging at high frame rates. A case study is also presented; it highlights the bottlenecks of a research scanner and proposes an alternative architecture to improve the performance of the system.*

## 6.1 Introduction

An ultrasound system is a complex interconnection of sub-systems that carry out different functionalities: the probe [2], [5], [7], [98], which transmits ultrasound waves [99], [100] and receives the backscattered echoes; the transmission stage (TX), which drives the probe with appropriate signals; the acquisition chain (RX), which includes signal conditioning, digitization, and data storage into memories; the processing stages, including dynamic beamforming [17], [101] and all the digital signal processing required by the specific imaging modes [28], [29], [33], [47]. In most scanners [15], [16], [19], [21], each function is implemented by specific devices, often embedded on different electronics boards, interfaced with each other according to the general architecture of the system [9]. The design of such a complex system, including firmware, hardware, and software, must cope with lots of physical, digital, and analog constraints, especially when the scanner has to perform 3-D imaging [50], [102]–[105].

In this chapter will be considered with special attention the requirements of the digital processing stage, comprehending data transfer bandwidths, computational costs, and data storage. As a case study, the research scanner ULA-OP 256 [20] was used to highlight possible bottlenecks and performance limitations. The study evidenced a bottleneck due to the specific architecture of the system, which limits the performance, i.e., the frame rate achievable in real-time, in high frame rate modalities. A different architecture has been proposed and experimentally compared with the current architecture.

## 6.2 Digital devices requirements

During the design and development of a real-time system, data processing and data transfer bandwidths must be studied accurately to achieve an efficient real-time processing chain. Processing capabilities and transfer bandwidths must be perfectly balanced to avoid bottlenecks that compromise the overall system performance. The following paragraphs focus on the most demanding processing stages (data acquisition and storage, beamforming, and demodulation) and on their requirements in terms of data transfer bandwidths and computational loads that are strictly requested to digital devices for real-time processing.

### *Raw data and memories*

The amount of raw data $RD$ [bit] generated to reconstruct a volume or a frame of the region of interest relates to: the number of independent channels ($N_{Ch}$), the resolution of the ADC ($S_{bit}$), the number of radiofrequency samples (or depths) acquired for each channel ($N_{depths}$), and the number of transmission events $N_{TX}$ required to reconstruct a frame or an entire volume:

$$RD = N_{Ch} \cdot N_{depths} \cdot S_{bit} \cdot N_{TX} \qquad 6.1$$

It is worth recalling that, for example, while for a line-by-line scanning $N_{TX}$ can be equal to the number of lines $N_L$ of the final image, in plane or diverging waves imaging, $N_{TX}$ could be equal to 1.

Moreover, since *RD* must be saved on memories, the latter must be fast enough to sustain the data write bandwidth ($B_{wr}$) required for the specific desired volume or frame rate $R$ [Hz]:

$$B_{wr} = RD \cdot R \qquad 6.2$$

Therefore, Eq. 6.2 defines the minimum write bandwidth that the memories must grant to correctly save the serialized bitstream. Violating this condition can lead to a bottleneck that can result in a loss of acquired data, or in reduction of performance. Once the data are saved into the memories, the beamformer can read and process them according to the beamforming algorithm. Often, the requirements on the read bandwidth of memories $B_{rd}$ could be even stricter, indeed the beamforming algorithm may require to read multiple times the same data, which are processed with different delay and weighting laws, e.g., to perform the parallel beamforming. Therefore, considering the parallel beamforming factor $(PF)$, $B_{rd}$ is:

$$B_{rd} = RD \cdot R \cdot PF = B_{wr} \cdot PF \qquad 6.3$$

which can be much higher than $B_{wr}$. Slower memories could lead to a bottleneck slowing down the beamforming stage and, therefore, limiting the performance of the system.

### *Beamforming*

The digitized raw data are processed by a digital beamformer, often implemented in FPGA. In most, if not all, scanners a Delay-and-Sum (DAS)[101] algorithm is applied to dynamically focus the echo signals. It means that for each channel, the RX delays are varied to keep the RX focal point consistent with the time of flight. Depending on the scan sequence and on the required output frame/volume rate, the beamforming can be implemented line-by-line or by multiline acquisition (also called parallel beamforming). The latter processing, typically implemented in high frame rate imaging, could be very intensive, indeed, despite the reduced number of TX events required $(N_{TX})$ to form a frame/volume, the beamformer should sustain high output data rates, sometimes even higher than the input ones. The computational effort of the parallel beamforming linearly increases with the number of parallel lines to be processed $(PF)$. However, even if the name may suggest that only parallel operations are involved, that's not true in an absolute sense, because as previously mentioned the memories used for data saving and processing are shared and must respect the memory access timings, which cannot increase linearly with the number of lines.

The DAS beamforming consists in applying dynamic delays and apodization coefficients to the acquired data, i.e., the data temporarily stored in the memory buffers. Considering the simplistic assumption that applying a delay only consists in retrieving a sample at a specific memory address, the DAS algorithm requires, for each beamformed point $(P)$, a multiplication for each channel to perform the apodization and $N_{Ch} - 1$

TABLE 6.I

OPERATIONS NEEDED FOR THE DAS ALGORITHM

| | |
|---|---|
| **SUMS** | $(N_{Ch}-1)\cdot P$ |
| **MULTIPLICATIONS** | $N_{Ch}\cdot P$ |

sums for the coherent sum. Therefore, the total number of operations need for DAS are those reported in Table 6.I.

Once the beamforming operation is performed, the beamformed data must be transferred to either the memories or the cascade processing stages. The beamformer output bandwidth $B_{Beam}$ can be computed as follows:

$$B_{Beam} = P\cdot BF_{bits}\cdot R \qquad 6.4$$

where $BF_{bits}$ is the number of bits of the beamformer output samples. Therefore, this throughput rate should be sustained by the cascade processing stages and the communication digital buses.

### *Demodulation and Filtering*

Demodulation can be performed with several techniques, but the most used one is in-phase quadrature demodulation, which involves the multiplication of beamformed data with sine and cosine samples at the demodulation frequency, low pass filtering, and downsampling of a factor $DF$. Since the demodulation is a very efficient operation, it may be neglected in the computation of the computational load. However, the output data rate $B_{Dem}$ must be considered as it can be very high, especially in (3-D) HFR imaging. The demodulation output bandwidth $B_{Dem}$ can be computed as follows:

$$B_{Dem} = \frac{P\cdot IQ_{bits}\cdot R}{DF} \qquad 6.5$$

Where $IQ_{bits}$ is the number of bits of the demodulated output samples.

### *Requirement examples for 2-D and 3-D imaging*

Table 6.II summarizes some example requirements of digital devices for some representative imaging cases considering a PRF of 1000 Hz, which in HFR imaging examples also correspond to the frame/volume rate.

The 2-D imaging cases consider a post-beamforming frame of 96 lines × 1280 samples per lines, corresponding to roughly $P$=123k beamformed points, with samples of $BF_{bits} = IQ_{bits} = 24$. The first example, reconstructs the image by a traditional line-by-line (2D-LL) scan sequence with focused TX, while the second one, is a HFR imaging sequence, based on a single plane wave (2D-PW) TX and parallel beamforming in RX (with a considered $PF = 6$). 2D-LL allows high image quality, but with limited frame rate (10 Hz with PRF =1000 Hz). In fact, in this case, even if a higher PRF is feasible, a limitation at 80Hz of FR would be anyway encountered because of the relatively high amount of raw data involved per frame. It's worth highlighting that the related bandwidth $B_{wr}$ is the same requested to 2D-PW case to reach instead a frame rate of 1000 Hz. 2D-PW case requirements, even if feasible, start stressing the system in terms of computational costs, where $31 \cdot 10^9$ operations per

TABLE 6.II

EXAMPLE OF REQUIREMENTS FOR 2-D AND 3-D IMAGING

| **2-D imaging** | | | **3-D imaging** | | | |
|---|---|---|---|---|---|---|
| **Mode** | **2D LL** | **2D PW** | **Mode** | **3D LL** | **3D-PW 256** | **3D-PW 1024** |
| **PRF [Hz]** | 1000 | 1000 | **PRF [Hz]** | 1000 | 1000 | 1000 |
| **FR [Hz]** | 10.4 | 1000 | **VR [Hz]** | 1 | 1000 | 1000 |
| **P** | 123k | 123k | **P** | 1.3M | 1.3M | 1.3M |
| **$N_{CH}$** | 128 | 128 | **$N_{CH}$** | 256 | 256 | 1024 |
| **RD [MB]** | 22.5 | 0.23 | **RD [MB]** | 480 | 0.47 | 1.88 |
| **$B_{wr}$ [MB/s]** | 234.4 | 234.4 | **$B_{wr}$ [MB/s]** | 468.8 | 468.8 | 1875 |
| **$B_{rd}$ [MB/s]** | 234.4 | 1406.3 | **$B_{rd}$ [MB/s]** | 468.8 | 2812.5 | 11250 |
| **$B_{beam}$ [MB/s]** | 3.7 | 351.6 | **$B_{beam}$ [MB/s]** | 3.7 | 3750 | 3750 |
| **$B_{dem}$ [MB/s]** | 3.7 | 351.6 | **$B_{dem}$ [MB/s]** | 3.7 | 3750 | 3750 |
| **Sums [$10^6$/s]** | 163 | 15606 | **Sums [$10^6$/s]** | 326 | 334234 | 1340867 |
| **Mult. [$10^6$/s]** | 164 | 15729 | **Mult. [$10^6$/s]** | 327 | 335544 | 1342177 |

second are required only for the beamforming, and transfer bandwidths, that are considerably higher than 2D-LL reported in table.

The 3-D imaging cases consider a relatively small volume of 32 lines × 32 lines × 1280 samples per lines, corresponding to roughly $P$=1.3M beamformed points. The first example, as in the 2D case, reconstructs the image by a traditional line-by-line (3D-LL) scan sequence with focused TX. The second and third examples are HFR imaging sequences, based on a single plane wave TX and parallel beamforming in RX (with $PF = 6$ as in 2D cases). However, the former considers a probe with 256 elements (3D-PW-256), e.g., a 2-D sparse array, while the third example consider a probe with 1024 elements (3D-PW-1024), e.g., a full 2-D matrix array. In all 3D cases, the requirements exponentially rise, due to the increased number of elements and number of points needed to reconstruct a volume. In 3D-LL case the same considerations done for the analogous 2D-LL case are still valid, but even more limiting, considering that to reconstruct a single volume is required $RD$ = 480 MB, and that the volume rate that can be reached here is of 1 Hz. The 3D-PW-256 case instead should probably be considered as a borderline case. In fact, even if actual high-end scanners may not sustain, yet, such high requirements, in terms of both computational load ($770 \cdot 10^9$ operations per second) and transfer bandwidths, most likely they will fulfill those requirements soon. It's worth highlighting also, as mentioned before, that depending on cases, in 3D-PW imaging the beamformer output bandwidth $B_{Beam}$ can be even higher than the bandwidths required to read and write raw data ($B_{wr}$ and $B_{wr}$), and that also the output demodulation bandwidth $B_{Dem}$ requested is demanding, which in these specific cases equals $B_{Beam}$ (due to $BF_{bits} = IQ_{bits}$). Finally, the 3D-PW-1024 case shows the great effort that is needed when the number of channels acquired is increased to 1024. This increase strongly impacts on the number of operations (roughly 2.8$\cdot 10^{12}$ operations per second), and all the transfer bandwidths required in the elaboration chain, especially the ones regarding raw data management, which results massive, and far to be performed in real-time with current technologies.

## 6.3 Case study: ULA-OP 256 towards 3-D high frame rate imaging

According to Table 6.II, it is quite evident that the implementation of a real-time 3-D HFR imaging system must respect very strict requirements. Although, some of them cannot be respected with the current technology level, design choices, such as the system architecture or the embedded processing devices, may imply a better or worse performance of the system. Therefore, in this case study, the ULA-OP 256 was used and thoroughly analyzed to highlight possible bottlenecks and performance limitations.

### 6.3.1 Identification of bottlenecks

The analysis of the system led to the identification of two main bottlenecks. The first one is identified by the beamformer output bandwidth ($B_{BF}$) that can output up to about 560 mega samples per second (MSPS) with a resolution of 32 bits, corresponding to an output rate of roughly 18 Gbit/s.

The second bottleneck is the data transfer bandwidth of partial beamformed data between all FE DSPs and the one embedded on the MC $B_{MC}$ that can sustain a transfer rate of 1.75 GB/s, due to the SRIO link.

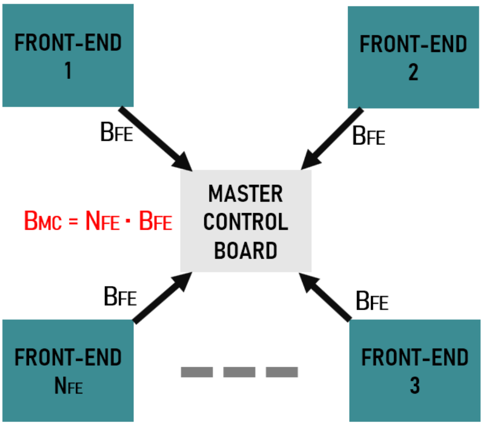

*Fig. 6-1 Schematic diagram of the star architecture highlighting the data transfer bandwidths involved. All the FE boards send the BF lines to the MC board at the same time, so the* $B_{MC}$ *requested to sustain the transfer is equal to* $N_{FE}$ *times higher the output bandwidth of a single FE* $B_{FE}$

Both bottlenecks were already shown on a previous study [22] highlighting that, in some cases, 2-D HFR imaging may by limited by the $B_{MC}$ and $B_{BF}$. Since the beamformer is quite optimized, its capacity can be hardly improved. It is implemented on the FE FPGAs whose performance is limited by the available resources (362000 logic elements, 1726 RAM blocks on each FPGA).

On the other hand, the bottleneck on $B_{MC}$ is due to the communication architecture between the FE boards and the MC board, which exploits a star configuration, as illustrated in Fig. 6-1. In detail, as previously mentioned in paragraph 3.4 , each FE FPGA produces partially beamformed data that are transferred to the dedicated DDR of the DSPs through Direct memory access. FE DSPs quadrature demodulate the received data and then transfer the partially beamformed baseband samples to the MC board, one line at a time. However, the connected FE boards ($N_{FE}$) transfer, with a bandwidth $B_{FE}$, their samples to the MC board all at the same time, and that, especially when a high number of FE boards are connected, can produce a bottleneck due to communication congestion of the master control board $B_{MC}$. Although this architecture is very efficient when a few number of lines must be transferred during the PRI or with probes having a limited number of elements, this architecture is not optimal for HFR imaging and probes with a lot of elements, i.e., it is not optimal for 3-D HFR imaging.

### 6.3.2 New ring architecture

A different communication scheme has been proposed based on a ring architecture (Fig. 6-2). In the proposed approach, a new communication channel between the DSPs on different FE boards has been opened and implemented on DSPs firmware. The channel allows transferring the partially beamformed lines from a FE DSP to the one on a neighbor FE by using the SRIO link. In details, in the new ring architecture, the DSPs of $FE_1$ transfer the first partially beamformed lines to the DSPs of $FE_2$. The DSP of the $FE_2$ after receiving the line coherently sum the line with its partial contribution, creating another accumulated partially beamformed line obtained by the sum of 64 channels. The accumulated line is then sent to the next FE DSP, which repeats the operations showed for DPS $FE_2$

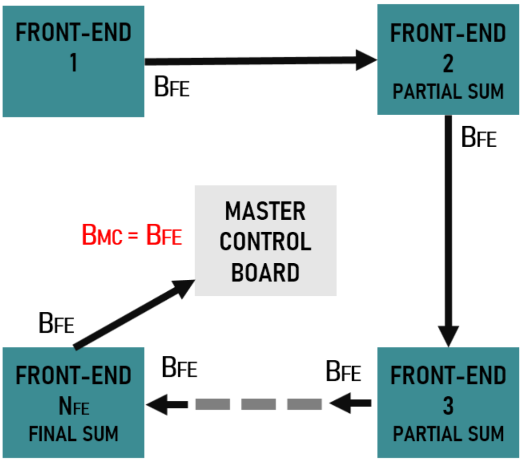

*Fig. 6-2 Schematic diagram of the ring architecture highlighting the data transfer bandwidths involved. All the FE sends the BF lines to the neighbor FE board, which accumulate its contribution to the received line. The last FE of the chain sends to the MC the final BF line. The* $B_{MC}$ *requested to sustain the transfer is equal to the output bandwidth of a single FE, i.e.,* $B_{FE}$

adding its 32 channels contribution. This operation is repeated in chain until the last FE board installed on the system is reached. The last board $FE_N$, adding its partial contribution to the accumulated line, perform, as a result, the final beamforming summation for that line. Therefore, in this architecture, only the $FE_N$ board sends data to the master control board which has to sustain a transfer bandwidth of $B_{FE}$. The ring architecture should be particularly efficient when a lot of lines must be reconstructed and transferred at high frame rate.

### 6.3.3 Experiments

The ULA-OP 256 was programmed to transmit, depending on the experiment, 1, 3, and 5 steered diverging waves (DW1, DW3, DW5) to produce HFR images/volumes (DW1) and HFR compounded images/volumes (DW3, DW5). Five experimental tests were performed in both star and ring architecture. To assess the system performance, the following metrics were evaluated: the maximum achievable pulse repetition frequency ($PRF_{Max}$), the maximum B-mode, imaging frame/volume rate ($FR_{Max}$), the average beamformer output bandwidth

TABLE 6.III

TABLE OF THE EXPERIMENTS PERFORMED ON STAR AND RING ARCHITECTURE

| | **EXP. I** | **EXP. II** | **EXP. III** | **EXP. IV** | **EXP. V** |
|---|---|---|---|---|---|
| **Mode** | DW1<br>DW3<br>DW5 | DW1<br>DW3<br>DW5 | DW1<br>DW3<br>DW5 | DW1<br>DW3<br>DW5 | DW1<br>DW5 |
| **$F_S$ [MHz]** | 39.06 | | | 26.04 | |
| **$N_{depths}$** | 1280 | | | 896 | |
| **$N_{FE}$** | 4 | 8 | 8 | 8 | 8 |
| **$N_{CH}$** | 128 | 256 | 256 | 256 | 256 |
| **$N_L$** | 96 | 96 | 96×2 | 96 | 32×30 |
| **$N_G$** | 512 | | | | |

($B_{BF}$), and the MC bandwidth ($B_{MC}$). All tests were performed with beamformed data samples $IQ_{bits}$ of 24 bit, and reconstructing images in a depth range of 25 mm (from 5 to 30 mm of depth), with 6 parallel beamformers. Table 6.III summarizes the settings used for the experiments, where the acronym DW1 DW3 and DW5 reported in table represents the imaging modes that has been tested on the specific experiment, $F_S$ the sampling rate of the system, $N_G$ the number of IQ depths and $N_L$ the number of lines.

Experiment I is the starting point. These settings were previously used in [22], to test the speed performance. Here 1280 RF samples ($N_{depths}$) are acquired at 39.06 MHz sampling frequency for 128 elements, and an image composed by 96 lines and 512 IQ depths ($N_G$) is reconstructed. Since the beamformer was upgraded after publishing the results in [22], this experiment was performed to assess the current performance of the system. Furthermore, this experiment was considered interesting to evaluate how the ring architecture performs in a configuration with a low number of FE boards, which in this case is $N_{FE}$=4.

Experiment II was introduced to demonstrate the performance with a more realistic number of elements for 3-D imaging. In fact, 2-D probes are composed at least by 256 elements. For that reason, the number of elements used in this experiment was extended to 256 and correspondingly 8 FE boards were installed. In these two examples, the 2-D probe was exploited to reconstruct a B-mode image on a single plane with a programmable rotational angle.

Experiment III was used for bi-plane imaging, where the 2-D probe is used to reconstruct at the same time 2 images of 96 lines over two different planes, i.e., a total of 192 lines.

Experiment IV instead reduced the computational load of the configuration reported in Experiment II by reducing the sampling frequency to 26.04 MHz. For the same region of interest, the number of the RF samples $N_{depths}$ are, thus, reduced from 1280 to 896. This experiment was introduced to understand whether a reduction of the number of acquired samples could relax the requirements on the memories and, thus, improve the overall system performance.

Experiment V finally considered full 3-D imaging of a small volume, composed of 32×30 lines. In this experiment the same sampling frequency of Experiment IV was used, not to overload the system considering the great effort already requested for a volumetric reconstruction. The modes tested here are DW1 and DW5. DW3 mode was not implemented in this experiment, although technically possible, because with the transmission of three DWs it would not be possible to perform a symmetrical insonification of the region of interest, necessary to ensure the same compound image quality on both lateral directions of the volume.

### 6.3.4 Results

The tables reported in this paragraph summarize the performance of the system for the 5 tested experiments. For each experiment, the PRF was initially set to 100 Hz, then it was step-by-step increased, with a minimum step of 50 Hz for the initial increments, and 10Hz for the fine tuning, until the system worked stably (with exception for the last experiment which required a lower starting PRF and finer steps). The highest PRF at which the system was stable was considered as $PRF_{Max}$. Depending on the experiment, instability could be caused by beamforming limits, data transfer rate bottlenecks, or number of simultaneous memory accesses. Once the $PRF_{Max}$ was determined, the $FR_{Max}$ was computed according to the scan sequence and the number of compounded images. Moreover, the tables report the estimated beamforming output data rate $B_{BF}$ and the MC transfer bandwidth $B_{MC}$. The results of the five experiments are reported in Table 6.IV, where all the metrics that correspond to the achievement of the maximum limit (bottleneck) are highlighted in orange.

TABLE 6.IV

SYSTEM PERFORMANCE OBTAINED FOR THE DIFFERENT EXPERIMENTS

| | | **Experiment I** | | | **Experiment II** | | |
|---|---|---|---|---|---|---|---|
| | | **DW1** | **DW3** | **DW5** | **DW1** | **DW3** | **DW5** |
| **STAR** | PRF$_{MAX}$ [Hz] | 1500 | 4500 | 4500 | 750 | 2200 | 3700 |
| | FR$_{MAX}$ [Hz] | 1500 | 1500 | 900 | 750 | 733 | 740 |
| | B$_{BF}$ [MSPS] | 184 | 553 | 553 | 92 | 270 | 455 |
| | B$_{MC}$ [GB/s] | 1.77 | 1.77 | 1.06 | 1.77 | 1.73 | 1.75 |
| **RING** | PRF$_{MAX}$ [Hz] | 1800 | 3400 | 4300 | 1800 | 3400 | 3900 |
| | FR$_{MAX}$ [Hz] | 1800 | 1133 | 860 | 1800 | 1133 | 780 |
| | B$_{BF}$ [MSPS] | 221 | 418 | 528 | 221 | 418 | 479 |
| | B$_{MC}$ [GB/s] | 0.53 | 0.33 | 0.25 | 0.53 | 0.33 | 0.23 |

| | | **Experiment III** | | | **Experiment IV** | | |
|---|---|---|---|---|---|---|---|
| | | **DW1** | **DW3** | **DW5** | **DW1** | **DW3** | **DW5** |
| **STAR** | PRF$_{MAX}$ [Hz] | 360 | 1100 | 1850 | 750 | 2300 | 3800 |
| | FR$_{MAX}$ [Hz] | 360 | 366 | 370 | 750 | 766 | 760 |
| | B$_{BF}$ [MSPS] | 88 | 270 | 455 | 65 | 198 | 327 |
| | B$_{MC}$ [GB/s] | 1.70 | 1.73 | 1.75 | 1.77 | 1.81 | 1.79 |
| **RING** | PRF$_{MAX}$ [Hz] | 900 | 1400 | 1900 | 2600 | 5800 | 5800 |
| | FR$_{MAX}$ [Hz] | 900 | 467 | 380 | 2600 | 1933 | 1160 |
| | B$_{BF}$ [MSPS] | 221 | 344 | 467 | 224 | 499 | 499 |
| | B$_{MC}$ [GB/s] | 0.53 | 0.28 | 0.22 | 0.77 | 0.57 | 0.34 |

| | | **Experiment V** | |
|---|---|---|---|
| | | **DW1** | **DW5** |
| **STAR** | PRF$_{MAX}$ [Hz] | 75 | 320 |
| | FR$_{MAX}$ [Hz] | 75 | 64 |
| | B$_{BF}$ [MSPS] | 65 | 275 |
| | B$_{MC}$ [GB/s] | 1.77 | 1.51 |
| **RING** | PRF$_{MAX}$ [Hz] | 260 | 650 |
| | FR$_{MAX}$ [Hz] | 260 | 130 |
| | B$_{BF}$ [MSPS] | 224 | 559 |
| | B$_{MC}$ [GB/s] | 0.77 | 0.38 |

The results of Experiment I ( Table 6.IV top left), shows that, in case of 4 FE boards installed, the frame rate reachable with both star and ring architectures are comparable. In the star architecture the $FR_{Max}$ is 1500 Hz and reached in case DW1 and DW3. In both cases, the bottleneck was due to the SRIO link between the FE boards and the MC board, which can reach a maximum bandwidth of 1.75-1.80 GB/s. In the ring architecture the performance improved for DW1 and the $FR_{Max}$ resulted 1800 Hz. However, the performance slightly worsened for DW3 and DW5. This behavior was expected since the ring architecture should perform the best with a high $N_{FE}$. It is worth highlighting that the beamformer was close to its maximum output data rate (roughly 560 MSPS) for DW3 and DW5 in the star architecture.

The results of Experiment II (Table 6.IV top right), show that, although $N_{FE}$ increased w.r.t. Experiment I, the performance for the ring architecture did not change, while for the star architecture the $FR_{Max}$ halved. This can be explained considering that a doubled $N_{FE}$ corresponds, in the star architecture, to doubling the required $B_{MC}$, while it does not depend on $N_{FE}$ for the ring architecture. Overall, in Experiment II, the ring architecture performed up to 2.4 times better than the star architecture.

Although results of experiment III (Table 6.IV middle left), confirm that the performance linearly depends on the number of reconstructed lines. Indeed, doubling the number of reconstructed lines (192), w.r.t. Experiment II, resulted in a halved $FR_{Max}$. The table highlight that for the star architecture the bottleneck is still $B_{MC}$, which explain the halved $FR_{Max}$. However, the reason why the frame rate halved also for the ring architecture must be explained with a congestion on memory accesses. For that reason, as previously explained in experiment section, a configuration with a lower number of RF samples, was tested in experiment IV.

The results of Experiment IV (Table 6.IV middle right), highlight that relaxing the requirements on the memories by reducing the number of read/write cycles, does not impact on the performance of the star architecture, which performs as in Experiment II. Although less samples were beamformed the saturation of $B_{MC}$ still limited $FR_{Max}$. On the other hand, in the ring architecture, relaxing the requirements on the memories led to a considerable $FR_{Max}$ increase, roughly 50% w.r.t. Experiment II.

Finally, Experiment V assessed the system performance for a full volume HFR imaging composed by 32×30 lines. Results (Table 6.IV bottom left) show that, in the star architecture, $FR_{Max}$ resulted 75 Hz in DW1 mode, and reached 64 Hz in DW5 mode. However, in both cases, the bottleneck was the saturation of $B_{MC}$. On the other hand, the ring architecture enabled higher $FR_{Max}$, up to 260 Hz in DW1 mode and reached 130 Hz in DW5 mode, where instead the bottleneck was $B_{BF}$. Therefore, these results confirmed that the ring architecture is more suitable than the star architecture for 3-D HFR imaging, where a considerable number of lines must be reconstructed for each PRI.

## 6.4 Discussion an conclusion

The reduction of the bandwidth $B_{MC}$ occupied in the transfer of beamformed data to the MC board is reduced by the ring architecture by a factor equivalent to $N_{FE}$ boards used in the system configuration. The reduction of $B_{MC}$ involved in the ring architecture allowed increasing the system performance for those modes that were limited by the saturation of $B_{MC}$ in the star architecture. However, although $B_{MC}$ is reduced by a factor $N_{FE}$, the improvement of $FR_{Max}$ does not increase by the same factor. Indeed, other digital bottlenecks limit the system performance, e.g., the beamforming output rate and the number of simultaneous accesses to the memories. Implementing a smarter manager of the multiple accesses to memories could further increase the ring architecture performance, however it was not investigated in this study and will be implemented and tested in a future work. Despite this limitation, the experimental results, obtained for the 5 experiments, showed that the ring architecture is profitable when a high number of FE boards ($N_{FE}$>4) are installed in the system, i.e., when several elements are used in TX/RX as in the case of 3-D imaging.

It is worth highlighting that the modes based on multiple DW transmissions (DW3, DW5) and RX coherent compounding always allow achieving higher $PRF_{Max}$: the higher the number of compounded waves, the higher $PRF_{Max}$. For the star architecture, since the bottleneck is often the saturation of $B_{MC}$, an increased number of diverging waves does not impact on $FR_{Max}$. Even if this could appear counterintuitive, in fact, the compounding helps the star architecture to get the most out of the beamforming stage, which in DW1 mode is not adequately exploited because the saturation of $B_{MC}$ is dependent on the output frame rate. For the ring architecture, compounding allows a better exploitation of the beamformer, however, as intuitively expected, the highest $FR_{Max}$ is always obtained with DW1. In these cases, since the $B_{MC}$ requirements are relaxed, the bottlenecks are the number of memory accesses and the additional computational load due to compounding. Nevertheless, it is worth highlighting that the ring architecture w.r.t. to the star architecture always achieves higher $FR_{Max}$ (except for experiment I).

Experiment V deserves some additional considerations as it highlights what really are the requirements and capabilities of a real-time HFR system for volumetric imaging. In fact, although the number of lines reconstructed in the volume was relatively small (32×30), the ULA-OP 256 enabled a maximum $FR_{Max}$ of 260 Hz and 130 Hz in DW1 and DW5 mode, respectively. Such a frame rate, although lower the maximum achievable in theory, is high enough for morphological imaging, but could also enable the cascade processing for those methods based on contour or speckle tracking algorithms and achieve high temporal resolutions. However, still, the volume rate is not high enough for Doppler based methods.

In conclusion, the proposed ring architecture resulted efficient in increasing the overall system performance of the ULA-OP 256 in high-rate imaging. Even if this first implementation still presents some limitation that need to be further investigated, these results, move the first step towards HFR 3-D imaging in real-time.

As a final consideration regarding 3-D imaging, a special attention should be surely given to all the techniques that could increase the image quality and reduce the overall computational effort of the system. 3-D imaging in fact, may suffer of a low contrast of the images produced, so could be interesting apply all the techniques proposed in 2-D imaging to increase contrast and spatial resolution [8], [106]–[108]. Furthermore, some exciting approaches for efficient delay calculations [104], or machine and deep learning based techniques such as compress sensing [109], intelligent sub-sampling and frequency domain beamforming [110], [111], compressed and adaptive beamforming [112], [113] look more than ever appetible for 3-D imaging systems to increase both image quality and systems performance, pushing future work to be focused also on these techniques.

# Chapter 7. Conclusion

*This chapter summarizes the contributions of the thesis and discusses possible directions for future research.*

## 7.1 Summary of contributions

This PhD project has provided contributions to the development of novel ultrasound modalities on the research scanner ULA-OP 256. Real-time implementation and experimental test of 2-D, 3-D, and HFR imaging modalities have been reported.

In particular:

- A new US modality called Virtual-real-time was developed and tested on ULA-OP 256. The possibility of re-processing raw data, previously stored on the memories, at a lower rate, provides a new way of displaying HFR images and allows overcoming the processing bottlenecks that happen in real-time for computationally demanding methods. This capability resulted particularly useful for the MLVD method, which was shown capable of working at increased PRF (up to 16 kHz), and for HFR color flow imaging, which could work at improved temporal/spatial resolution.
- The ULA-OP 256 firmware and software were modified to make the scanner capable of working with 2-D probes of arbitrary geometries. It was thus possible to simultaneously image multiple (selectable) planes in a volume. Two different applications were tested by using a sparse spiral array probe. In the first application, bi-plane imaging was implemented for the robust assessment of flow-mediated dilation. In the second application, two planes, each with programmable azimuth angle, were scanned in real-time, and arbitrarily oriented Doppler lines were set to produce real-time 3-D spectral Doppler analysis.
- A study on the requirements of the digital receiving stage of scanners performing 3-D HFR imaging was conducted. The study was applied to the ULA-OP 256, and revealed that the star architecture used to transfer beamformed data among the boards of systems encountered a bandwidth saturation that limited the scanner performance during HFR imaging. A new ring architecture, performing a partial summation of the beamformed data in each front-end board, was proposed, implemented, and tested. The results showed that the new architecture increased the performance of the scanner, which

permitted the processing of small volumes at volume rates up to 260 Hz.

## 7.2 Directions of future work

The capability of virtual real-time modality of immediately re-process ultrasound acquisitions on the same real-time user interface offers some interesting scenarios that encourage clinical tests. This new tool, in fact, could help medical researchers and expert physicians to obtain in a practical way more informations and a new perspective on the phenomena of interest, exploiting complex and high-resolution (in time and space) imaging methods otherwise feasible only in a successive post-processing phase. Of significative interest could be also the implementation of this modality in portable devices like the point-of-care devices, which could overcome their limited computational power, providing to the physicians new imaging possibilities.

The recent introduction of systems capable of 3-D imaging opens the road to many exciting imaging possibilities such as the visualization of ultrasound data with volume rendered images. However, the adoption of a new way to manage ultrasound informations in the clinical practice may require some time. The multi-plane modes discussed in this thesis, could be a first step to introduce the potentiality of 3-D imaging in the clinical practice and suggests clinical tests.

The proposed bi-plane imaging for a robust assessment of Flow Mediated Dilation exam, could help this already validated exam to overcome its limitations, that at the moment confine its spread mostly for research protocols. If confirmed by clinical tests, the bi-plane approach could be a robust and promising tool for early diagnosis and follow-up of atherosclerosis and cardiovascular diseases, and hopefully could become a spread routine clinical exam.

The real-time 3-D Spectral Doppler Analysis proposed may give to physicians the opportunity to effectively assess the dynamics of blood flow within an entire volume of interest, with two programmable planes. Possible future developments comprehending a better navigation system, and, possibly, an automatic system to determine the best imaging planes for the specific anatomy of the subject, could make this imaging mode an easy and comprehensive 3-D imaging tool.

Finally, the implementation of the new digital architecture of ULA-OP 256 made a new step on the development of real-time HFR 3-D imaging methods, which require demanding system performance. The promising results in terms of performance, strongly suggest further developments based on the implementation of data compression techniques and newer Artificial Intelligence techniques for advanced beamforming and automatic detection of the regions of interest. These techniques may relax the system requirements, increase the image quality, and support the physicians during the examinations, and thus, finally enable the system to perform the next generation of 3-D HFR advanced imaging methods.

# Bibliography

[1] J. M. Baran and J. G. Webster, “Design of low-cost portable ultrasound systems: Review,” in *2009 Annual International Conference of the IEEE Engineering in Medicine and Biology Society*, Sep. 2009, pp. 792–795. doi: 10.1109/IEMBS.2009.5332754.

[2] A. S. Savoia, G. Caliano, and M. Pappalardo, “A CMUT probe for medical ultrasonography: from microfabrication to system integration,” *IEEE Transactions on Ultrasonics, Ferroelectrics, and Frequency Control*, vol. 59, no. 6, pp. 1127–1138, Jun. 2012, doi: 10.1109/TUFFC.2012.2303.

[3] S. W. Smith, O. T. von Ramm, M. E. Haran, and F. L. Thurstone, “Angular response of piezoelectric elements in phased array ultrasound scanners,” *IEEE Transactions on Sonics and Ultrasonics*, vol. 26, no. 3, pp. 185–190, May 1979, doi: 10.1109/T-SU.1979.31085.

[4] O. Martínez-Graullera, C. J. Martín, G. Godoy, and L. G. Ullate, “2D array design based on Fermat spiral for ultrasound imaging,” *Ultrasonics*, vol. 50, no. 2, Art. no. 2, Feb. 2010, doi: 10.1016/j.ultras.2009.09.010.

[5] A. Ramalli, E. Boni, A. S. Savoia, and P. Tortoli, “Density-tapered spiral arrays for ultrasound 3-D imaging,” *IEEE Transactions on Ultrasonics, Ferroelectrics, and Frequency Control*, vol. 62, no. 8, pp. 1580–1588, Aug. 2015, doi: 10.1109/TUFFC.2015.007035.

[6] P. Mattesini, A. Ramalli, L. Petrusca, O. Basset, H. Liebgott, and P. Tortoli, “Spectral Doppler Measurements With 2-D Sparse Arrays,” *IEEE Transactions on Ultrasonics, Ferroelectrics, and Frequency Control*, vol. 67, no. 2, pp. 278–285, Feb. 2020, doi: 10.1109/TUFFC.2019.2944090.

[7] A. Stuart Savoia *et al.*, “A 256-Element Spiral CMUT Array with Integrated Analog Front End and Transmit Beamforming Circuits,” in *2018 IEEE International Ultrasonics Symposium (IUS)*, Oct. 2018, pp. 206–212. doi: 10.1109/ULTSYM.2018.8579867.

[8] L. Wei *et al.*, “High Frame Rate Volumetric Imaging of Microbubbles Using a Sparse Array and Spatial Coherence Beamforming,” *IEEE Transactions on Ultrasonics, Ferroelectrics, and Frequency Control*, vol. 68, no. 10, pp. 3069–3081, Oct. 2021, doi: 10.1109/TUFFC.2021.3086597.

[9] E. Boni, A. C. H. Yu, S. Freear, J. A. Jensen, and P. Tortoli, “Ultrasound Open Platforms for Next-Generation Imaging Technique Development,” *IEEE Transactions on Ultrasonics, Ferroelectrics, and Frequency Control*, vol. 65, no. 7, pp. 1078–1092, Jul. 2018, doi: 10.1109/TUFFC.2018.2844560.

[10] P. Tortoli, F. Guidi, G. Guidi, and C. Atzeni, “Spectral velocity profiles for detailed ultrasound flow analysis,” *IEEE Transactions on Ultrasonics, Ferroelectrics and Frequency Control*, vol. 43, no. 4, pp. 654–659, Jul. 1996, doi: 10.1109/58.503727.

[11] M. Lenge, A. Ramalli, E. Boni, H. Liebgott, C. Cachard, and P. Tortoli, “High-frame-rate 2-D vector blood flow imaging in the frequency domain,” *IEEE Transactions on Ultrasonics, Ferroelectrics, and Frequency Control*, vol. 61, no. 9, pp. 1504–1514, Sep. 2014, doi: 10.1109/TUFFC.2014.3064.

[12] C. Kasai, K. Namekawa, A. Koyano, and R. Omoto, “Real-Time Two-Dimensional Blood Flow Imaging Using an Autocorrelation Technique,” *IEEE Transactions on Sonics and Ultrasonics*, vol. 32, no. 3, pp. 458–464, May 1985, doi: 10.1109/T-SU.1985.31615.

[13] M. Tanter and M. Fink, “Ultrafast imaging in biomedical ultrasound,” *IEEE Transactions on Ultrasonics, Ferroelectrics, and Frequency Control*, vol. 61, no. 1, pp. 102–119, Jan. 2014, doi: 10.1109/TUFFC.2014.2882.

[14] J. Provost, C. Papadacci, C. Demene, J. L. Gennisson, M. Tanter, and M. Pernot, “3-D ultrafast doppler imaging applied to the noninvasive mapping of blood vessels in Vivo,” *IEEE Transactions on Ultrasonics, Ferroelectrics, and Frequency Control*, vol. 62, no. 8, pp. 1467–1472, Aug. 2015, doi: 10.1109/TUFFC.2015.007032.

[15] C. C. P. Cheung *et al.*, “Multi-channel pre-beamformed data acquisition system for research on advanced ultrasound imaging methods,” *IEEE Transactions on Ultrasonics, Ferroelectrics and Frequency Control*, vol. 59, no. 2, pp. 243–253, Feb. 2012, doi: 10.1109/TUFFC.2012.2184.

[16] M. Lewandowski, M. Walczak, B. Witek, P. Kulesza, and K. Sielewicz, “Modular & scalable ultrasound platform with GPU processing,” 2012.

[17] B. Y. S. Yiu, I. K. H. Tsang, and A. C. H. Yu, “GPU-based beamformer: Fast realization of plane wave compounding and synthetic aperture imaging,” *IEEE Transactions on Ultrasonics, Ferroelectrics, and Frequency Control*, vol. 58, no. 8, pp. 1698–1705, Aug. 2011, doi: 10.1109/TUFFC.2011.1999.

[18] H. So, J. Chen, B. Yiu, and A. Yu, “Medical Ultrasound Imaging: To GPU or Not to GPU?,” *IEEE Micro*, vol. 31, no. 5, pp. 54–65, Sep. 2011, doi: 10.1109/MM.2011.65.

[19] J. A. Jensen *et al.*, “Ultrasound research scanner for real-time synthetic aperture data acquisition,” *IEEE Trans Ultrason Ferroelectr Freq Control*, vol. 52, no. 5, pp. 881–891, May 2005.

[20] E. Boni *et al.*, “ULA-OP 256: A 256-Channel Open Scanner for Development and Real-Time Implementation of New Ultrasound Methods,” *IEEE Transactions on Ultrasonics, Ferroelectrics, and Frequency Control*, vol. 63, no. 10, pp. 1488–1495, Oct. 2016, doi: 10.1109/TUFFC.2016.2566920.

[21] B. Y. S. Yiu, M. Walczak, M. Lewandowski, and A. C. H. Yu, “Live Ultrasound Color-Encoded Speckle Imaging Platform for Real-Time Complex Flow Visualization In Vivo,” *IEEE Transactions on Ultrasonics, Ferroelectrics, and Frequency Control*, vol. 66, no. 4, pp. 656–668, Apr. 2019, doi: 10.1109/TUFFC.2019.2892731.

[22] E. Boni *et al.*, “Architecture of an Ultrasound System for Continuous Real-Time High Frame Rate Imaging,” *IEEE Transactions on Ultrasonics, Ferroelectrics, and Frequency Control*, vol. 64, no. 9, pp. 1276–1284, Sep. 2017, doi: 10.1109/TUFFC.2017.2727980.

[23] P. Tortoli, G. Bambi, F. Guidi, and R. Muchada, “Toward a better quantitative measurement of aortic flow,” *Ultrasound Med Biol*, vol. 28, no. 2, pp. 249–257, Feb. 2002, doi: 10.1016/s0301-5629(01)00462-8.

[24] D. H. Evans and W. N. McDicken, *Doppler Ultrasound: Physics, Instrumentation and Signal Processing*, 2nd Edition. Wiley-Blackwell, 1999.

[25] J. A. Jensen, S. I. Nikolov, A. C. H. Yu, and D. Garcia, “Ultrasound Vector Flow Imaging—Part II: Parallel Systems,” *IEEE Transactions on Ultrasonics, Ferroelectrics, and Frequency Control*, vol. 63, no. 11, pp. 1722–1732, Nov. 2016, doi: 10.1109/TUFFC.2016.2598180.

[26] I. K. Ekroll, H. Torp, L. Lovstakken, A. Swillensz, and P. Segersz, “Simultaneous quantification of flow and tissue velocities based on multi-angle plane wave imaging with an extended velocity range,” in *Ultrasonics Symposium (IUS), 2011 IEEE International*, Oct. 2011, pp. 438–441. doi: 10.1109/ULTSYM.2011.0105.

[27] P. Tortoli, G. Bambi, and S. Ricci, “Accurate Doppler angle estimation for vector flow measurements,” *IEEE Transactions on Ultrasonics, Ferroelectrics, and Frequency Control*, vol. 53, no. 8, pp. 1425–1431, Aug. 2006, doi: 10.1109/TUFFC.2006.1665099.

[28] S. Ricci, A. Ramalli, L. Bassi, E. Boni, and P. Tortoli, “Real-Time Blood Velocity Vector Measurement Over a 2-D Region,” *IEEE Transactions on Ultrasonics, Ferroelectrics, and Frequency Control*, vol. 65, no. 2, pp. 201–209, Feb. 2018, doi: 10.1109/TUFFC.2017.2781715.

[29] B. Y. S. Yiu and A. C. H. Yu, “High-Frame-Rate Ultrasound Color-Encoded Speckle Imaging of Complex Flow Dynamics,” *Ultrasound in Medicine & Biology*, vol. 39, no. 6, pp. 1015–1025, Jun. 2013, doi: 10.1016/j.ultrasmedbio.2012.12.016.

[30] P. Joos *et al.*, “High-Frame-Rate Speckle-Tracking Echocardiography,” *IEEE Transactions on Ultrasonics, Ferroelectrics, and Frequency Control*, vol. 65, no. 5, pp. 720–728, May 2018, doi: 10.1109/TUFFC.2018.2809553.

[31] E. G. Grant *et al.*, “Carotid Artery Stenosis: Gray-Scale and Doppler US Diagnosis—Society of Radiologists in Ultrasound Consensus Conference,” *Radiology*, vol. 229, no. 2, pp. 340–346, Nov. 2003, doi: 10.1148/radiol.2292030516.

[32] P. Tortoli, “A tracking FFT processor for pulsed Doppler analysis beyond the Nyquist limit (medical ultrasound),” *IEEE Transactions on Biomedical Engineering*, vol. 36, no. 2, pp. 232–237, Feb. 1989, doi: 10.1109/10.16470.

[33] D. Posada *et al.*, “Staggered Multiple-PRF Ultrafast Color Doppler,” *IEEE Transactions on Medical Imaging*, vol. 35, no. 6, pp. 1510–1521, Jun. 2016, doi: 10.1109/TMI.2016.2518638.

[34] C. Giangrossi *et al.*, “Virtual real-time: a new US operating modality,” in *2019 IEEE International Ultrasonics Symposium (IUS)*, Oct. 2019, pp. 1493–1496. doi: 10.1109/ULTSYM.2019.8926259.

[35] V. Meacci *et al.*, “High velocity investigation with Multi Line Vector Doppler,” in *2019 IEEE International Ultrasonics Symposium (IUS)*, Oct. 2019, pp. 360–363. doi: 10.1109/ULTSYM.2019.8925613.

[36] B. Dunmire, K. W. Beach, K.-H. Labs, M. Plett, and D. E. Strandness Jr., “Cross-beam vector Doppler ultrasound for angle-independent velocity measurements,” *Ultrasound in Medicine & Biology*, vol. 26, no. 8, pp. 1213–1235, Oct. 2000, doi: 10.1016/S0301-5629(00)00287-8.

[37] S. Ricci, L. Bassi, and P. Tortoli, “Real-time vector velocity assessment through multigate Doppler and plane waves,” *IEEE Transactions on Ultrasonics, Ferroelectrics, and Frequency Control*, vol. 61, no. 2, pp. 314–324, Feb. 2014, doi: 10.1109/TUFFC.2014.6722616.

[38] S. S. M. Lai, B. Y. S. Yiu, A. K. K. Poon, and A. C. H. Yu, “Design of Anthropomorphic Flow Phantoms Based on Rapid Prototyping of Compliant Vessel Geometries,” *Ultrasound in Medicine & Biology*, vol. 39, no. 9, pp. 1654–1664, Sep. 2013, doi: 10.1016/j.ultrasmedbio.2013.03.015.

[39] K. V. Ramnarine, D. K. Nassiri, P. R. Hoskins, and J. Lubbers, “Validation of a New Blood-Mimicking Fluid for Use in Doppler Flow Test Objects,” *Ultrasound in Medicine & Biology*, vol. 24, no. 3, pp. 451–459, Mar. 1998, doi: 10.1016/S0301-5629(97)00277-9.

[40] S. Ricci, L. Bassi, A. Dallai, R. Matera, and P. Tortoli, “Real-time staggered PRF for vector Doppler blood velocity assessment,” in *2017 IEEE International Ultrasonics Symposium (IUS)*, Sep. 2017, pp. 1–4. doi: 10.1109/ULTSYM.2017.8091797.

[41] D. H. Evans, J. A. Jensen, and M. B. Nielsen, “Ultrasonic colour Doppler imaging,” *Interface Focus*, vol. 1, no. 4, pp. 490–502, Aug. 2011, doi: 10.1098/rsfs.2011.0017.

[42] J. Bercoff *et al.*, “Ultrafast compound doppler imaging: providing full blood flow characterization,” *IEEE Transactions on Ultrasonics, Ferroelectrics, and Frequency Control*, vol. 58, no. 1, pp. 134–147, Jan. 2011, doi: 10.1109/TUFFC.2011.1780.

[43] B. Denarie *et al.*, “Coherent Plane Wave Compounding for Very High Frame Rate Ultrasonography of Rapidly Moving Targets,” *IEEE Transactions on Medical Imaging*, vol. 32, no. 7, pp. 1265–1276, Jul. 2013, doi: 10.1109/TMI.2013.2255310.

[44] I. K. Ekroll, M. M. Voormolen, O. K.-V. Standal, J. M. Rau, and L. Lovstakken, “Coherent compounding in doppler imaging,” *IEEE Transactions on Ultrasonics, Ferroelectrics, and Frequency Control*, vol. 62, no. 9, pp. 1634–1643, Sep. 2015, doi: 10.1109/TUFFC.2015.007010.

[45] C. Demené *et al.*, “Spatiotemporal Clutter Filtering of Ultrafast Ultrasound Data Highly Increases Doppler and fUltrasound Sensitivity,” *IEEE Transactions on Medical Imaging*, vol. 34, no. 11, pp. 2271–2285, Nov. 2015, doi: 10.1109/TMI.2015.2428634.

[46] J. A. Jensen *et al.*, “SARUS: A synthetic aperture real-time ultrasound system,” *IEEE Transactions on Ultrasonics, Ferroelectrics, and Frequency Control*, vol. 60, no. 9, pp. 1838–1852, Sep. 2013, doi: 10.1109/TUFFC.2013.2770.

[47] F. Guidi and P. Tortoli, “Real-Time High Frame Rate Color Flow Mapping System,” *IEEE Transactions on Ultrasonics, Ferroelectrics, and Frequency Control*, vol. 68, no. 6, pp. 2193–2201, Jun. 2021, doi: 10.1109/TUFFC.2021.3064612.

[48] Ultrasonix, “Touch Screen Ultrasound System - SonixTouch,” 2012. http://www.ultrasonix.com/ultrasound-systems/sonixtouch (accessed Dec. 12, 2012).

[49] J. Provost *et al.*, “3D ultrafast ultrasound imaging in vivo,” *Phys Med Biol*, vol. 59, no. 19, Art. no. 19, Oct. 2014, doi: 10.1088/0031-9155/59/19/L1.

[50] Q. Huang and Z. Zeng, “A Review on Real-Time 3D Ultrasound Imaging Technology,” *BioMed Research International*, vol. 2017, p. e6027029, Mar. 2017, doi: 10.1155/2017/6027029.

[51] A. Ramalli *et al.*, “High-Frame-Rate Tri-Plane Echocardiography With Spiral Arrays: From Simulation to Real-Time Implementation,” *IEEE Transactions on Ultrasonics, Ferroelectrics, and Frequency Control*, vol. 67, no. 1, pp. 57–69, Jan. 2020, doi: 10.1109/TUFFC.2019.2940289.

[52] S. Harput *et al.*, “3-D Super-Resolution Ultrasound Imaging With a 2-D Sparse Array,” *IEEE Transactions on Ultrasonics, Ferroelectrics, and Frequency Control*, vol. 67, no. 2, Art. no. 2, Feb. 2020, doi: 10.1109/TUFFC.2019.2943646.

[53] K. E. Pyke, E. M. Dwyer, and M. E. Tschakovsky, “Impact of controlling shear rate on flow-mediated dilation responses in the brachial artery of humans,” *Journal of Applied Physiology*, vol. 97, no. 2, pp. 499–508, Aug. 2004, doi: 10.1152/japplphysiol.01245.2003.

[54] J. Yeboah, J. R. Crouse, F.-C. Hsu, G. L. Burke, and D. M. Herrington, “Brachial Flow-Mediated Dilation Predicts Incident Cardiovascular Events in Older Adults,” *Circulation*, vol. 115, no. 18, pp. 2390–2397, May 2007, doi: 10.1161/CIRCULATIONAHA.106.678276.

[55] A. Gnasso *et al.*, “Association between wall shear stress and flow-mediated vasodilation in healthy men,” *Atherosclerosis*, vol. 156, no. 1, pp. 171–176, May 2001, doi: 10.1016/S0021-9150(00)00617-1.

[56] T. G. Papaioannou, E. N. Karatzis, M. Vavuranakis, J. P. Lekakis, and C. Stefanadis, “Assessment of vascular wall shear stress and implications for atherosclerotic disease,” *International Journal of Cardiology*, vol. 113, no. 1, pp. 12–18, Oct. 2006, doi: 10.1016/j.ijcard.2006.03.035.

[57] L. Ghiadoni, M. Salvetti, M. L. Muiesan, and S. Taddei, “Evaluation of Endothelial Function by Flow Mediated Dilation: Methodological Issues and Clinical Importance,” *High Blood Press Cardiovasc Prev*, vol. 22, no. 1, pp. 17–22, Mar. 2015, doi: 10.1007/s40292-014-0047-2.

[58] J. Yeboah *et al.*, “Predictive Value of Brachial Flow-Mediated Dilation for Incident Cardiovascular Events in a Population-Based Study,” *Circulation*, vol. 120, no. 6, pp. 502–509, Aug. 2009, doi: 10.1161/CIRCULATIONAHA.109.864801.

[59] M. C. Corretti *et al.*, “Guidelines for the ultrasound assessment of endothelial-dependent flow-mediated vasodilation of the brachial artery: A report of the International Brachial Artery Reactivity Task Force,” *Journal of the American College of Cardiology*, vol. 39, no. 2, pp. 257–265, Jan. 2002, doi: 10.1016/S0735-1097(01)01746-6.

[60] P. Tortoli, C. Palombo, L. Ghiadoni, G. Bini, and L. Francalanci, “Simultaneous ultrasound assessment of brachial artery shear stimulus and flow-mediated dilation during reactive hyperemia,” *Ultrasound Med Biol*, vol. 37, no. 10, pp. 1561–1570, Oct. 2011, doi: 10.1016/j.ultrasmedbio.2011.06.001.

[61] A. Ramalli *et al.*, “Continuous Simultaneous Recording of Brachial Artery Distension and Wall Shear Rate: A New Boost for Flow-Mediated Vasodilation,” *IEEE Transactions on Ultrasonics, Ferroelectrics, and*

*Frequency Control*, vol. 66, no. 3, pp. 463–471, Mar. 2019, doi: 10.1109/TUFFC.2018.2889111.

[62] A. F. Frangi, M. Laclaustra, and P. Lamata, “A registration-based approach to quantify flow-mediated dilation (FMD) of the brachial artery in ultrasound image sequences,” *IEEE Transactions on Medical Imaging*, vol. 22, no. 11, pp. 1458–1469, Nov. 2003, doi: 10.1109/TMI.2003.819278.

[63] V. Gemignani, F. Faita, L. Ghiadoni, E. Poggianti, and M. Demi, “A System for Real-Time Measurement of the Brachial Artery Diameter in B-Mode Ultrasound Images,” *IEEE Transactions on Medical Imaging*, vol. 26, no. 3, pp. 393–404, Mar. 2007, doi: 10.1109/TMI.2006.891477.

[64] A. Nowicki *et al.*, “20-MHz Ultrasound for Measurements of Flow-Mediated Dilation and Shear Rate in the Radial Artery,” *Ultrasound in Medicine & Biology*, vol. 44, no. 6, Art. no. 6, Jun. 2018, doi: 10.1016/j.ultrasmedbio.2018.02.011.

[65] K. Aizawa *et al.*, “Brachial artery vasodilatory response and wall shear rate determined by multigate Doppler in a healthy young cohort,” *Journal of Applied Physiology*, vol. 124, no. 1, pp. 150–159, Nov. 2017, doi: 10.1152/japplphysiol.00310.2017.

[66] K. Aizawa *et al.*, “Arterial wall shear rate response to reactive hyperaemia is markedly different between young and older humans,” *J Physiol*, vol. 597, no. 16, pp. 4151–4163, Aug. 2019, doi: 10.1113/JP278310.

[67] P. Tortoli, G. Guidi, P. Berti, F. Guidi, and D. Righi, “An FFT-based flow profiler for high-resolution in vivo investigations,” *Ultrasound in Medicine & Biology*, vol. 23, no. 6, pp. 899–910, 1997, doi: 10.1016/S0301-5629(97)00017-3.

[68] M. Demi, M. Paterni, and A. Benassi, “The First Absolute Central Moment in Low-Level Image Processing,” *Computer Vision and Image Understanding*, vol. 80, no. 1, pp. 57–87, Oct. 2000, doi: 10.1006/cviu.2000.0861.

[69] “Doppler Ultrasound in Obstetrics and Gynecology,” 2005, doi: 10.1007/3-540-28903-8.

[70] I. M. Coman and B. A. Popescu, “Shigeo Satomura: 60 years of Doppler ultrasound in medicine,” *Cardiovasc Ultrasound*, vol. 13, pp. 48–48, Dec. 2015, doi: 10.1186/s12947-015-0042-3.

[71] Z. Nuffer, A. Rupasov, N. Bekal, J. Murtha, and S. Bhatt, “Spectral Doppler ultrasound of peripheral arteries: a pictorial review,” *Clinical Imaging*, vol. 46, pp. 91–97, Nov. 2017, doi: 10.1016/j.clinimag.2017.07.007.

[72] J. A. Jensen *et al.*, “History and Latest Advances in Flow Estimation Technology: From 1-D in 2-D to 3-D in 4-D,” presented at the 2019 IEEE International Ultrasonics Symposium (IUS), Oct. 2019. doi: 10.1109/ultsym.2019.8926210.

[73] H. Bouzari *et al.*, “Curvilinear 3-D Imaging Using Row-Column-Addressed 2-D Arrays With a Diverging Lens: Feasibility Study,” *IEEE Transactions on Ultrasonics, Ferroelectrics, and Frequency Control*, vol. 64, no. 6, pp. 978–988, Jun. 2017, doi: 10.1109/tuffc.2017.2687521.

[74] J. Zhou *et al.*, “High-Volume-Rate 3-D Ultrasound Imaging Based on Synthetic Aperture Sequential Beamforming With Chirp-Coded Excitation,” *IEEE Transactions on Ultrasonics, Ferroelectrics, and*

*Frequency Control*, vol. 65, no. 8, pp. 1346–1358, Aug. 2018, doi: 10.1109/tuffc.2018.2839085.

[75] S. Fiorentini, L. M. Saxhaug, T. G. Bjastad, E. Holte, H. Torp, and J. Avdal, “Maximum Velocity Estimation in Coronary Arteries Using 3-D Tracking Doppler,” *IEEE Transactions on Ultrasonics, Ferroelectrics, and Frequency Control*, vol. 65, no. 7, pp. 1102–1110, Jul. 2018, doi: 10.1109/tuffc.2018.2827241.

[76] J. Udesen, F. Gran, K. L. Hansen, J. A. Jensen, C. Thomsen, and M. B. Nielsen, “High frame-rate blood vector velocity imaging using plane waves: simulations and preliminary experiments,” *IEEE Trans Ultrason Ferroelectr Freq Control*, vol. 55, no. 8, pp. 1729–1743, Aug. 2008, doi: 10.1109/TUFFC.2008.858.

[77] J. A. Jensen, S. Nikolov, A. C. H. Yu, and D. Garcia, “Ultrasound Vector Flow Imaging: I: Sequential Systems,” *IEEE Transactions on Ultrasonics, Ferroelectrics, and Frequency Control*, pp. 1–1, 2016, doi: 10.1109/tuffc.2016.2600763.

[78] J. Avdal, L. Lovstakken, H. Torp, and I. K. Ekroll, “Combined 2-D Vector Velocity Imaging and Tracking Doppler for Improved Vascular Blood Velocity Quantification,” *IEEE Transactions on Ultrasonics, Ferroelectrics, and Frequency Control*, vol. 64, no. 12, pp. 1795–1804, Dec. 2017, doi: 10.1109/tuffc.2017.2757600.

[79] P. Tortoli, M. Lenge, D. Righi, G. Ciuti, H. Liebgott, and S. Ricci, “Comparison of carotid artery blood velocity measurements by vector and standard Doppler approaches,” *Ultrasound Med Biol*, vol. 41, no. 5, pp. 1354–1362, May 2015, doi: 10.1016/j.ultrasmedbio.2015.01.008.

[80] M. Correia, J. Provost, M. Tanter, and M. Pernot, “4D ultrafast ultrasound flow imaging:in vivoquantification of arterial volumetric flow rate in a single heartbeat,” *Physics in Medicine and Biology*, vol. 61, no. 23, pp. L48–L61, Nov. 2016, doi: 10.1088/0031-9155/61/23/l48.

[81] S. Holbek, T. L. Christiansen, M. B. Stuart, C. Beers, E. V. Thomsen, and J. A. Jensen, “3-D Vector Flow Estimation With Row–Column-Addressed Arrays,” *IEEE Transactions on Ultrasonics, Ferroelectrics, and Frequency Control*, vol. 63, no. 11, pp. 1799–1814, Nov. 2016, doi: 10.1109/tuffc.2016.2582536.

[82] S. Holbek *et al.*, “Ultrasonic 3-D Vector Flow Method for Quantitative In Vivo Peak Velocity and Flow Rate Estimation,” *IEEE Transactions on Ultrasonics, Ferroelectrics, and Frequency Control*, vol. 64, no. 3, pp. 544–554, Mar. 2017, doi: 10.1109/tuffc.2016.2639318.

[83] M. S. Wigen *et al.*, “4-D Intracardiac Ultrasound Vector Flow Imaging–Feasibility and Comparison to Phase-Contrast MRI,” *IEEE Transactions on Medical Imaging*, vol. 37, no. 12, pp. 2619–2629, Dec. 2018, doi: 10.1109/tmi.2018.2844552.

[84] S. Rossi, A. Ramalli, F. Fool, and P. Tortoli, “High-Frame-Rate 3-D Vector Flow Imaging in the Frequency Domain,” *Applied Sciences*, vol. 10, no. 15, p. 5365, Aug. 2020, doi: 10.3390/app10155365.

[85] R. Y. Chiao and Xiaohui Hao, “Coded excitation for diagnostic ultrasound: a system developer’s perspective,” *IEEE Transactions on Ultrasonics,*

*Ferroelectrics and Frequency Control*, vol. 52, no. 2, pp. 160–170, Feb. 2005, doi: 10.1109/TUFFC.2005.1406543.

[86] A. Ramalli, F. Guidi, E. Boni, and P. Tortoli, "A real-time chirp-coded imaging system with tissue attenuation compensation," *Ultrasonics*, vol. 60, pp. 65–75, Jul. 2015, doi: 10.1016/j.ultras.2015.02.013.

[87] A. Ramalli, E. Boni, A. Dallai, F. Guidi, S. Ricci, and P. Tortoli, "Coded Spectral Doppler Imaging: From Simulation to Real-Time Processing," *IEEE Transactions on Ultrasonics, Ferroelectrics, and Frequency Control*, vol. 63, no. 11, pp. 1815–1824, Nov. 2016, doi: 10.1109/TUFFC.2016.2573720.

[88] C. Yoon, W. Lee, J. Chang, T. Song, and Y. Yoo, "An efficient pulse compression method of chirp-coded excitation in medical ultrasound imaging," *IEEE Transactions on Ultrasonics, Ferroelectrics and Frequency Control*, vol. 60, no. 10, pp. 2225–2229, 2013, doi: 10.1109/TUFFC.2013.2815.

[89] T. Misaridis and J. A. Jensen, "Use of modulated excitation signals in medical ultrasound. Part I: basic concepts and expected benefits," *IEEE Transactions on Ultrasonics, Ferroelectrics and Frequency Control*, vol. 52, no. 2, pp. 177–191, Feb. 2005, doi: 10.1109/TUFFC.2005.1406545.

[90] T. Misaridis and J. A. Jensen, "Use of modulated excitation signals in medical ultrasound. Part II: design and performance for medical imaging applications," *IEEE Transactions on Ultrasonics, Ferroelectrics and Frequency Control*, vol. 52, no. 2, pp. 192–207, Feb. 2005, doi: 10.1109/TUFFC.2005.1406546.

[91] P. Tortoli, G. Guidi, and P. Pignoli, "Transverse doppler spectral analysis for a correct interpretation of flow sonograms," *Ultrasound in Medicine & Biology*, vol. 19, no. 2, pp. 115–121, Jan. 1993, doi: 10.1016/0301-5629(93)90003-7.

[92] P. Tortoli, V. Michelassi, G. Bambi, F. Guidi, and D. Righi, "Interaction between secondary velocities, flow pulsation and vessel morphology in the common carotid artery," *Ultrasound Med Biol*, vol. 29, no. 3, pp. 407–415, Mar. 2003.

[93] V. L. Newhouse, K. S. Dickerson, D. Cathignol, and J.-Y. Chapelon, "Three-dimensional vector flow estimation using two transducers and spectral width," *IEEE Transactions on Ultrasonics, Ferroelectrics, and Frequency Control*, vol. 41, no. 1, pp. 90–95, Jan. 1994, doi: 10.1109/58.265826.

[94] E. Boni, F. Fool, M. D. Verweij, H. J. Vos, and P. Tortoli, "On the efficacy of in-probe pre-amplifiers for piezoelectric 2D arrays," presented at the 2020 IEEE International Ultrasonics Symposium (IUS), 2020.

[95] A. Østvik, E. Smistad, S. A. Aase, B. O. Haugen, and L. Lovstakken, "Real-Time Standard View Classification in Transthoracic Echocardiography Using Convolutional Neural Networks," *Ultrasound in Medicine & Biology*, vol. 45, no. 2, pp. 374–384, Feb. 2019, doi: 10.1016/j.ultrasmedbio.2018.07.024.

[96] Y. Gao, Y. Zhu, B. Liu, Y. Hu, G. Yu, and Y. Guo, "Automated Recognition of Ultrasound Cardiac Views Based on Deep Learning with Graph

Constraint," *Diagnostics*, vol. 11, no. 7, Art. no. 7, Jul. 2021, doi: 10.3390/diagnostics11071177.

[97] A. Madani, R. Arnaout, M. Mofrad, and R. Arnaout, "Fast and accurate view classification of echocardiograms using deep learning," *npj Digital Med*, vol. 1, no. 1, pp. 1–8, Mar. 2018, doi: 10.1038/s41746-017-0013-1.

[98] E. Roux, A. Ramalli, H. Liebgott, C. Cachard, M. C. Robini, and P. Tortoli, "Wideband 2-D Array Design Optimization With Fabrication Constraints for 3-D US Imaging," *IEEE Transactions on Ultrasonics, Ferroelectrics, and Frequency Control*, vol. 64, no. 1, Art. no. 1, Jan. 2017, doi: 10.1109/TUFFC.2016.2614776.

[99] F. Prieur, B. Dénarié, A. Austeng, and H. Torp, "Correspondence - Multi-line transmission in medical imaging using the second-harmonic signal," *IEEE Transactions on Ultrasonics, Ferroelectrics, and Frequency Control*, vol. 60, no. 12, pp. 2682–2692, Dec. 2013, doi: 10.1109/TUFFC.2013.2868.

[100] G. Matrone, A. Ramalli, A. S. Savoia, P. Tortoli, and G. Magenes, "High Frame-Rate, High Resolution Ultrasound Imaging With Multi-Line Transmission and Filtered-Delay Multiply And Sum Beamforming," *IEEE Transactions on Medical Imaging*, vol. 36, no. 2, pp. 478–486, Feb. 2017, doi: 10.1109/TMI.2016.2615069.

[101] G. Matrone, A. S. Savoia, G. Caliano, and G. Magenes, "The Delay Multiply and Sum Beamforming Algorithm in Ultrasound B-Mode Medical Imaging," *IEEE Transactions on Medical Imaging*, vol. 34, no. 4, pp. 940–949, Apr. 2015, doi: 10.1109/TMI.2014.2371235.

[102] A. C. Dhanantwari *et al.*, "An efficient 3D beamformer implementation for real-time 4D ultrasound systems deploying planar array probes," in *2004 IEEE Ultrasonics Symposium*, Aug. 2004, vol. 2, pp. 1421-1424 Vol.2. doi: 10.1109/ULTSYM.2004.1418067.

[103] B. J. Savord, "Beamforming methods and apparatus for three-dimensional ultrasound imaging using two-dimensional transducer array," Nov. 01, 2000 Accessed: Dec. 06, 2011. [Online]. Available: http://www.freepatentsonline.com/6013032.html

[104] A. Ibrahim *et al.*, "Efficient Sample Delay Calculation for 2-D and 3-D Ultrasound Imaging," *IEEE Transactions on Biomedical Circuits and Systems*, vol. 11, no. 4, pp. 815–831, Aug. 2017, doi: 10.1109/TBCAS.2017.2673547.

[105] A. Fenster, D. B. Downey, and H. N. Cardinal, "Three-dimensional ultrasound imaging," *Phys. Med. Biol.*, vol. 46, no. 5, p. R67, May 2001, doi: 10.1088/0031-9155/46/5/201.

[106] N. Q. Nguyen and R. W. Prager, "A Spatial Coherence Approach to Minimum Variance Beamforming for Plane-Wave Compounding," *IEEE Transactions on Ultrasonics, Ferroelectrics, and Frequency Control*, vol. 65, no. 4, pp. 522–534, Apr. 2018, doi: 10.1109/TUFFC.2018.2793580.

[107] G. Matrone, A. Ramalli, J. D'hooge, P. Tortoli, and G. Magenes, "A Comparison of Coherence-Based Beamforming Techniques in High-Frame-Rate Ultrasound Imaging With Multi-Line Transmission," *IEEE Transactions on Ultrasonics, Ferroelectrics, and Frequency Control*, vol. 67, no. 2, pp. 329–340, Feb. 2020, doi: 10.1109/TUFFC.2019.2945365.

[108] A. Wiacek, E. González, and M. A. L. Bell, "CohereNet: A Deep Learning Architecture for Ultrasound Spatial Correlation Estimation and Coherence-Based Beamforming," *IEEE Transactions on Ultrasonics, Ferroelectrics, and Frequency Control*, vol. 67, no. 12, pp. 2574–2583, Dec. 2020, doi: 10.1109/TUFFC.2020.2982848.

[109] K. Gedalyahu, R. Tur, and Y. C. Eldar, "Multichannel Sampling of Pulse Streams at the Rate of Innovation," *IEEE Transactions on Signal Processing*, vol. 59, no. 4, pp. 1491–1504, Apr. 2011, doi: 10.1109/TSP.2011.2105481.

[110] A. Burshtein, M. Birk, T. Chernyakova, A. Eilam, A. Kempinski, and Y. C. Eldar, "Sub-Nyquist Sampling and Fourier Domain Beamforming in Volumetric Ultrasound Imaging," *IEEE Transactions on Ultrasonics, Ferroelectrics, and Frequency Control*, vol. 63, no. 5, pp. 703–716, May 2016, doi: 10.1109/TUFFC.2016.2535280.

[111] I. A. M. Huijben, B. S. Veeling, K. Janse, M. Mischi, and R. J. G. van Sloun, "Learning Sub-Sampling and Signal Recovery With Applications in Ultrasound Imaging," *IEEE Transactions on Medical Imaging*, vol. 39, no. 12, pp. 3955–3966, Dec. 2020, doi: 10.1109/TMI.2020.3008501.

[112] B. Luijten *et al.*, "Adaptive Ultrasound Beamforming Using Deep Learning," *IEEE Transactions on Medical Imaging*, vol. 39, no. 12, pp. 3967–3978, Dec. 2020, doi: 10.1109/TMI.2020.3008537.

[113] N. Wagner, Y. C. Eldar, and Z. Friedman, "Compressed Beamforming in Ultrasound Imaging," *IEEE Transactions on Signal Processing*, vol. 60, no. 9, pp. 4643–4657, Sep. 2012, doi: 10.1109/TSP.2012.2200891.